SALT AND TESS MONITORING OF CENTRAL STARS OF PLANETARY NEBULAE

Kelebogile Bonokwane
Supervisor: Dr. B. Miszalski [1]
Co-supervisor: Dr S. Mohamed [2,3]
Co-supervisor: Dr I. Monageng [2,3]
Co-supervisor: Dr R. Manick [3]

31 August 2020

A thesis presented to the University of Cape Town in full fulfilment of the degree:
Master of Science in Astrophysics and Space science
UNIVERSITY OF CAPE TOWN

[1] Macquarie University
[2] University of Cape Town
[3] South African Astronomical Observatory

Abstract

Planetary Nebulae (PNe) are the product of Asymptotic Giant Branch (AGB) evolution. Evolved from Solar-like intermediate mass stars (0.8 – 8$M_{\odot}$), they have a hot, radiating core that ionizes the gas of the expelled envelope, producing a glowing nebula. The core eventually evolves into a white dwarf (WD), following the WD cooling track. Complex, aspherical morphologies are observed in PNe and binary central stars (CSs) have been the favoured explanation for deviations from spherical symmetry. Finding and characterizing the population of binary CSs is thus important to understand the physics behind their morphologies. The objects of this study are Hen3-1333, Hen2-113 and Hen2-47, all with Wolf-Rayet (WR) CSs that commonly exhibit fast, dense stellar winds. All exhibit multipolarity in their young nebulae, Hen3-1333 has a disk and dual-dust chemistry, while the other two have central stars offset from the geometric centre of their nebulae. The objects were chosen because most of these features, especially multipolar morphologies, are not well represented amongst PNe with known binary CSs. Here we develop a quantitative time-series analysis to determine whether these objects have binary CSs and develop constraints to permissible orbital parameters.

The High Resolution Spectrograph (HRS) of the Southern African Large Telescope (SALT) was used to collect échelle spectroscopic data over 3 years and The Exoplanet Survey Satellite (TESS) was used to obtain photometric data for the objects. The medium resolution (MR) mode (R $\approx$ 40000) was chosen and 58, 60, and 35 spectra were collected for Hen3-1333, Hen2-113 and Hen2-47, respectively, with an average S/N of 40 at 4495 Å. The TESS data had continuous sampling (30 min cadence) recorded for an orbit length of 27.4 days. Using cross-correlation and Gaussian line fitting, radial velocity (RV) time-series were compared to lightcurves determined from the TESS data. Lomb-Scargle periodograms were used to search for periodic variability in the RV and photometry time-series data. The results were discussed based on short (0 – 10 days), intermediate (10 – 10^3 days) and long (10^3 – 10^4 days) orbital period ranges. Compatible scenarios for each range were estimated by combining observational constraints with different parameters expected for assumed companion star types. The quantitative variability analysis excludes short orbital period binary systems, suggesting that if their multiple features are due to binary interactions, the most likely case is the long orbital period range. If the variability observed is due to a companion, rather

than pulsations from the CS, the companion masses, 0.10 – 1.36 $M_{\odot}$ for Hen3-1333, 0.043 – 1.27 $M_{\odot}$ for Hen2-113 and 0.077 – 1.36 $M_{\odot}$ for Hen2-47, correspond to main sequence stars and dwarfs.

Acknowledgements

I would like to express my most humble gratitude to my supervisory team for all the constructive advice in fulfilment of this dissertation. You saw potential in me and have helped equip me with valuable skills for my research career. I wish to express my gratitude to the University of Cape Town and the South African Astronomical Observatory for the resources and facilities that provided a conducive working environment. I would like to acknowledge the facilities that provided the data that was used in this work. Some of the observations reported in this dissertation were obtained with the Southern African Large Telescope (SALT) under the proposal codes 2016-2-SCI-034, 2017-1-MLT-010 and 2018-2-MLT-007 (PI B. Miszalski). This dissertation also includes data collected by the TESS mission. Funding for the TESS mission is provided by the NASA Explorer Program. I would like to convey many thanks to the National Research Foundation and the National Astrophysics and Space Science Programme for funding my degree.

I would like to say a special thank you to my partner and family for the immeasurable support, encouragement and love they have shown me. Most importantly I would like to thank my Creator for the grace He has blessed me with throughout my journey to fulfill my purpose.

Plagiarism Declaration

I, Kelebogile Verginia Stephanie Bonokwane, know the meaning of plagiarism and declare that all of the work in the document, save for that which is properly acknowledged, is my own.

Contents

List of Figures

List of Tables

Chapter 1

Introduction

1.1 Planetary nebulae

Planetary nebulae (PNe) are the evolved remnants low-to-intermediate mass stars similar to our Sun ($0.8M_{\odot}$ to $8M_{\odot}$). They start off as a main sequence star with H burning in the core, producing a He core (Fig. 1.1, Herwig 2005). These stars evolve to the red giant phase when H burning starts in a shell around the He core (Herwig 2005). The He core burning out produces a C/O core surrounded by a He and H shell as the star evolves to the Asymptotic Giant Branch (AGB) phase (Herwig 2005). The PN follows just off the AGB, heats up and then cools down into a white dwarf past the knee of the cooling track (Fig. 1.1) (De Marco 2009). The core ejects material in its surrounding shell, once ejected and carried by strong winds, is left surrounding the exposed core. The core is a white dwarf and radiation from the core ionizes the expelled gas. The ionized material surrounding the core is known as the nebula. The PN evolutionary phase is short, the nebula lasts about 10 000 years and the size of it shrinks by a factor of 3 from what it is at the start of the PN phase (Kwok 2005). At this stage the temperature of the nebula increases by a factor of about 20, starting from 5000 K to temperatures as high as 100 000 K (Hajduk et al. 2015). The rapid evolution of central stars (CSs) of PNe makes it easy to trace the evolution of individual PNe CSs (Hajduk et al. 2015).

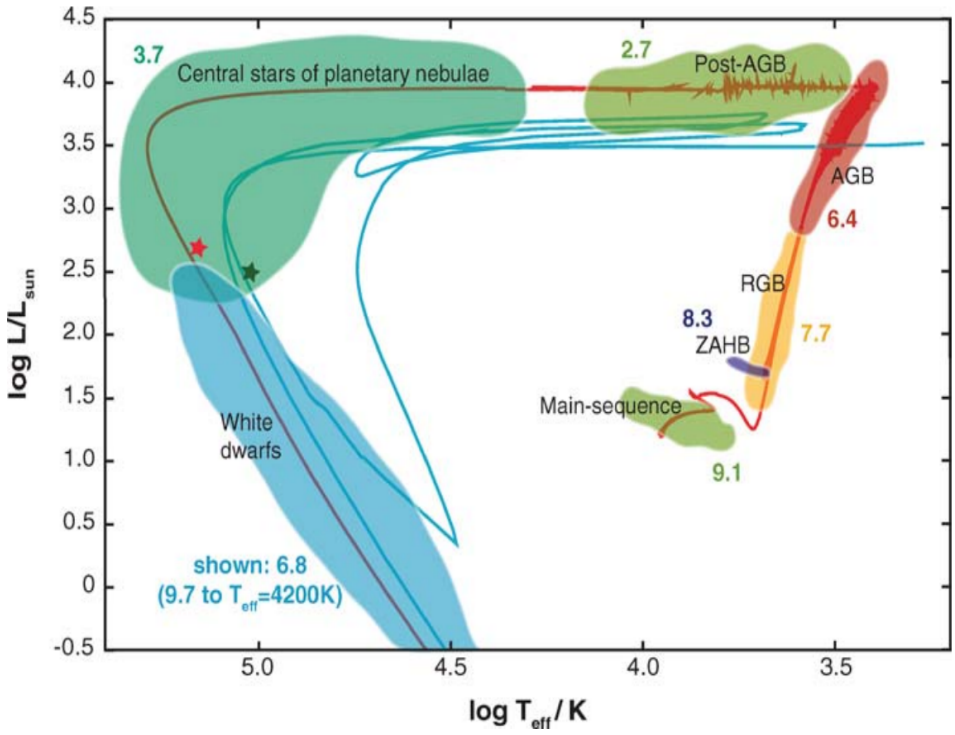

Figure 1.1: *The evolutionary track (red line) of a $2M_{\odot}$ star in the Hertzsprung-Russell Diagram (Herwig 2005).*

PNe are observed in early and late type galaxies. Furthermore, PNe can be used to trace the elements in the chemistry and the abundance of those elements in the galaxies. The emission lines are bright so they can be seen in distant galaxies and the chemical abundances of PNe can tell more about the stellar population of the galaxy. PNe are therefore similar to H II regions but PNe can trace a wider range of progenitor ages whereas H II regions are limited to young, massive stars (Gonçalves 2019). The information from the emission lines helps constrain chemical evolution models (Gonçalves 2019). PNe can be divided into two categories based on chemical abundances, these are He/H and N/O (Kingsburgh and Barlow 1994). Type I PNe are young (<1 Gyr old progenitors with masses $>3M_{\odot}$), while non-Type I have ages <10 Gyr and are old enough to trace the interstellar medium (ISM) chemical evolution (Gonçalves 2019). The ages of PNe populations are studied and used to probe metallicity gradients of the Galaxy (Stanghellini and Haywood 2010). Stanghellini and Haywood (2010) further discussed that gradients of oxygen and iron abundance from young stars (<1.0 Gyr) and intermediate-age (open clusters, <5 Gyr) populations agree with those of PNe derived in their work.

Planetary nebulae can be used to construct rotation curves of galaxies. The rotation curves of spiral galaxies can be decomposed into a disk donor and dark halo contributor, therefore providing a direct technique for studying the structure of dark halos (Aniyan et al. 2017). The decomposition depends on M/L (mass/luminosity) values and these are critical for obtaining the parameters of dark halos, a key ingredient in the field of cosmology. Jacoby (1980) developed the luminosity function (LMF) for PNe in the Local Group to estimate the PNe population there-in and project populations in other galaxies. Furthermore the LMF of PNe can be used as a distance indicator (Ciardullo 2010). It was found that for galaxies of known distances, the absolute magnitudes of the brightest PNe were always similar (Ciardullo 2010, Méndez 2017). This realization led to PNe being used as standard candles but Méndez (2017) concluded that surface brightness fluctuations and tip of the red giant branch distance methods have an advantage since they can be used in the infrared.

The important applications of PNe commonly assume spherical structures, since these are observed and provide a simplified interpretation. PNe have however been observed to come in interesting shapes and sizes. Jets, multiple lobes, disks, and rings are among the common features observed in aspherical PNe as discussed in the following section.

1.2 Morphology of planetary nebulae

The structure of PNe has been commonly observed to show different morphologies that have been modelled over the years to understand the origin of these structures (Raga et al. 2009, Velázquez et al. 2011, Zou et al. 2019). Balick and Frank (2002) describe the basic categories of nebula types as Round (R, prototype IC 3568), Elliptical (E, NGC 3132 and 6826), Bipolar (Bp, a pair of lobes), and irregular (relatively rare). A more detailed attempt to classify PNe according to their morphology was done by Sahai et al. (2011), noting that the projection in which an object is observed can play a role in how we perceive the morphology Jones et al. (2012). Sahai et al. (2011) expanded on the basic structures by accounting for secondary features (open/closed lobes, waists, point-symmetry, halo).

The simplest morphological type is a spherical PN and Abell 39 (Fig. 1.2, top left panel) is a classic example. The more complex shaped PNe have rings and spiral structures, NGC 6543 (Fig. 1.2, top right panel) is an example of them. MyCn 18 (Fig. 1.2, left middle panel) is a bipolar PN with symmetric hourglass lobes and a pinched waist. Similarly another popular bipolar PN is M2-9 (Fig. 1.2, right middle panel). Jets are commonly observed and these can be modelled as ballistic outflows where precession of the outflow axis produces a point-symmetric spiral jet/counterjet system (Raga et al. 2009). A binary nucleus was discovered in Fg1 (Fig. 1.2, bottom panel; Boffin et al. 2012), the archetype of this morphological class, validating the result from Raga et al. (2009). Zou et al. (2019) states that most non-spherical PNe are young and these tend to show more complex morphologies than the pre-planetary nebulae (PPNe) they evolve from, especially the ones with mulitipolar morphologies (Sahai

and Trauger 1996, 1998). The waist structure is an example, in the case of PPNe it can be less exposed and visible than in young PNe (Sahai et al. 2011). The next section further discusses the morphology of young PNe.

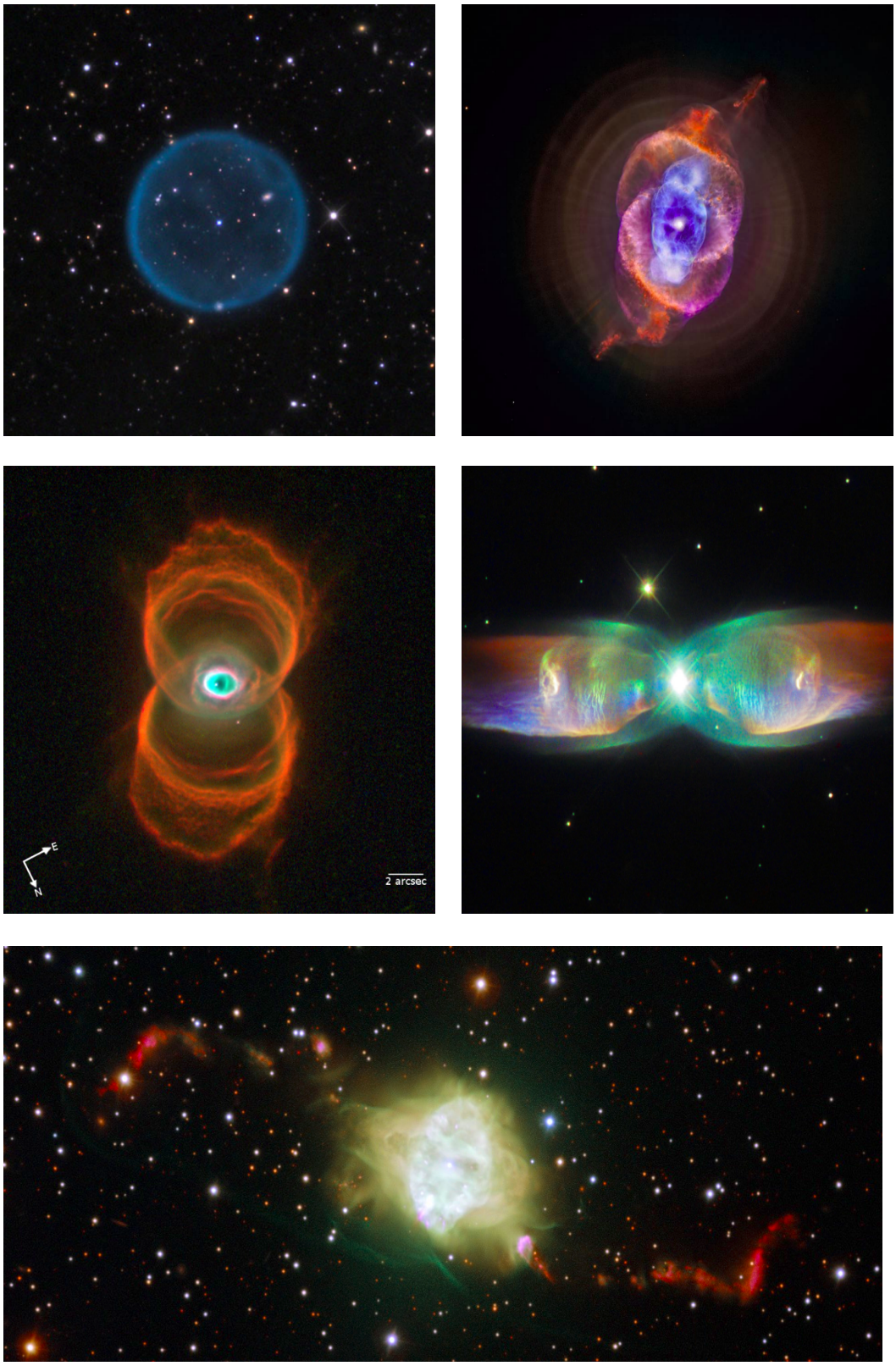

Figure 1.2: *Images of PNe displaying multipolarity, jets and offset CSs. Abell 39 (WIYN/NOAO/NSF) (top left panel), NGC 6543 (NASA teams (CXC/SAO/STScI)) (top right panel), MyCn 18 (Sahai et al. 1999) (left middle panel), M2-9 (NASA, ESA, HST) (right middle panel), Fg1 (Boffin et al. 2012) (bottom panel).*

1.2.1 Young multipolar PNe

Planetary nebulae have a short evolution phase but they can be divided into young-and older-type PNe. PPNe are observed around 1000 years after the AGB phase, as a transition phase to the young PNe phase (Kwok and Hrivnak 1993). Most of these PPNe have complex, aspherical morphologies with toroidal envelopes and collimated outflows (Sahai et al. 2007). As these features develop over the first few hundred years, PPNe are important probes to understand how spherical AGB winds transform to aspherical PNe (Balick and Frank 2002). In recent years, observations of objects such as the Red Rectangle and IRAS 08544-4431 suggest they may be shaped by a disk wind launched from a rotating disk (Bujarrabal et al. 2018). Objects with this kind of aspherical structure with multiple lobes are called multipolar PPNe. Multipolar PPNe may be shaped through ballistic outflows or bullets (Balick et al. 2013) or possibly precessing collimated fast winds and jets with time-dependent ejection velocity (Velázquez et al. 2014). The bullets are produced in explosive events and these lead to the multipolar outflows observed in young PNe when the CS is hot enough to ionize the nebula. Sect. 1.4.4 further discusses multipolarity in PNe. The mechanisms responsible for the morphologies of PNe have been much debated and the following section explores the proposed scenarios.

1.3 The shaping of complex PNe

The stellar astrophysics community has debated whether the morphology and shaping of PNe is due to stellar rotation, the presence of magnetic fields or binary nuclei (Balick and Frank 2002, De Marco 2009). The interacting stellar winds model is one of the oldest models to support the shaping of PNe (Kwok et al. 1978), however it cannot explain all observed morphologies. More recently, the binary CS scenario has become the favoured explanation especially for the most complex PNe.

1.3.1 The interacting stellar wind (ISW) model

The interacting stellar wind model (ISW) was introduced by Kwok et al. (1978) to explain the formation of PN shells. The framework involves a fast stellar wind rapidly sweeping up slower, denser material lost on the AGB. In this case a majority of the kinetic energy in the fast wind is converted to thermal energy at a radiation-less shock (Balick and Frank 2002). In a steady state, the ram pressure of the heated shock wind matches the pressure of the denser upstream material. This interaction stops the fast wind from reaching the slower wind directly in a steady state (Balick and Frank 2002), see schematic of model in Fig. 1.3.

Frank et al. (1990) showed that predictions of ISW models agree well with the density distribution. Calvet and Peimbert (1983) suggested dense circumstellar tori can move away the winds in the direction of a polar axis, thus forming bubbles resulting in a bipolar outflow. Thus further studies of the ISW model continued with analytic and numerical studies of fast

winds interacting with disks and tori (Frank 1994, Icke 1988, Soker and Livio 1989). These studies led to the development of the generalized interacting stellar winds models (GISW). Morris (1981, 1987) and Soker and Livio (1989) agreed that the disks might be remnants of binary mergers and tidal interactions, but the disks origin is assumed and the model therefore fails to produce bipolar PNe. The GISW could account for spherical, elliptical and bipolar morphologies, but as observations improved, PNe jets could not be explained by the model (Balick and Frank 2002).

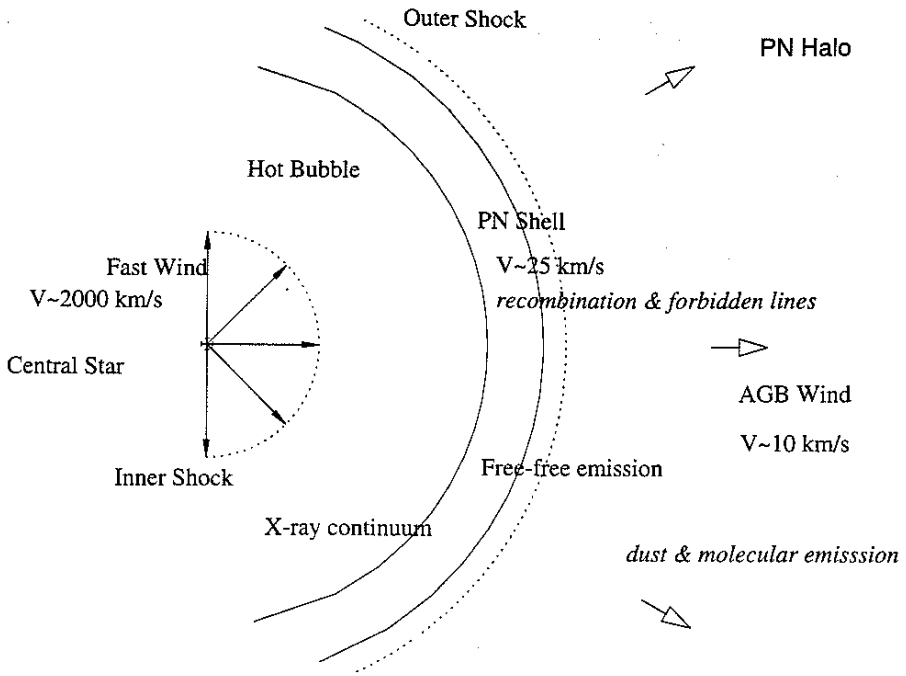

Figure 1.3: *A schematic adapted to illustrate the region around the CS and the process described in the ISW model (Kwok 2000).*

1.3.2 Magnetic fields in PNe

Magnetic fields were proposed as the mechanism responsible for forming the axisymmetric shapes in PNe (Garcia-Segura et al. 1997, García-Segura et al. 2014, 2020). Discovering a sufficiently strong magnetic field in the CSs of PNe would present strong support for the hypothesis that the axisymmetric or bipolar PNe resulted from magnetic collimation (Blackman 2009). Theoretical arguments however demonstrated that the structure of aspherical PNe are likely not be due to large scale magnetic fields (Soker 2006). Steffen et al. (2014) finds that for the majority of the observed CSs, there is no significant evidence that such surface magnetic fields exist. The measurements from Steffen et al. (2014) indicate that there is a weak mean longitudinal magnetic field of 100 Gauss in three CSs of young PNe.

Magnetic fields in PNe are believed to be present during the common envelope (CE) phase (García-Segura et al. 2020). In the event of a CE, an unbound section of the giant star's envelope is launched and ejected. The bound material falls back and creates an accretion disk, a merger may occur or a circumbinary accretion disk may develop. If the stellar companion remains the spiral-in phase, a short period binary system results (Ivanova et al. 2013). Soker and Livio (1994) suggested in both cases of the disks, magnetically driven winds and jets can be produced and Tocknell et al. (2014) discusses magnetic field constraints due to systems with jets. Presuming that some of the circumbinary accretion disk lands on the stars and the primary star remnant is hot, García-Segura et al. (2020) studied the scenario which accounts for all winds. Lee and Sahai (2003) have assumed and modelled this outflowing wind as a "tapered" flow, Balick et al. (2019) recently modelled this wind.

The role of magnetic fields in shaping PNe has been questioned with regards to how strong stellar surface magnetic fields are and how long such fields last (Soker 2006). The fields inside the stars come from the core-envelope boundary that results in sizable shear (García-Segura et al. 2014). In the case that the core ejects the envelope during the spiral-in phase, magnetic fields can be processed outwards and can fall back onto the circumbinary disk.

The magnetic field scenario according to the above observations and models may play a contributing role in shaping the morphology of PNe, but a binary system is still required to explain the complex morphology (García-Segura et al. 2020). However, the idea of magnetic fields being a contributing factor still improves upon the results of the ISW model for higher-order structure (e.g. multipolar) PNe. In the following section the binary CS scenario is explored in detail with observational evidence.

1.3.3 Surveys for binary CSs

The binary CS scenario considers a stellar companion to the CS. Here the interaction of the two stars, particularly the CE interaction, is believed to be the reason for the shaping of the nebula. This scenario has grown in popularity over the years because it had increasing observational support compared to the competing scenarios (Bond 2000, Miszalski et al. 2009). To grow the population of discovered binary CSPNe in morphologically complex PNe, several surveys were conducted. Photometry studies dominate these surveys historically, but due to observational biases and limitations (eg. bias towards short orbital periods, nebular contamination; De Marco et al. 2008) the surveys have since evolved. This spurred a shift towards radial velocity (RV) monitoring surveys since they were less affected by these biases. These studies improved upon the photometric surveys by discovering a wider range of orbital periods. High resolution échelle RV surveys proved much more successful than low-resolution RV surveys and continue to increase the numerical fraction of binary CSPNe.

Photometric monitoring

Photometry was the most effective tool that has been widely used to monitor CSs of PNe (CSPNe) due to its efficiency and simplicity; it proved very useful for finding binary systems in PNe (Miszalski et al. 2009). Several surveys were conducted: Bond (2000) identified 16 PNe with close binary systems, stating these binaries comprise of $\approx$ 10% of CSs and the Optical Gravitational Lensing Experiment (OGLE) III photometric survey helped identify a binary fraction of 10 - 20 % (Miszalski et al. 2009), in agreement with the result by Bond (2000). Photometry works well for discovering binaries amongst faint PNe. In recent surveys the faintness achieved with the Exoearth Discovery and Exploration Network (EDEN) is said to be 3 mags fainter than the Transiting Exoplanet Survey Satellite (TESS) (I $\approx$ 15 mag) (Gibbs et al. 2020).

The disadvantages of photometry are that it is limited to shorter orbital periods ($<$ 3 days; De Marco et al. 2008). This selection effect in photometric surveys makes binaries with longer orbital periods difficult to detect. Photometric detection of binarity depends on the heating of one hemisphere of the companion by the primary, ellipsoidal variations and/or eclipsing systems (De Marco et al. 2008). This technique does not work well for binary systems with long periods since heating of the companion and ellipsoidal variations are more prominent in binaries with short separations (De Marco et al. 2008).

In order to minimize the detection bias towards lower orbital period binaries among PNe, the radial velocity (RV) method is needed (Bond 2000). RV monitoring is the application of Doppler spectroscopy and Bond (2000) suggested that RV surveys are needed to probe the expected large population of binary systems between 10 - 100 days (see also, Bond (2005)). In an attempt to address how biases can be eliminated Nebot Gómez-Morán et al. (2011) identified a mean detection probability greater than 35% for their RV survey based on a

population of white dwarf-main sequence (WDMS) binaries and post-CE binaries (PCEB), and used it to correct for biases in orbital period. The WDMS and PCEB are closely related to CSPNe since the latter are post-CE and eventually evolve into WDs. The bias-corrected distribution (Fig. 10) in Nebot Gómez-Morán et al. (2011) population synthesis still agreed with previous models, showing a decline of objects towards longer periods. Toonen and Nelemans (2013) claim that these selection effects therefore hardly play a role on the period distribution of visible PCEBs. These results imply PNe binaries (which are PCEBs) may simply have more shorter orbital periods but it is important to continue the search for longer orbital periods before coming to a final conclusion.

Radial velocity monitoring

After Bond (2000) successfully identified variability in PNe, several RV surveys were conducted (e.g. Afsar and Bond 2005, De Marco et al. 2004, Sorensen and Pollacco 2003). Sorensen and Pollacco (2003) used the 4.2m William Herschel and 2.5m Isaac Newton (INT) telescopes of the Isaac Newton Group on the Island of La Palma (Canary Islands). The Intermediate Dispersion Spectrograph (IDS) with a resolution of 1.5 Å onboard the INT was used. There were 6 – 40 high quality spectra taken and the removal of two wind variables results in 18% variability that may imply binarity at intermediate periods. The short and long period orbits suggested a 40% binary fraction and correcting for unobserved companions this value reached up to 60%. De Marco et al. (2004) made use of the 3.5 m WIYN[1] telescope from 2002 to 2003 and the Hydra fiber optics bench mounted spectrograph which has a resolution 0.60 Å. The results presented exceed a binary fraction of 50% for intermediate period objects based on the variability observed. Afsar and Bond (2005) presented a survey from the Small and Moderate Aperture Research Telescope System (SMARTS) operated at Cerro Tololo Interamerican observatory (CTIO). Longslit spectroscopic data were obtained for 19 southern planetary nuclei (PNNi). The FWHM achieved was 2.2 Å and about half of the sample appeared to have variable RVs with more than 90% confidence, where 37% of them were 99% confidences. A more recent RV survey was conducted by Manick et al. (2015) where six PNe were monitored at the South African Astronomical Observatory (SAAO). The SAAO 1.9m Telescope was equipped with the SpCCD spectrograph having a resolution of 1.09 - 2.4 Å FWHM and the SALT observations were done using the RSS which has a resolution 2.4 Å and the cross-correlation had a velocity accuracy of 10 km/s.

The surveys mentioned above were a great improvement to CSPNe monitoring for variability, however they did not determine the orbital periods to validate the variability and prove binarity for their objects. The results included sample sizes that were small and the number of individual observations per object were also small. The exact procedure and individual measurements for some results were not explicitly explained, making it difficult to interpret the results. The observations of the objects in the surveys were conducted with

[1]Wisconsin-Indiana-Yale-NOAO telescope (WIYN) operated at Kitt Peak National observatory, Arizona; Roddier et al. (1995)

low resolution because of the availability at the time. With improved facilities now, new high resolution spectroscopy is conducted with échelle spectrographs.

Van Winckel et al. (2014) used the High-Efficiency and high-Resolution Mercator échelle Spectrograph (HERMES; Raskin et al. 2011) from the 1.2 m Mercator telescope at the La Palma del Roque de Los Muchachos observatory. A spectral resolution of $R = \lambda/\Delta\lambda = 85000$ covering a wavelength range 377 – 900 nm is produced. PN G052.7+50.7 was observed to have an orbital period of 1136 days and LoTr5 was observed to have an orbital period longer than 1800 days, a result that was not fully covered at that point but later determined in Jones et al. (2017) who also used HERMES to monitor PNe. This is an ongoing survey started in 2009 with the CSs of NGC 1514 (BD+30°623) and HD 112313 (LoTr 5), resulting in confirmed binaries with orbital periods of 3306 and 2717 days, respectively.

Miszalski et al. (2018a) made use of the SALT HRS spectrograph in medium resolution mode, achieving resolving power of R = 43000 and R = 40000 for the blue and red arms, respectively. The CS of NGC 1360 was found to be a double degenerate binary with an orbital period of 142 days and semi-amplitude of 11.8 km/s. MyCn 18 which exhibits an offset CS was found to have an orbital period of 18.15 days with a semi-amplitude of 11 km/s (Miszalski et al. 2018b). Later IC 4776 revealed an orbital period of 3.11 days (Miszalski et al. 2019a) and Sp3 was discovered to have an orbital period of 4.8 days and to very likely be a triple system (Miszalski et al. 2019b). The surveys conducted with échelle spectroscopy are currently the focus for RV monitoring.

1.4 Characteristics and features associated with binarity

Several common morphological features of PNe are not commonly found among PNe with discovered binary CS. These inlcude, Wolf-Rayet CSs, dual dust chemistry, disk/torus, multipolarity, offset CSs and we expand upon each feature in the this section.

1.4.1 Wolf-Rayet CSs

Wolf-Rayet (WR) stars are stars following the end of their evolution, experiencing extensive mass loss through dense stellar winds. One can tell a WR star through the strong emission lines of carbon (WC), oxygen (WO) or nitrogen (WN) (Crowther et al. 1998). WR stars are either massive (Pop I) or low mass (Pop II) CSPNe. Crowther et al. (1998) developed a classification scheme for WR stars focusing on WC and WO stars, concluding that they require abundance studies to confirm that the C and O abundances in the massive and CSPN WC-type stars from their work are consistent. [WC] CSs are a subclass of the carbon-rich WR stars in PNe, the CSs have carbon and helium rich atmospheres but are hydrogen deficient (Todt and Hamann 2015). WR systems are often found in dusty regions of the Galaxy (Perea-Calderón et al. 2009) and the notion of a dual dust presence is observed as carbon

and oxygen lines in the spectra of the nebula. It is claimed that about 50 % of known [WC] PNe are observed to have this dual-dust chemistry (Cohen et al. 2002, De Marco and Soker 2002), more detail is given in Sec. 1.4.3.

The birth place of the [WC] CSPNe is assumed to come from thermal pulses towards the final phase of the AGB or possibly towards the early phase of the post-AGB (Zijlstra et al. 1991). WR star formation is however still poorly understood but it is suggested that they are linked to binary systems (De Marco and Soker 2002) but the born-again scenario does not explain [WN] stars (Miszalski et al. 2012).

1.4.2 Offset CSs

Offset CS were thought to be due to large eccentric orbits and variable mass loss and interactions, which would impart a large shift of the orbit over time and the CS would thus shift (Soker et al. 1998). One of the authors' assumptions is that eccentric orbit binaries are largely responsible for displaced CSs of bipolar PNe therefore making a restricting case. To account for a more general case Chamandy et al. (2019) investigated the energy budget of the CE evolution. In their work, Chamandy et al. (2019) trace the centre of mass (CM) of a particle-gas structure and the CE. The top panel of Fig. 1.4 illustrates the trail of the particle CM in blue, the gas CM is in orange and the envelope CM in red, while the entire system CM is in green. The top panel of Fig. 1.4 also indicates timestamps throughout the period of the simulation for the different entities of the system. The bottom panel shows the speeds of the CM for the particle, gas, envelope and system in the respective colours as the top panel with the addition of the relative speed between envelope CM and particle CM in black. These curves illustrate the decrease in speed at the end of the plunge in phase and eventually fall towards zero. Moreover Fig. 1.4 shows the CM is not stationary in position but develops an offset due to the energy transfer between the gas and the envelope because of the mass loss.

The archetype of offset CSs, MyCn 18 (Fig. 1.2) was shown recently to be a binary system (Miszalski et al. 2018b). Proper motion might have played a role in the offset of the CS because the direction of the offset system complements the proper motion (Miszalski et al. 2018b). Chamandy et al. (2019) explain that the proper motion may be the cause of asymmetric mass loss that was seen in their simulation which further supports the speculations from Soker (1999). Simulations of Chamandy et al. (2019) suggest post-CE binarity and proper motion may play a role but detailed simulations are required to explore this further.

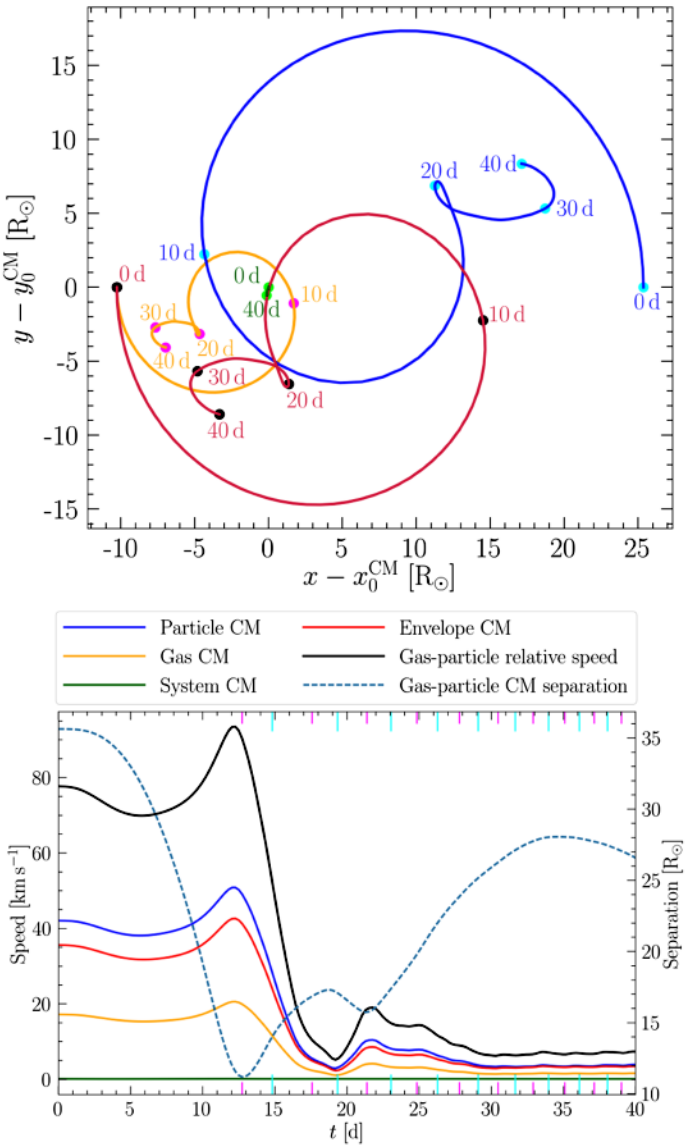

Figure 1.4: *(Top) The CM track of the particle, gas, envelope and system. (Bottom) The speed (km/s) of the CM over the 40 day period with the entities in the same colours as the top panel but including the relative speed between envelope CM and particle CM in black (Chamandy et al. 2019).*

1.4.3 Dual-dust chemistry and dust disks

Dual-dust chemistry is observed through crystalline silicates of [WC] and other type stars and these lines are seen at longer wavelengths of 20 μm (Waters et al. 1998). More evidence of crystalline silicates was observed in Cohen et al. (1999) and Barlow (1998) revealing that the C-rich [WC] nebulae of Hen3-1333 shows strong emission from crystalline olivines, pyroxenes and H_2O ice. Waters and Molster (1999) speculated a large fraction of [WC] CSPNe, showing cool crystalline silicates must still be undiscovered. They further question whether this is a property of PNe in general or if it is restricted to [WC] stars. Understanding the structure and formation of [WC] stars or WR stars in the general sense can help explain correlation of cool oxygen-rich dust to CS spectral type. Dual-dust chemistry has been argued to result from the born-again scenario (De Marco and Soker 2002). In this case an evolved CS that is already on the WD cooling track has a final helium shell flash, quickly returning to the AGB and then evolves along the horizontal track towards the WD phase (De Marco and Soker 2002). Hydrogen deficiency often accompanies dual-dust chemistry, it has been suggested to arise from post-AGB when there is a late thermal pulse (LTP) but not later when the WD cooling track comes into play. De Marco and Soker (2002) show that subsequent H deficiency from dual-dust chemistry should occur all within a short time.

There are three other suggested scenarios that are said to fail or are inadequate to sustain dual-dust chemistry; the single star scenario, a disk scenario, and the Oort cloud scenario (see De Marco and Soker 2002 where they briefly explain why the scenarios fail). De Marco and Soker (2002) proposed two scenarios for dual-dust chemistry, the first is a spiral-in companion and the second considers a stellar companion outside of the envelope. The first of the scenarios has a low-mass companion to the AGB star that deposits gravitational energy and angular momentum. The companion enters the AGB envelope and then spirals in creating a slow wind and fall back material onto the CS (De Marco and Soker 2002). In the second scenario a stellar companion that is outside the envelope shapes the AGB wind and forms a circumbinary disk around the companion (De Marco and Soker 2002). The backflow of material during this process is caused through the enhancement of mass loss and there is spin-up of the AGB. These scenarios have been developed over the years and the consensus is that the CE evolution is not completely understood and this makes it difficult to truly know how such phenomena may come about. Since both scenarios take a companion into account, it is strongly suggested that dual-dust chemistry is connected to binary systems.

The circumstellar disk as previously mentioned is an unlikely cause for dual-dust chemistry but in the event there is dual-dust chemistry a dust-disk may be observed. A circumstellar disk surrounds the stellar system in the form of a torus. The circumstellar disk ties in with dual-dust chemistry since it can host O-rich material for some time after the AGB phase (De Marco and Soker 2002). In later studies Chesneau et al. (2006) explain that a binary companion is required to produce this kind of circumstellar disk. Chesneau et al. (2006) further describe that the formation of such an O-rich disk would be during the early AGB further

agreeing with De Marco and Soker (2002). Cohen et al. (2002) suggests the circumstellar disk to be the reason for dual dust chemistry but De Marco and Soker (2002) imply the disk is not able to describe dust chemistry because they argue it is will likely be a product of stellar companions which develop a common envelope.

1.4.4 Multipolarity

Multipolarity is classically defined in the instance when objects have a minimum of two pairs of axially symmetric structures (Hsia et al. 2019). The first multipolar nebulae were found through a survey of Galactic PNe (Manchado et al. 1989) and K4-55 was discovered to be bipolar (Guerrero et al. 1996). Multipolarity has been studied as a result of the objects that exhibit this feature such as Hen2-47 (Starfish Nebula) and simulations have been conducted to reproduce this structure (Haro-Corzo et al. 2009, Raga et al. 2009, Velázquez et al. 2011). Velázquez et al. (2012) explored multipolarity, noting that bipolar or multipolar PPNe show one or more pairs of elongated structures which are commonly known as lobes. These lobes are ejected material from the CS that may have a global mirror or point symmetric morphology (see Fig. 1.5, middle panel). Multipolar morphologies are believed to result from the presence of a binary system, hence a binary companion is often observed in systems with jets, which are common for PPNe and or lobes of material expelled from the CS. The model for making bipolar PNe and PPNe consists of a bipolar jet outflow or collimated fast winds ejected by one of the binary elements as a result of an accreting disk formed around the star (Morris 1987, Soker and Rappaport 2000). Huang et al. (2020) agrees, stating that the jet and precessing collimated fast winds result from the precessing disk (Fig. 1.6).

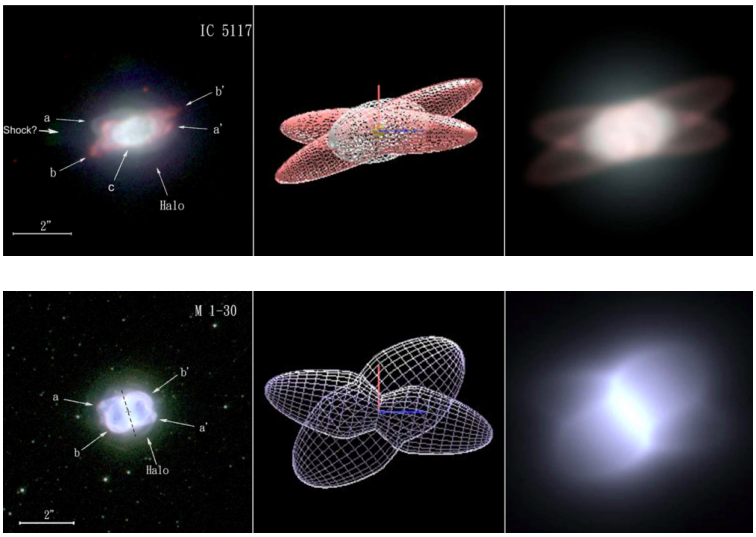

Figure 1.5: *HST image (left), three-dimensional mesh (center), and rendered image (right) of IC 5117 (top) and M 1-30 (bottom) (Hsia et al. 2014).*

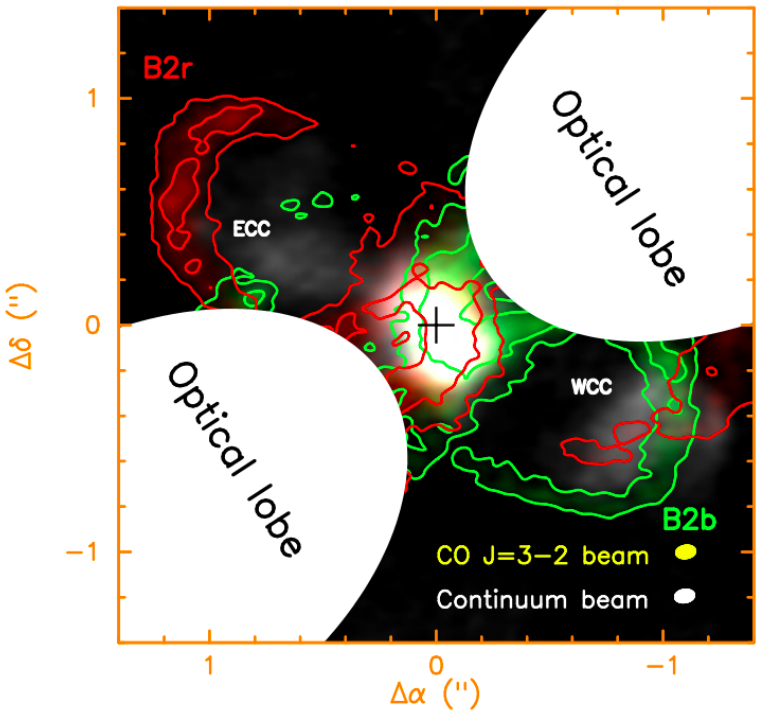

Figure 1.6: *The inner region of I17150 displaying the morphology with the optical lobes indicated and the blue shifted (green contours) and red shifted (red contours) outflows overplotted on a continuum map (grey-scale) (Huang et al. 2020).*

1.4.5 Dust formation

Some CS show dust formation that may be formed from binary interactions. Only a few have been studied (e.g. NGC 2346 Kato et al. 2001; M2-29 and Hen3-1333 Miszalski et al. 2011), while the process has been throughly studied in massive WR stars. The emission line spectra from WR stars result from mass loss through dense, clumpy winds. Williams (2019) states that high density structures in WC winds are important for dust formation. Dust formation is seen through shocks if the winds of the CS collide with massive companions and emission line variations help define what kind of dust producing mechanism is responsible (Williams 2019). The fading circumstellar dust emission (brightening of the stars show similar SEDs to heated dust emission, also sometimes referred to as episodic dust makers), episodic dust makers (stellar wind emission some of the time without any confirmed period) or constant dust makers (these are possible low-amplitude variable dust maker from circular orbit binary systems) are responsible for the presence of dust in these stars. To identify dust formation the criterion used considers the excess flux, this is 10% of the wind flux at 2-4 μm of the specific region (Williams 2019). The authors later concluded that the fading of dust emission is wind speed dependent. The mass loss process dilutes the stellar flux heating such that the dust decreases in temperature. One of the well-studied dust production cases is the WR 104 the Pinwheel nebula, see Fig. 1.7.

Tuthill et al. (2008) described the geometry of WR 104 as having material implanted within a spherical wind that stretches uniformly from the central system. The Pinwheel has been modelled to probe the process responsible for the continuous dust production. The Archimedean spiral model is one such model; a best-fit spiral produced a systematic offset from the core flux. Exploring the role that radiative braking may play in this object, Tuthill et al. (2008) express that for a system that involves a WR and an OB star, where the momentum of the WR wind affects the acceleration environment, it should be considered what role of the OB star luminosity plays with regards to the momentum balance of the WR wind. Sudden wind braking may result from the WR wind and may detain a stagnant point further from OB star.

Other objects that exhibit similar dust variations are R Coronae Borealis (RCB) stars, these are late supergiant stars with variations in their luminosity. The minima are assumed to occur when ejected clouds of carbon condense in the line-of-sight, causing an effect similar to a dust obscuration event (see Fig. 1.8). The atmospheres of the majority of these stars are hydrogen-deficient and are carbon enriched (Pollacco et al. 1992). The composition of the atmospheres are not well understood.

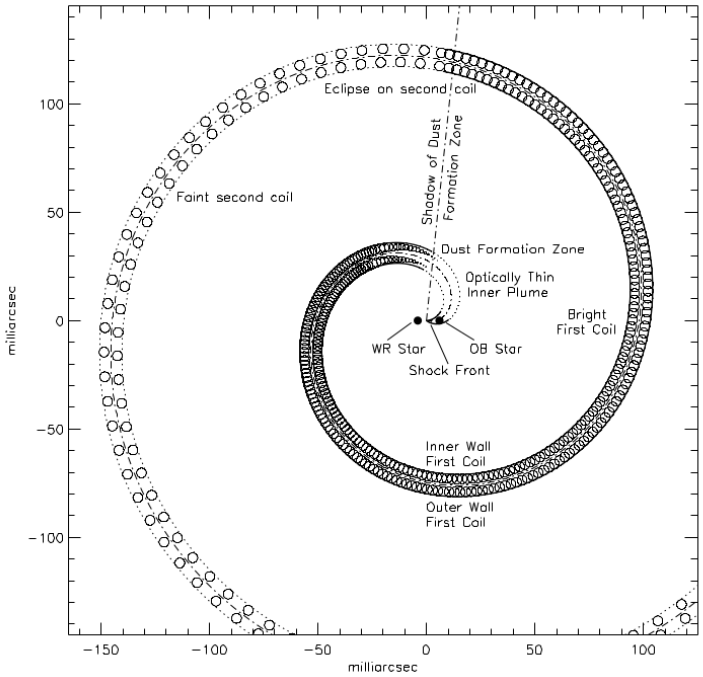

Figure 1.7: *Schematic diagram WR 104, highlighting the import features of the system (Tuthill et al. 2008).*

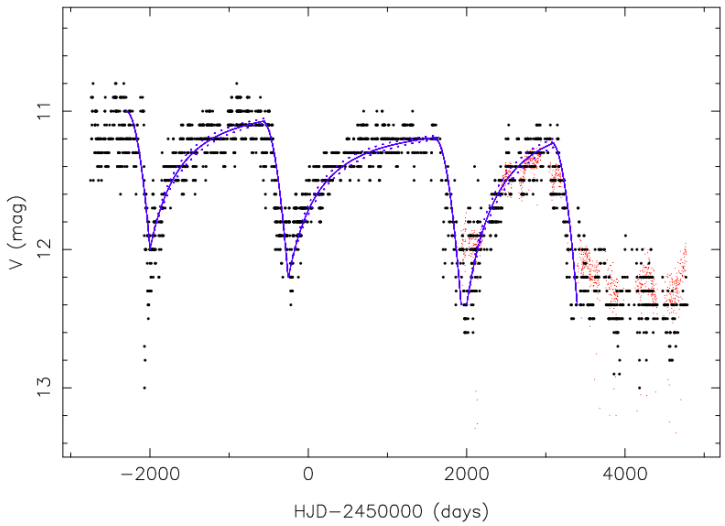

Figure 1.8: *Hen3-1333 observed dust obscuration in the lightcurve where the black points are from Cohen et al. (2002) and the red points are from ASAS (Pojmanski 2002). The blue line is the lightcurve model from Miszalski et al. (2011).*

1.5 PNe studied in this work

The subject of this thesis is the study of three objects chosen because of their interesting features and morphologies. Two of the objects (Hen3-1333, Hen2-113) possesses dual-dust chemistry and all three show multipolar morphologies. All three objects have WR CSs that are bright (Vmag = 11 - 16 mag) and relatively easy to observe with échelle spectrographs. These CSs exhibit strong clumpy dust winds and the multitude of these features and characteristics makes these objects interesting sources to study for binarity.

1.5.1 Hen3-1333

Hen3-1333 has a cool WR CS [WC10] within a multipolar nebula (Fig. 1.9), earlier found with an effective temperature of 30 000 K, a terminal velocity of 225 km/s, and a mass-loss rate of $4\times10^{-6}M_{\odot}$/yr (De Marco and Crowther 1998). Dual-dust chemistry is present and a dust disk was observed from HST images by De Marco et al. (2002a) with an inner radius of 97 $\pm$ 11 AU; Chesneau et al. (2006) used the VLTI to resolve the disk and determine its parameters. The lightcurve (Fig. 1.8) produced in Miszalski et al. (2011) displays variability that is similar to that of RCB stars but that case has extended timescales (Alcock et al. 2001, Tisserand et al. 2008).

Miszalski et al. (2011) further describe a model to explain the lightcurve (Fig. 1.8), and the standard of the fit implies similar physics might relate to fading events in PNe similar to RCB stars. It is suggested dust develops in the inner edge region of the disk but the disks are magnitudes bigger than RCB stars since the ionising field of the CSPN is more powerful such that wind densities are inadequate to yield dust formation (De Marco et al. 2002b). High densities can only be achieved with a dust disk or shock wind interchange with a companion. De Marco et al. (2002b) conclude that obscuration events is rarely observed in PNe and further supports the notion that the dust disk is due to binarity. A confirmed binary of 16 days was found in NGC 2346 where in this case the object is a dust former (Kato et al. 2001).

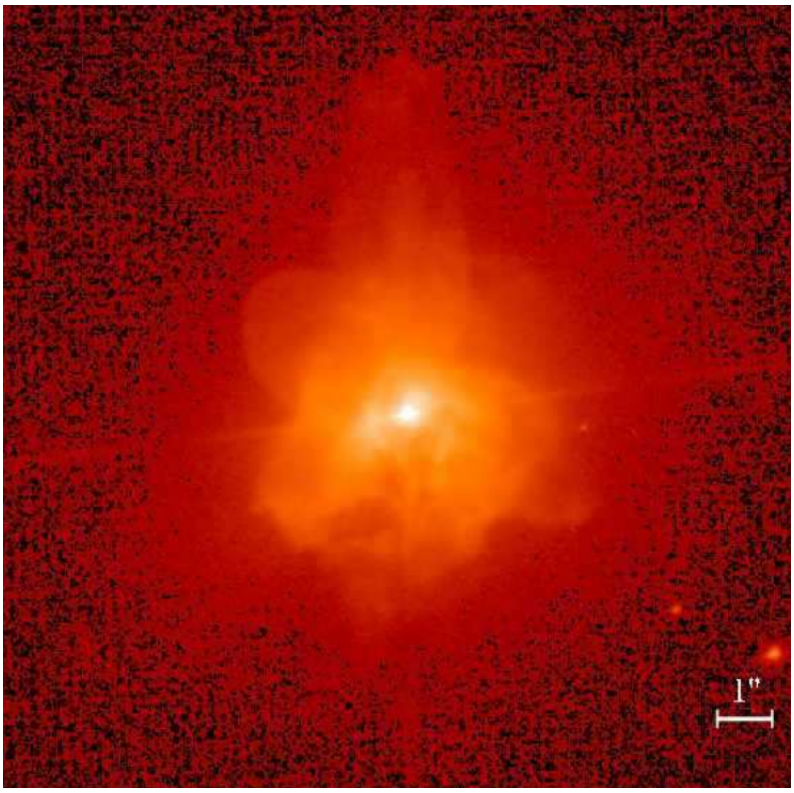

Figure 1.9: *Hen3-1333 (HST, F435). Credit: Chesneau et al. (2006)*

1.5.2 Hen2-113

Hen2-113 is a twin CS to Hen3-1333, namely a [WC10] star (Crowther et al. 1998). Infrared Space Observatory (ISO) spectra show that this object has carbon-rich and oxygen-rich material (Waters et al. 1998), implying dual-dust chemistry. Dual-dust chemistry is often observed in cool [WC]-type CSs (Perea-Calderón et al. 2009), which is the case with this object. de Freitas Pacheco et al. (1993) performed spectroscopy on Hen 2-113, using thermodynamic equations, and concluded that the wind has a carbon-to-helium ratio is C/He = 0.5, which is consistent with the value of 0.55 found by De Marco and Crowther (1998). De Marco and Crowther (1998) based their model on an iterative technique from Hillier (1990) and found a mass loss rate of 3.8 $\times 10^{-6} M_{\odot}$/yr based on the terminal velocity assumption of 1000 km/s. The nebula viewed in the mid-infrared shows bipolar morphology with sharp edges around the lobes (Lagadec et al. 2006). Later, the morphology was shown to be infact multipolar at optical wavelengths (Fig. 1.11, Danehkar and Parker 2015). In the diffuse region, two elliptical rings are observed with the second one appearing only partially (See Fig. 1.10). Lagadec et al. (2006) describe the structure of the second ring that although incomplete, is well defined and parallel to Ring 1. The CS of Hen2-113 is offset and not symmetrically between the rings, further confirming that the CS is does not lie at the centre of the line that joins the NW-SE lobes of the nebula. The chemical composition of this object is similar to those that belong to a group of post AGB stars that have multiple lobes

and a young ionised PN.

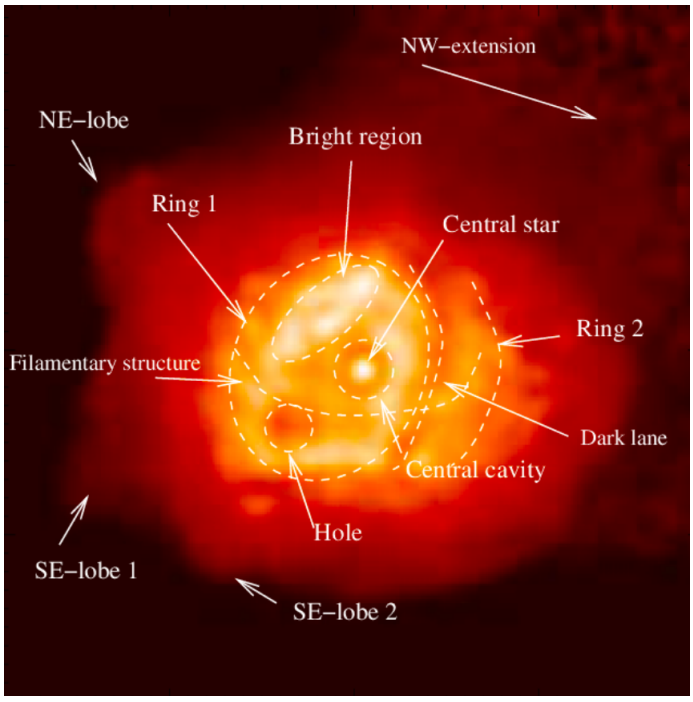

Figure 1.10: *Hen2-113 NACO L band image of the VLT with overlaid schematic describing the main structures of the object (Credit: Lagadec et al. 2006).*

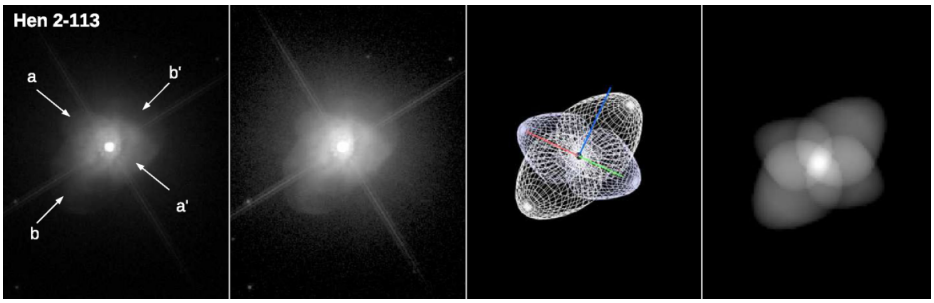

Figure 1.11: *Left panels: The observed HST (F814W filter) images of Hen2-113 based on different contrast levels. Right panels: the* SHAPE *mesh and rendered models of point symmetric lobes for Hen2-113 (Credit: Danehkar and Parker 2015)*

1.5.3 Hen2-47

Hen2-47, also known as the starfish nebula is a multipolar PN containing six major lobes and two bright partial ring-like structures (Fig. 1.12, Sahai 2000). In a similar way to Hen2-113 the CS is offset (Sahai 2000). The multipolar nebula has been modelled by Velázquez et al. (2012) on the effort to understand how the structure formed (see Fig. 1.13). The number of resulting lobes from the models depend on the ratio of precession to orbital periods, q, and variability in the ejection velocity that produces well-defined lobes. The orbital periods found to work with these models are of the order of years and the inclinations assumed are low inclinations ($10° - 30°$) (Velázquez et al. 2012), thus these predictions might explain the properties of Hen2-47.

Figure 1.12: *Hen2-47 optical image illustrating the offset CS and multipolar structure (NASA, ESA, HST Team (STScI/AURA))*

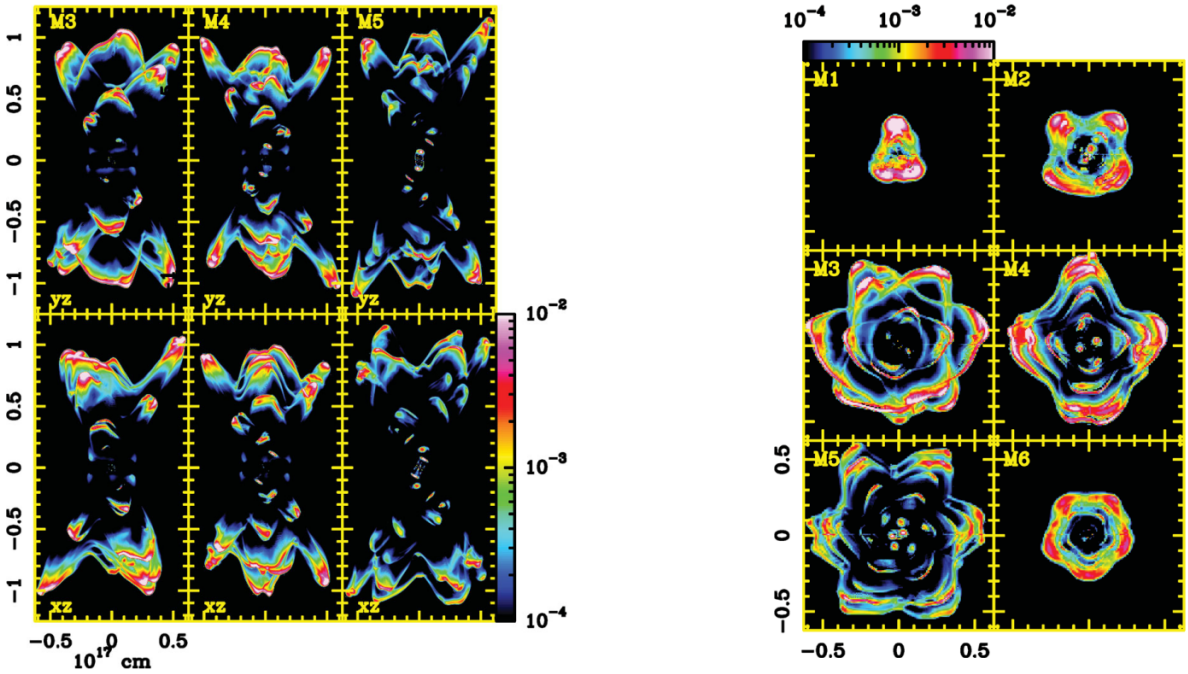

Figure 1.13: *Velázquez et al. (2012) modelled the young multipolar PNe, (Left) Models M3, M4, M5 in that succession. (Right) Models M1-M6 where the z-axis is tilted 90° with respect to the plane of the sky; they find that number of lobes observed relates to the mass ratio, q and the ratio between the precession and orbital periods.*

Chapter 2

Method

In order to determine whether the CSs of Hen3-1333, Hen2-113 and Hen2-47 are binary, we require time-series spectroscopy and photometry. Orbital motion can be probed via periodic RV (spectroscopic) or photometric variability. High resolution time-series spectroscopy from the Southern African Large Telescope (SALT) (Buckley et al. 2006) allows for long term RV monitoring. Space based photometry from The Exoplanet Survey Satellite (TESS) provides improved measurements compared to ground based photometry. It is more sensitive to smaller variability amplitudes and atmospheric conditions do not affect the sampling.

2.1 Telescopes

2.1.1 SALT

We employed the High Resolution Spectrograph (HRS) (Bramall et al. 2010) of the SALT to obtain the spectra of the PNe. The HRS is a dual-beam, fibre-fed échelle spectrograph (Fig. 2.1). The spectrograph is housed in a vacuum chamber which is temperature controlled. VPH gratings act as cross dispersers and the cameras are refractive. The pairs of optical fibres lead to the science target and the background sky. The resolving power of the low resolution (LR) mode is R $\approx$ 14000, a pair which feeds into an image slicer of 500 μm fibres unsliced, the medium resolution (MR) mode is R $\approx$ 40000 for sliced 500 μm fibres from another pair and a third pair delivers a high resolution (HR) of R $\approx$ 70000 sliced. Finally, a High Stability (HS) mode of R $\approx$ 65000 for 350 μm sliced fibres (Barnes et al. 2008). There is one camera each for the blue arm and the red arm. The blue camera has eight lenses and an aperture of 150mm while the red camera which makes use of a fringe suppressing deep depleting CCD has six lenses with an aperture of 170mm (Barnes et al. 2008).

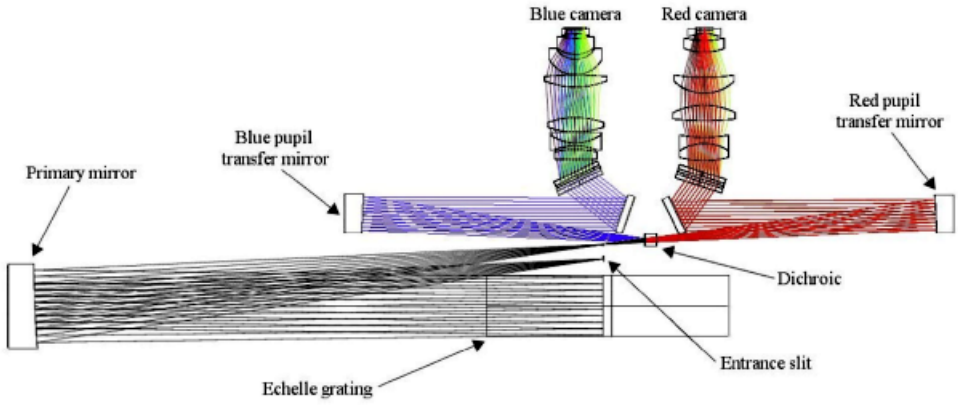

Figure 2.1: *SALT HRS dual beam échelle spectrograph (Barnes et al. 2008).*

2.1.2 TESS

We supplement the SALT HRS observations with well-sampled photometry from TESS. It has continuous sampling recorded every 2 min or less for stars that have been preselected and this goes for all the sectors for an orbit length of 27.4 days (Ricker et al. 2015). This is a photometric survey that has a bandpass of 600 to 1000 nm with a width of 400nm. The bandpass is centered on the I_C band, which runs from 700 - 900 nm, but is wider than it such that it is similar in size to the merging of the R_C (580 - 870 nm), I_C (700 - 900 nm) and z (800 - 1100 nm) bands (Fig. 2.2) (Ricker et al. 2015).

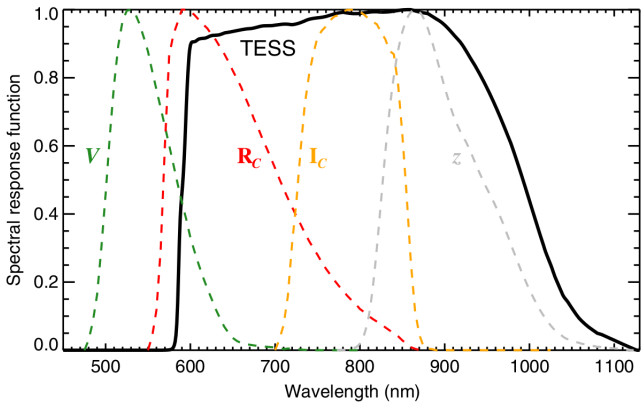

Figure 2.2: *The filter transmission curves displaying TESS coverage (solid line) and the bands that make up the TESS filters (dashed lines) (Ricker et al. 2015).*

The stars selected for observation in the survey are FGKM stars that are adequately bright and small such that transiting planets smaller than Neptune are detected, these stars have required magnitudes of $I_C < 12$ and $I_C < 13$ for FGK stars and M dwarfs, respectively (Ricker et al. 2015). Ricker et al. (2015) explains that four cameras are employed with the north and south ecliptic hemispheres divided into 13 partially overlapping sectors each (see

Fig. 2.3). The scanning strategy sized these sectors as 24 deg × 96 deg extending from an ecliptic latitude of 6 deg to the ecliptic pole (Ricker et al. 2015).

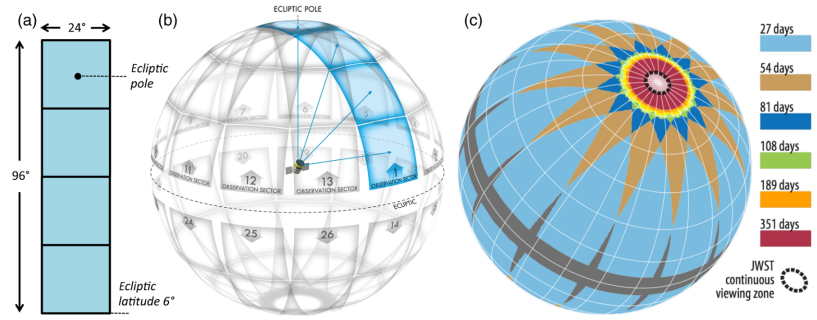

Figure 2.3: *The sectors illustrating the TESS coverage where (a) displays the instantaneous combined field of view of the four TESS cameras. The 26 observation sectors in (b) and (c) is demonstrating the duration of observations given the overlap of the sectors (Ricker et al. 2015).*

2.2 SALT HRS échelle spectroscopy

2.2.1 Observations

The data collected for Hen3-1333, Hen2-113 and Hen2-47 contains 58, 60, and 35 observations, respectively, and were collected over a period of about 3 years (966, 791, 930 days, respectively). These were conducted under the SALT programs 2016-2-SCI-034, 2017-1-MLT-010 and 2018-2-MLT-007 (PI B. Miszalski), Tab. 2.1, 2.2, 2.3. The MR mode for HRS was used which has a wavelength coverage of 3800-8900 Å. This resolution mode was chosen to give sufficient sensitivity to low RV amplitudes, but with a larger fibre which makes it better than the HR mode for brighter sources (O and B spectral type stars) (Crause et al. 2014). Since the objects' magnitudes in this work range between V = 10 − 13 mag, MR mode was most suitable. Regular SALT operations include a bias, ThAr arc and quartz lamp flat field calibrations. The data were processed with PYSALT (Crawford et al. 2010) before being reduced by a MIDAS pipeline (Kniazev et al. 2016). The MIDAS pipeline uses the ÉCHELLE (Ballester 1992) and FEROS (Stahl et al. 1999) packages. We converted the wavelength scale to a logarithmic one in order to setup logarithmic binning for with the cross-correlation task XCSAO. A heliocentric correction was applied to the data to remove the influence of the Earth's orbital position at the time of observation. This correction was applied using VELSET from the RVSAO package (Kurtz and Mink 1998). At this point the data were ready for the two RV determination methods: cross-correlation and Gaussian line fitting, the latter of which required the extra step of preparing text files through the ONEDSPEC package using SCOPY and WSPECTEXT tasks in IRAF[1]. The spectra shown in Fig. 2.4, 2.5, 2.6 are examples, up to the previously mentioned reduction step. The Julian

[1]Image Reduction and Analysis Facility: iraf.noao.edu

dates of the spectra were extracted from the headers, from the heliocentric corrected log files to represent the time in the RV curves.

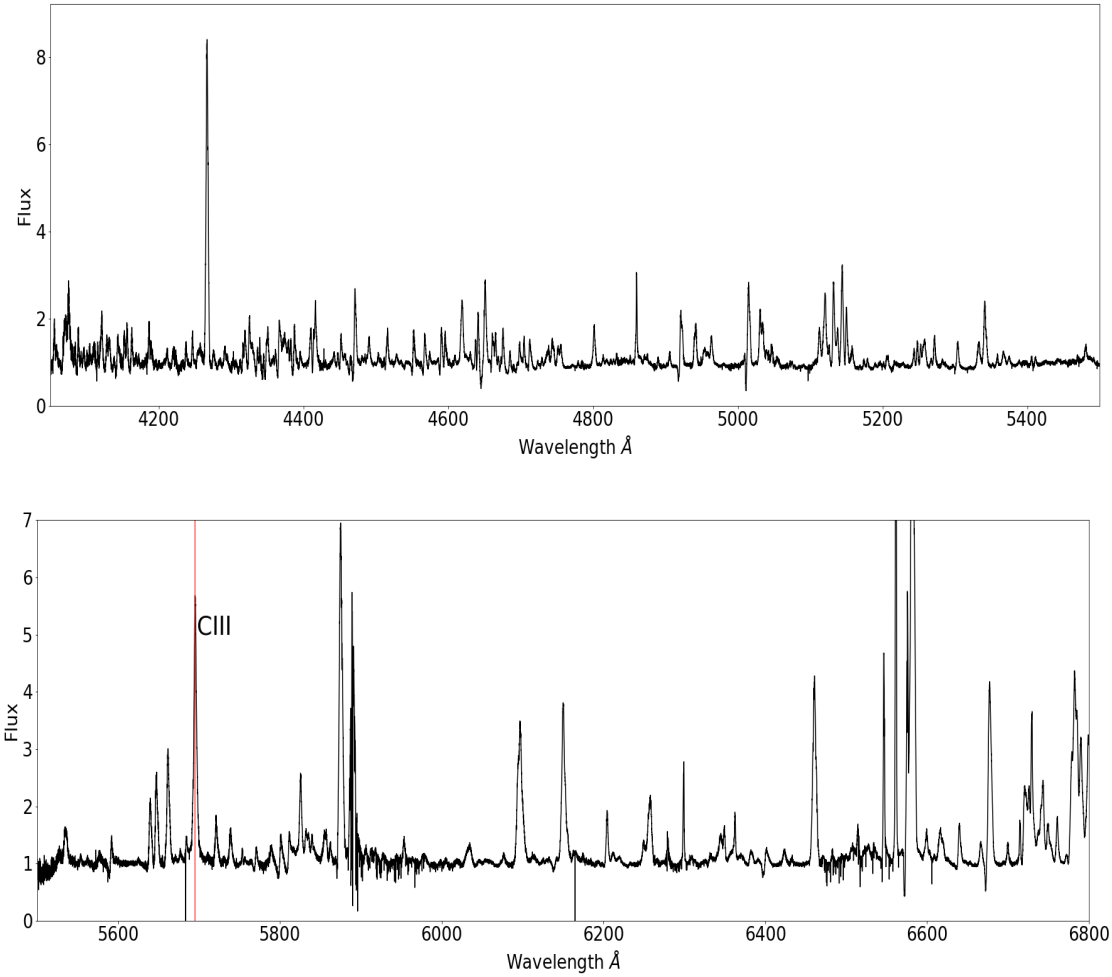

Figure 2.4: *Portions of a representative SALT spectrum of Hen3-1333, the red line indicates the CIII line at 5695* Å.

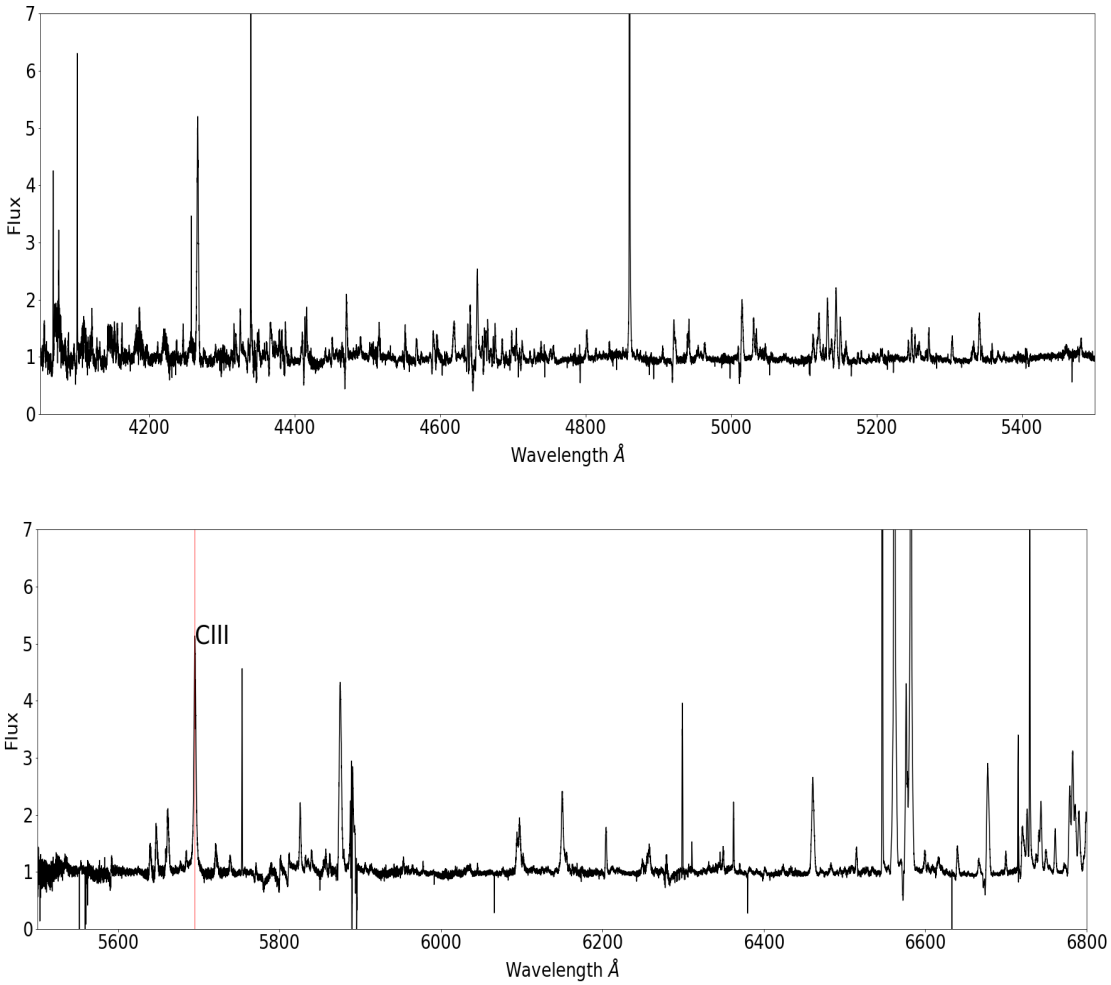

Figure 2.5: *Portions of a representative of Hen2-113 spectrum from SALT, the red line indicates the CIII line at 5695* Å.

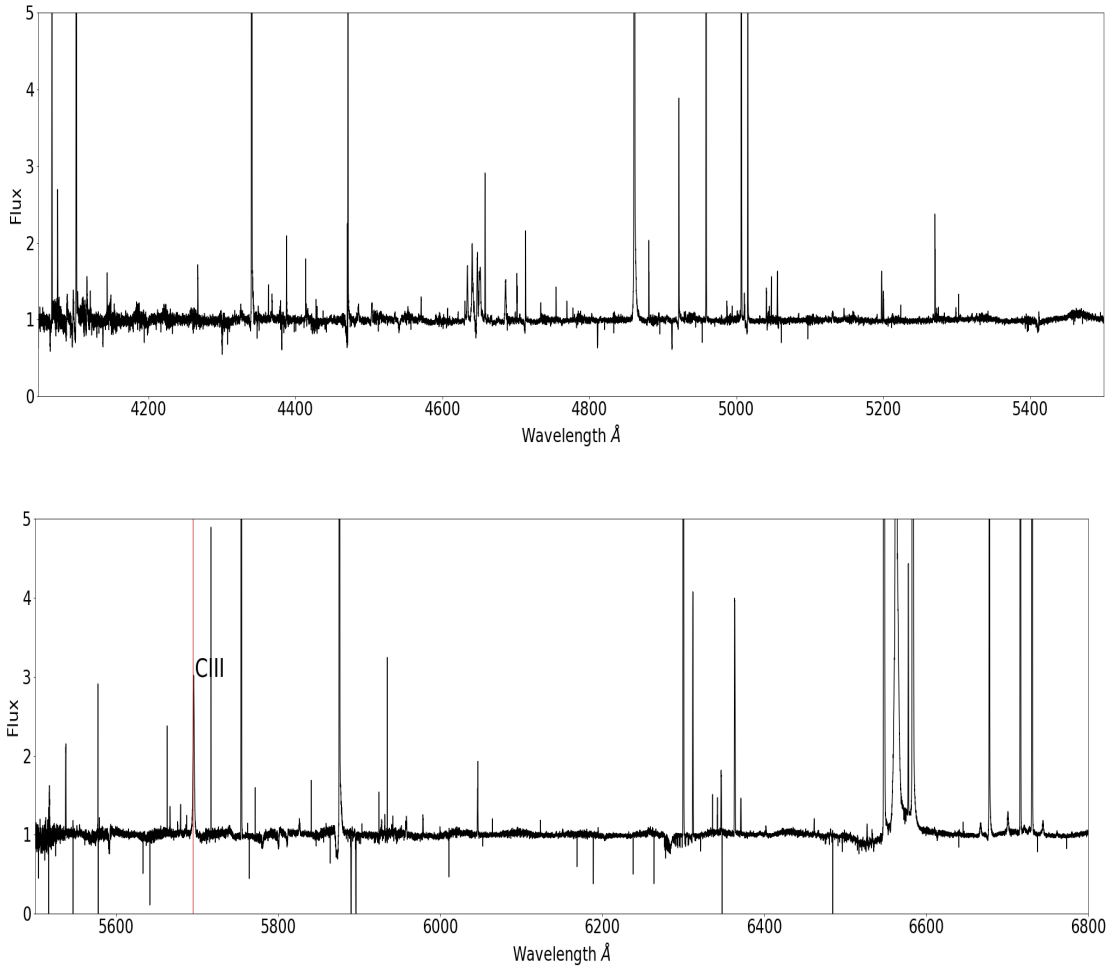

Figure 2.6: *Portions of a representative SALT Spectrum of Hen2-47, the red line indicates the CIII line at 5695* Å.

Table 2.1: *Hen3-1333 observation and Julian dates accompanied with the program proposal IDs (continued in Appendix Table A.1).*

Date of observation	Julian Date	Exposure time (s)	Proposal ID
2017-02-18	2457802.62173	300	2016-2-SCI-034
2017-03-16	2457828.56404	300	2016-2-SCI-034
2017-04-16	2457859.50004	300	2016-2-SCI-034
2017-05-05	2457879.4290	300	2017-1-MLT-010
2017-05-10	2457883.63281	300	2017-1-MLT-010
2017-05-15	2457888.6517	300	2017-1-MLT-010
2017-06-29	2457934.47001	300	2017-1-MLT-010
2017-07-01	2457936.46537	300	2017-1-MLT-010
2017-07-19	2457954.41331	300	2017-1-MLT-010
2017-07-24	2457959.41255	300	2017-1-MLT-010
2017-07-28	2457963.40543	300	2017-1-MLT-010

Table 2.2: *The table of observation and Julian dates for Hen2-113 and the program proposal IDs (continued in Appendix Table A.2).*

Date of observation	Julian Date	Exposure time (s)	Proposal ID
2017-07-01	2457936.42193	600	2017-1-MLT-010
2017-07-03	2457938.4212	600	2017-1-MLT-010
2017-07-21	2457956.36563	600	2017-1-MLT-010
2017-07-26	2457961.35099	600	2017-1-MLT-010
2017-07-30	2457965.30932	560	2017-1-MLT-010
2017-08-02	2457968.30056	560	2017-1-MLT-010
2017-08-03	2457969.32332	560	2017-1-MLT-010
2017-08-05	2457971.30754	560	2017-1-MLT-010
2017-08-06	2457972.30458	560	2017-1-MLT-010
2017-08-07	2457973.30584	500	2017-1-MLT-010
2017-08-08	2457974.27942	500	2017-1-MLT-010

Table 2.3: *Observation and Julian dates for Hen2-47, including the program proposal IDs (continued in Appendix Table A.3).*

Date of observation	Julian Date	Exposure time (s)	Proposal ID
2016-12-15	2457737.52117	1850	2016-2-SCI-034
2017-01-08	2457762.45509	1850	2016-2-SCI-034
2017-02-04	2457789.41243	1850	2016-2-SCI-034
2017-03-06	2457819.34303	1850	2016-2-SCI-034
2017-04-02	2457846.26218	1850	2016-2-SCI-034
2017-04-15	2457859.41783	1850	2016-2-SCI-034
2017-04-19	2457863.3942	1850	2017-1-MLT-010
2017-04-27	2457871.37723	1850	2017-1-MLT-010
2017-05-04	2457878.32189	1850	2017-1-MLT-010
2017-05-09	2457883.36416	1850	2017-1-MLT-010
2017-05-30	2457904.24935	1850	2017-1-MLT-010

2.2.2 Cross-correlation

Cross-correlation is one of the methods used to determine RV shifts between relative spectra to find orbital motion due to a hidden companion. Tonry and Davis (1979) describe the convolution of spectra in the cross-correlation technique. In this case consider a template spectrum, T(n), of zero shift and instrumentally broadened stellar-line profiles. The spectra are discretely sampled into N bins with the label, n, bin number, the true relationship is thus in linear form, $n = Aln\lambda + B$ (Tonry and Davis 1979). This is because the velocity shift is a uniform linear shift binned linearly with lnλ. The cross-correlation function is

$$c(x) = g \times t(x) = \frac{1}{N\sigma_g\sigma_t} \sum_m g(m)t(m-x), \tag{2.1}$$

where t(x) is simply g(x) shifted by d units so that g$\times$t(x) will have a peak 1 at x = d and g(x) is the source spectrum.

The error analysis in the convolution of cross correlating is determined for the shift and

velocity dispersion, also including confidence levels. Generally c(x), the cross-correlation function will have many peaks, and in some cases of low S/N that can distort or exceed the true shift. A peak is selected from data that are indiscretely binned but fitting a smooth curve provides accurate δ, h and ω for the position, height and full-width half-maximum (fwhm) of the peak. The largest errors come from mismatches between the source and template spectra, making the errors from counting statistics insufficient (Tonry and Davis 1979). To account for this mismatch, we regard c(x) as the sum of a perfect correlation function of a broadened, shifted template against template plus a remainder function. The first part provides a peak of exactly the correct width in proper position, and the addition of the second part can distort this peak for the shift error. Considering B to be the highest wave number where the Fourier transform on c(x) has a good amplitude, the mean error is

$$\varepsilon = \Big[x_0\Big(-\frac{4h}{\omega^2}\Big) + \frac{1}{4}\frac{N}{2B}\Big(-\frac{4\sqrt{2}\sigma_a}{\omega^2}\Big) + x_0\Big(-\frac{4\sqrt{2}\sigma_a}{\omega^2}\Big)\Big]\Big/\Big(\frac{4h}{\omega^2} + \frac{4\sqrt{2}\sigma_a}{\omega^2}\Big) - x_0. \tag{2.2}$$

The velocity dispersion requires that the error ω, the FWHM of a second order polynomial be transformed to σ, the intrinsic Gaussian dispersion of the object. Through defining a relationship between ω and γ the width of the Gaussian profile is given by

$$\gamma = f(\omega) \tag{2.3}$$

The dispersion from δ is μ and it is accompanied with the width τ for a typical feature in t(x) and the rms error of dispersion becomes

$$(\Delta\sigma)^2 = 2(\mu^2\Delta\mu^2 + 4\tau^2\Delta\tau^2 + \sigma^4)^{1/2} - 2\sigma^2. \tag{2.4}$$

The above error analysis is a complex approach, but the error analysis developed from the XCSAO task in the package RVSAO is much simpler. Calculating the error as,

$$error = \frac{3}{8}\frac{w}{(1+r)}, \tag{2.5}$$

where *error* is the error in a single velocity measurement, w is the FWHM of the correlation peak and r is defined as a statistic in TD79 (Kurtz and Mink 1998). We adopt this approach to cross-correlation in this work.

2.2.3 Application of cross-correlation on SALT HRS spectra

As a first step to cross-correlation the spectra were normalized. To normalise the spectra the IRAF task CONTINUUM was used. The parameters for the input spectra, order, and interact were set as n.fits, 3 and no, respectively. The process of apodization which is subtracting from the continuum followed after the spectra was normalized. The choice was made to subtract 2.0 from the continuum and the task SARITH was used (see Fig. 2.7). The other parameter change made was setting op = - and input = 2.0. The following step was to deter-

mine the signal-to-noise (S/N) of the spectra. The goal here was to find the spectra with the highest S/N to use as the reference template. I measured the S/N for each spectra with the SPLOT task, by pressing m on either side of a small wavelength window (Fig. 2.8). I changed the dispersion axis and headers by setting the dispersion axis to 1 and set the VELOCITY keyword to 0. Next followed the cross-correlation steps using the task XCSAO in the package RVSAO. I chose the start and end wavelength parameters but these were determined after a few iterations starting with 5625-5740 Å. I finally settled on the wavelength range 5500 − 6200 Å for the red spectra and 4200 − 5400 Å for the blue spectra which include strong carbon and oxygen lines. I chose the final parameters to include a wider range of lines but not including the Hα as this would have compromised the measurements because the line is strong enough to add to the variability and it originates from the nebula further away from the CS.

I set the template parameter as an initial reference template ($T_{ref}(n)$) which was the spectrum with the highest S/N. I set the velocity correction for the spectra and template to none as the spectra already went through heliocentric correction. I extracted the XCSAO log velocities and used it to shift the spectra to compile the final template by changing the velocities in the header to the new ones and using the VELSET task. I then plotted the spectra and stacked them with SPECPLOT to verify that it all synced up well. I combined the spectra thereafter to create the final template ($T_{final}(n)$, Fig. 2.9) with the task SCOMBINE (Fig. 2.10). I ran the XCSAO task again, this time with the template parameter set as the final template ($T_{final}(n)$) created in the previous step (Fig. 2.11). The final cross-correlation velocities were determined along with the uncertainties for the RV curve (see Tab. 2.4, 2.5, 2.6). Overall the main steps for cross-correlation were the following:

- Normalize the spectra.
- Determine the initial reference template as the spectrum with the highest S/N.
- Cross correlate the rest of the data using XCSAO through the RVSAO package.
- Combine the spectra and determine the template for the final cross-correlation velocities.
- Run the final cross-correlation with the final template.

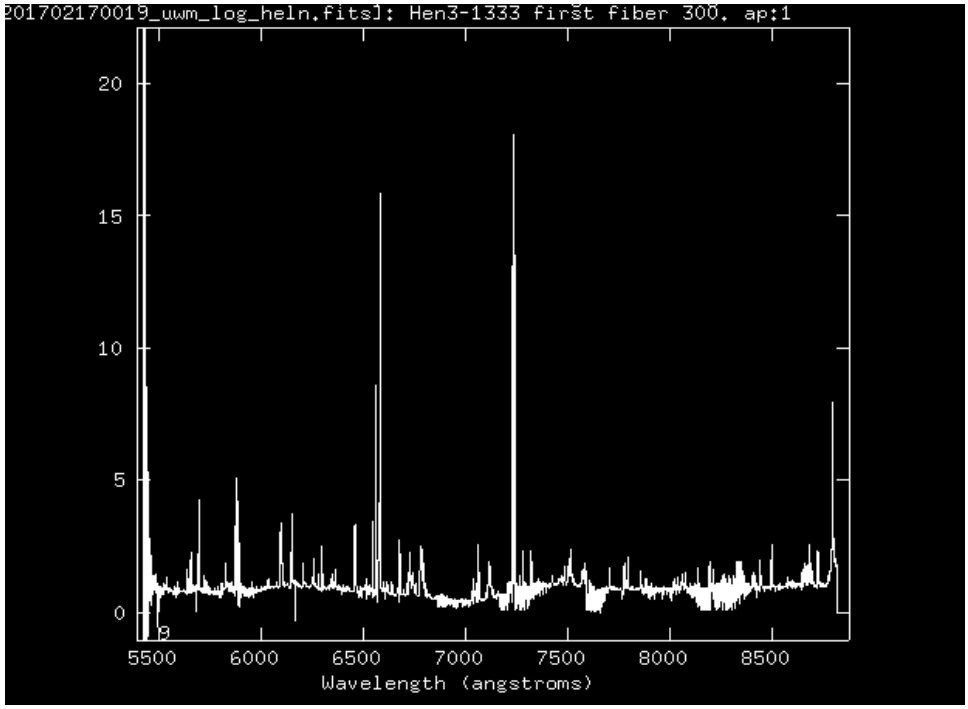

Figure 2.7: *A normalized red spectrum of Hen3-1333.*

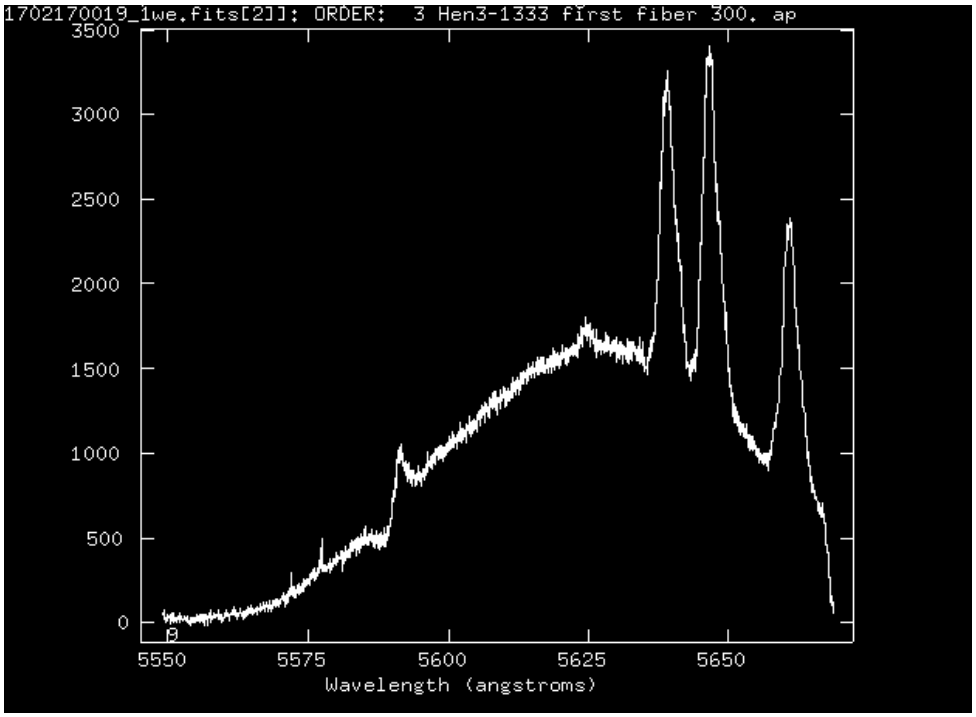

Figure 2.8: *The 3rd individual order spectrum of Hen3-1333 used to determine the S/N.*

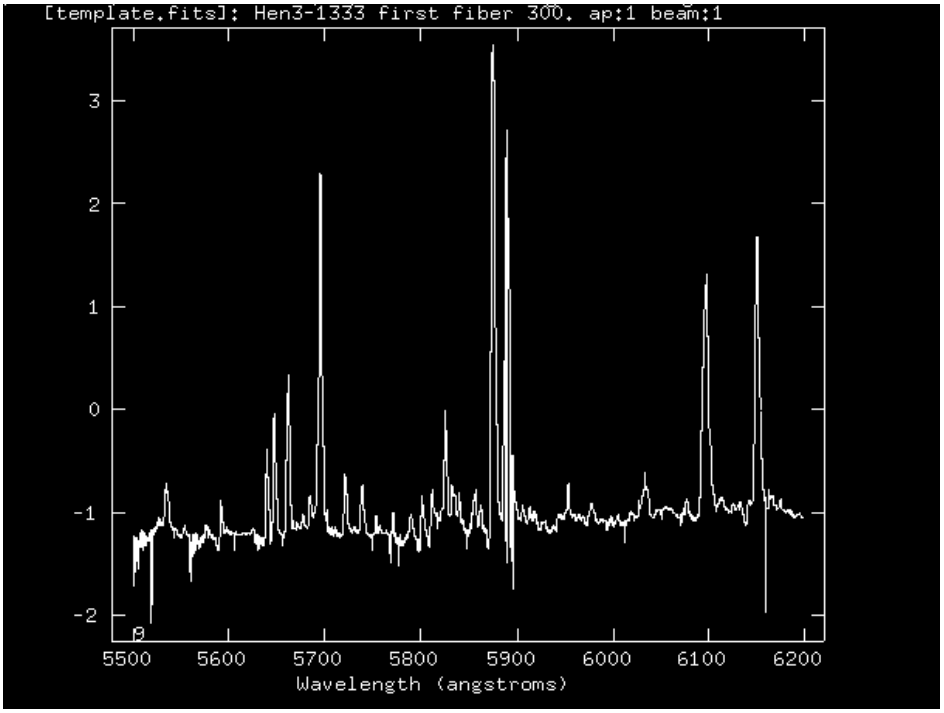

Figure 2.9: *The final built template of Hen3-1333 ready for cross-correlation.*

```
                                  I R A F
                     Image Reduction and Analysis Facility
PACKAGE = specred
   TASK = scombine

input   = □           *s1.fits  List of input spectra
output  =       template.fits  List of output spectra
(noutput=                   ) List of output number combined spectra
(logfile=              STDOUT) Log file

(apertur=                   ) Apertures to combine
(group  =           apertures) Grouping option
(combine=             average) Type of combine operation
(reject =                none) Type of rejection

(first  =                  no) Use first spectrum for dispersion?
(w1     =               5500.) Starting wavelength of output spectra
(w2     =               6200.) Ending wavelength of output spectra
(dw     =               INDEF) Wavelength increment of output spectra
(nw     =               INDEF) Length of output spectra
(log    =                  no) Logarithmic increments?

More
                                                        ESC-? for HELP
```

Figure 2.10: *The* IRAF *task* SCOMBINE *used to combine the spectra and build the template of Hen3-1333 according to the parameters.*

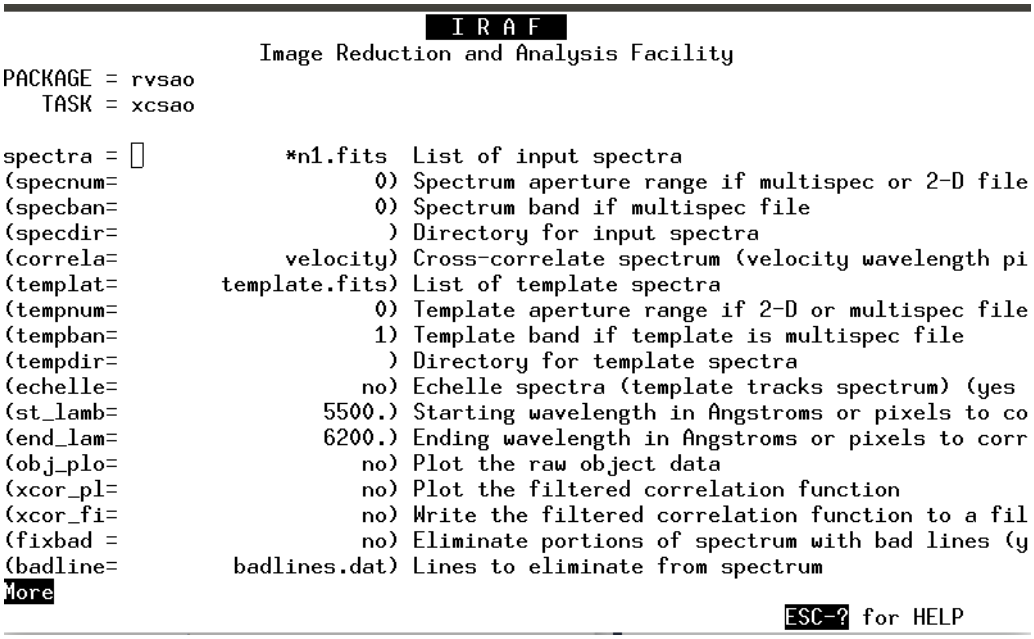

Figure 2.11: *The* IRAF *task* XCSAO *used to determine cross-correlation velocities according to the parameters displayed (i.e. the built template, wavelength range 5500 − 6200 A) for Hen3-1333.*

Table 2.4: *Hen3-1333 cross-correlation velocities for the blue and the red SALT spectra (continued in Appendix Table A.4).*

	Blue		Red	
Julian Date JD	RV (km/s)	σ (km/s)	RV (km/s)	σ (km/s)
2457802.62173	−0.63	1.11	−0.35	0.64
2457828.56404	−0.47	1.03	−2.55	0.71
2457859.50004	3.86	0.66	0.97	0.81
2457879.429	−0.80	0.63	−0.49	0.65
2457883.63281	3.76	1.22	2.84	0.64
2457888.6517	−4.08	1.13	−1.73	0.65
2457934.47001	−1.85	3.38	−1.86	0.63
2457936.46537	0.59	0.63	−0.40	0.53
2457954.41331	0.14	1.00	−0.30	0.47
2457959.41255	−0.85	0.95	0.02	0.89
2457963.40543	2.59	1.16	1.58	0.53

Table 2.5: *The cross-correlation velocities of Hen2-113 for the blue and red SALT spectra (continued in Appendix Table A.5).*

	Blue		Red	
Julian Date JD	RV (km/s)	σ (km/s)	RV (km/s)	σ (km/s)
2457936.42193	2.36	0.64	−3.75	0.66
2457938.4212	2.23	0.65	−5.98	0.77
2457956.36563	3.76	0.62	−0.47	0.52
2457961.35099	0.88	0.59	−10.13	0.51
2457965.30932	0.72	0.43	−8.78	0.49
2457968.30056	2.26	0.52	−4.43	0.55
2457969.32332	2.18	0.58	−5.61	0.55
2457971.30754	1.15	0.69	−6.73	0.77
2457972.30458	2.27	0.73	−3.98	0.60
2457973.30584	2.79	0.56	−6.02	0.50
2457974.27942	3.97	0.65	−0.25	0.65

Table 2.6: *Hen2-47 cross-correlation velocities for the SALT blue and red spectra (continued in Appendix Table A.6).*

	Blue		Red	
Julian Date JD	RV (km/s)	σ (km/s)	RV (km/s)	σ (km/s)
2457737.52117	0.49	0.29	−0.22	0.41
2457762.45509	0.18	0.23	−0.38	0.10
2457789.41243	0.28	0.23	−0.23	0.27
2457819.34303	0.69	0.11	−0.56	0.33
2457846.26218	0.89	0.26	−0.95	0.23
2457859.41783	0.77	0.30	−0.25	0.70
2457863.3942	0.79	0.26	−0.46	0.29
2457871.37723	0.69	0.07	−1.25	0.37
2457878.32189	0.68	0.11	−0.84	0.41
2457883.36416	0.52	0.25	−0.25	0.17
2457904.24935	0.54	0.12	−0.21	0.47

2.2.4 Gaussian line fitting

Gaussian fitting is individual line fitting of the absorption and emission lines from the spectra. Individual line fitting is important because some lines may be more sensitive to orbital variability. Here we used the CIII emission line, which is very sensitive to wind clumping and is sensitive to density enhancements (Moffat 1996). CIII is thus a good density tracer and is usually used in massive WR binaries (Bartzakos et al. 2001).

The LMFIT fitting module was used in PYTHON (Newville et al. 2016). LMFIT implements the Levenberg Marquardt fitting technique for non-linear optimization and curve fitting. Gaussian, Lorentzian and Voigt fitting profiles are available in the module and the Gaussian profile was fit to the CIII line at 5695 Å in the red spectra. The Gaussian function best fit the line profile. We explored an alternative Voigt function, but this over-fitted the line profile.

Once the choice of fitting function was made, the wavelength range was set to include the carbon line and thereafter initial parameters for the technique such as min and max wavelength ($<$ 10 Å on either side of the CIII line). Running the code produced a fit report which included a χ square value and the centre wavelength with uncertainty of the fit amongst other parameters. The central wavelength was used in the Doppler formula to determine the velocity of the line

$$v = \frac{c(\lambda - \lambda_0)}{\lambda_0}, \tag{2.6}$$

where λ is the central wavelength from LMFIT and λ_0 is the literature value of the central wavelength of CIII (5695 Å) and c is the speed of light. Fig. 2.12, 2.13, 2.14 displays an example of the line profile fit and the RVs with errors can be seen in Tab. 2.7, 2.8, 2.9.

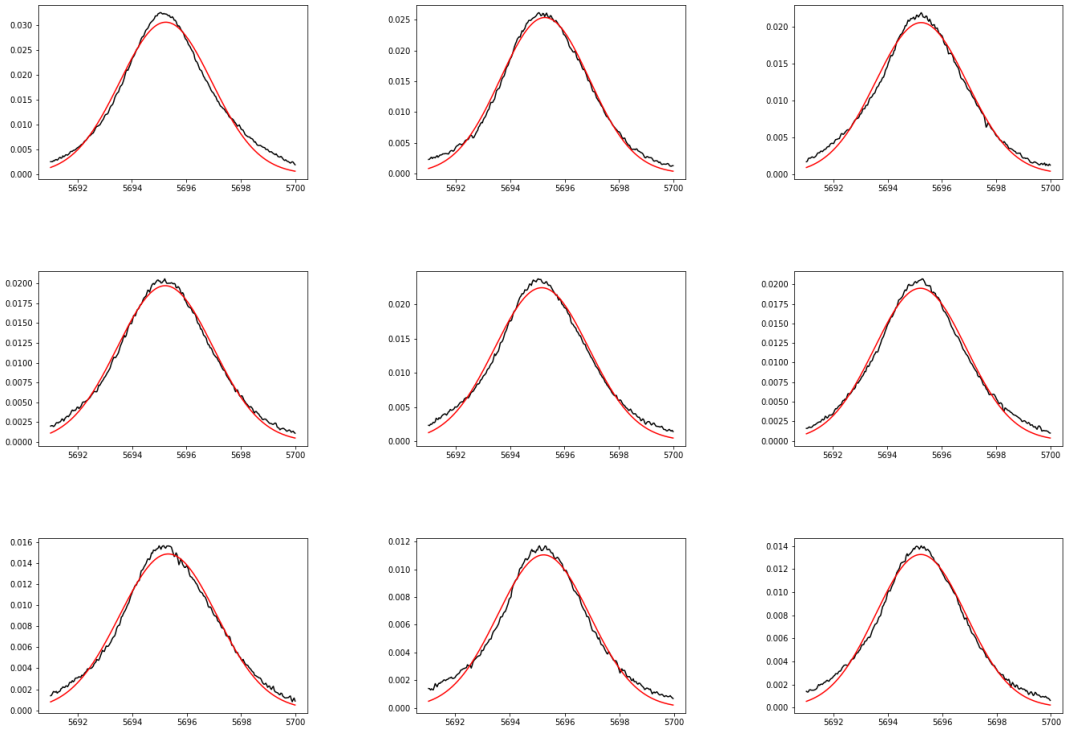

Figure 2.12: *Hen3-1333 Gaussian fit lines (red line) for 9 of the 58 spectra. Fit on CIII (5695 Å) with wavelength (Å) on the x axis and normalized flux on the y axis.*

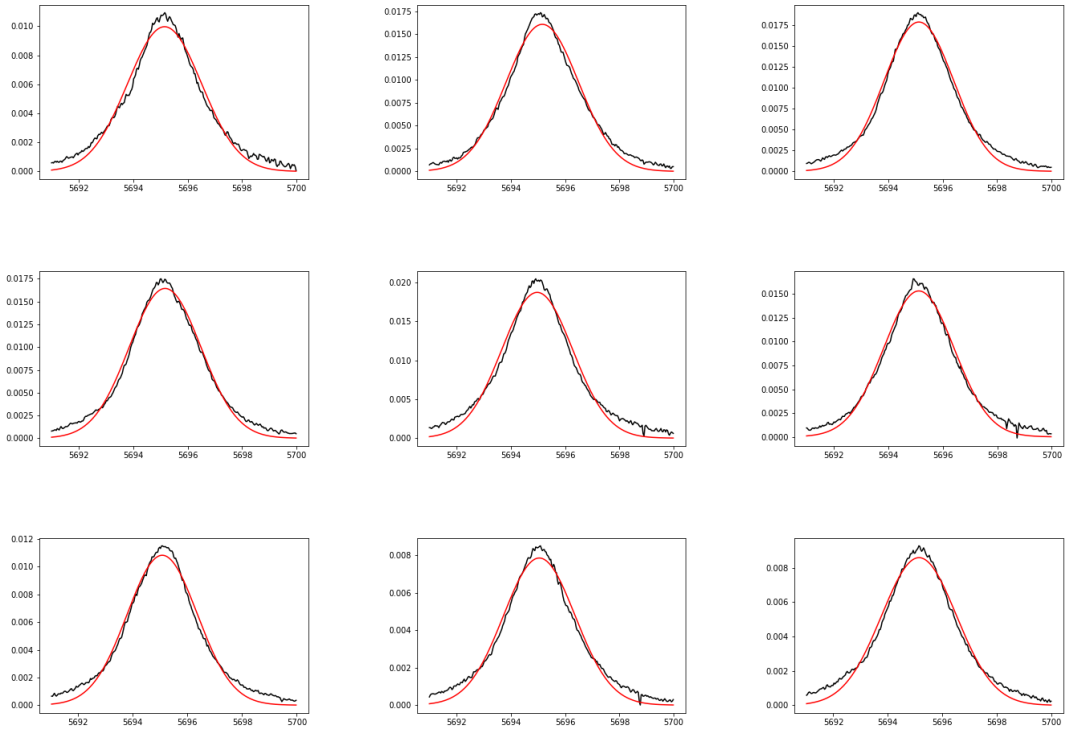

Figure 2.13: *Hen2-113 Gaussian fit lines (red line) for 9 of the 60 spectra. Fit on CIII (5695 Å) with wavelength (Å) on the x axis and normalized flux on the y axis.*

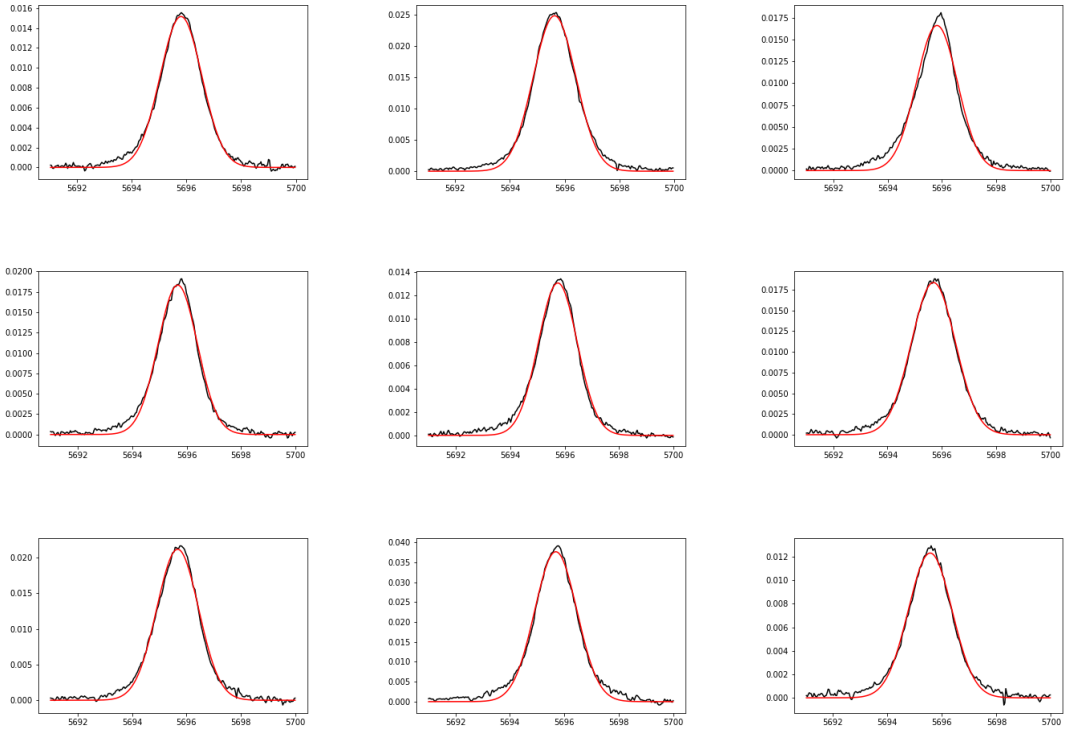

Figure 2.14: *Hen2-47 Gaussian fit lines (red line) for 9 of the 35 spectra. Fit on CIII (5695 Å) with wavelength (Å) on the x axis and normalized flux on the y axis.*

Table 2.7: *Hen3-1333 CIII line (5695 Å) Gaussian profile velocities. (continued in Appendix Table A.7).*

Julian Date JD	RV (km/s)	σ (km/s)
2457802.6217	-37.67	0.43
2457828.5640	-39.11	0.64
2457859.5000	-42.30	0.44
2457879.4290	-37.56	0.52
2457883.6328	-39.96	0.52
2457888.6517	-34.86	0.50
2457934.4700	-32.44	0.51
2457936.4654	-34.14	0.43
2457954.4133	-35.88	0.46
2457959.4126	-43.09	0.54

Table 2.8: *Hen2-113 CIII line (5695 Å) Gaussian profile velocities. (continued in Appendix Table A.8).*

Julian Date JD	RV (km/s)	σ (km/s)
2457936.4219	-42.83	0.38
2457938.4212	-42.00	0.38
2457956.3656	-37.14	0.49
2457961.3510	-46.96	0.41
2457965.3093	-45.85	0.44
2457968.3006	-49.85	0.46
2457969.3233	-39.11	0.49
2457971.3075	-46.99	0.44
2457972.3046	-44.74	0.46
2457973.3058	-40.69	0.37

Table 2.9: *Hen2-47 CIII line (5695 Å) Gaussian profile velocities. (continued in Appendix Table A.9).*

Julian Date JD	RV (km/s)	σ (km/s)
2457737.5212	-12.55	0.28
2457762.4551	-7.11	0.23
2457789.4124	-6.34	0.19
2457819.3430	-12.94	0.18
2457846.2622	-12.87	0.20
2457859.4178	-10.74	0.29
2457863.3942	-15.19	0.44
2457871.3772	-6.39	0.17
2457878.3219	-12.57	0.20
2457883.3642	-15.18	0.15
2457904.2494	-8.47	0.43

2.3 TESS lightcurves

As our objects were not part of the dedicated program, no pipeline reduced lightcurves were available. We had to extract our own using SPOC[1] and LIGHTKURVE (Barentsen and Lightkurve Collaboration 2020) from the raw data. The overview of the pipeline processes are as follows:

- Raw pixels are processed.
- Photometry and astrometry is extracted for each target.
- Systematic errors are identified and removed.
- Transiting planet signatures are flagged.
- Diagnostic tests are performed.

[1]Science Processing Operations Center: Jenkins et al. (2016)

The following outputs are produced from SPOC: target pixel files which are raw and calibrated pixel data, target lightcurve files which include photometric analysis and systematic error-corrected time-series data. Along with full frame images (FFI), these are raw, calibrated, and uncertainty images of the CCDs. The pipeline produces collateral pixel files which include raw and calibrated collateral pixel data. The data validation products are among the outputs and ancillary files that include pipeline meta-data and co-trending basis vectors. The FFIs of stars with a 2 min cadence are collected every 30 mins and calibrations are done through the pipeline SPOC. The objects in this research were recovered through the proposals from G. Ricker with the IDs tess-s0011-2-3, tess-s0012-2-4, tess-s0010-3-1, tess-s0011-3-2, tess-s0012-2-3 (Table. 2.10). The Python packages ELEANOR (Feinstein et al. 2019), LIGHTKURVE and TARGET SEARCH work well to search and retrieve objects through the pipeline, but LIGHTKURVE is especially good for objects that do not have a 2 min cadence such as our objects. The cadence of observations for our objects is therefore 30 min.

Table 2.10: *The TESS data observation details of Hen3-1333, Hen2-113 and Hen2-47.*

Object	Observation dates	Observation ID	Exposure time (s)
Hen3-1333	21/05/2019 - 19/06/2019	tess-s0012-2-3	1425.599394
Hen2-113	22/04/2019 - 26/05/2019	tess-s0011-2-3	1425.599394
	21/05/2019 - 19/06/2019	tess-s0012-2-4	1425.599394
Hen2-47	26/03/2019 - 22/04/2019	tess-s0010-3-1	1425.599391

2.3.1 Producing TESS lightcurves with LIGHTKURVE

The data for the lightcurves were downloaded through the MAST portal using modified Python code that interfaced with LIGHTKURVE. The detailed steps were as follows: I imported LIGHTKURVE to search the database for the object using SEARCH TESSCUT (Brasseur et al. 2019) for the cut frame since my objects do not have a 2 min cadence (in our case 30 min). I downloaded the data and created a target mask for plotting the data as pixels (Fig. 2.15). At this point I transformed the pixel data to a lightcurve and plotted the lightcurve which included the target and the background. I created a background mask to remove the background pixels in the image and determined an estimated background lightcurve which is the product of the background lightcurve per pixel and the number of pixels from the target. I plotted the lightcurve of the object with the extracted background lightcurve along with it (Fig. 2.16). Thereafter I determined a corrected lightcurve by subtracting the background from the target and plotted this as flux $[e^{-}s^{-1}]$ vs time-2457000 [Barycentric Julian Days] (Fig. 2.17). The magnitude-flux equation (Eq. 2.7) was used to convert the units from flux to magnitudes. A reference system (m_{ref} = 10, f_{ref} = 15000 $e^{-}s^{-1}$) was used in this equation[1] and the final (in magnitudes) lightcurves for Hen3-1333, Hen2-113 and Hen2-47 were plotted (see Fig. 2.18, 2.20, 2.22),

$$m - m_{ref} = -2.5log_{10}(f/f_{ref}). \tag{2.7}$$

[1]https://heasarc.gsfc.nasa.gov/docs/tess/observing-technical.html

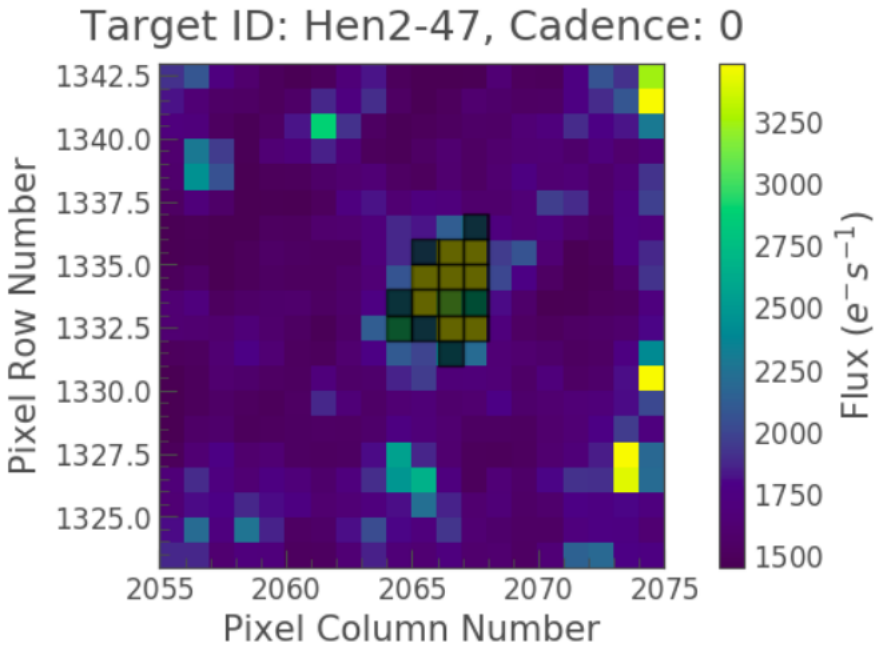

Figure 2.15: *Target pixel image of the Hen2-47 region with the pixel masks overlaid.*

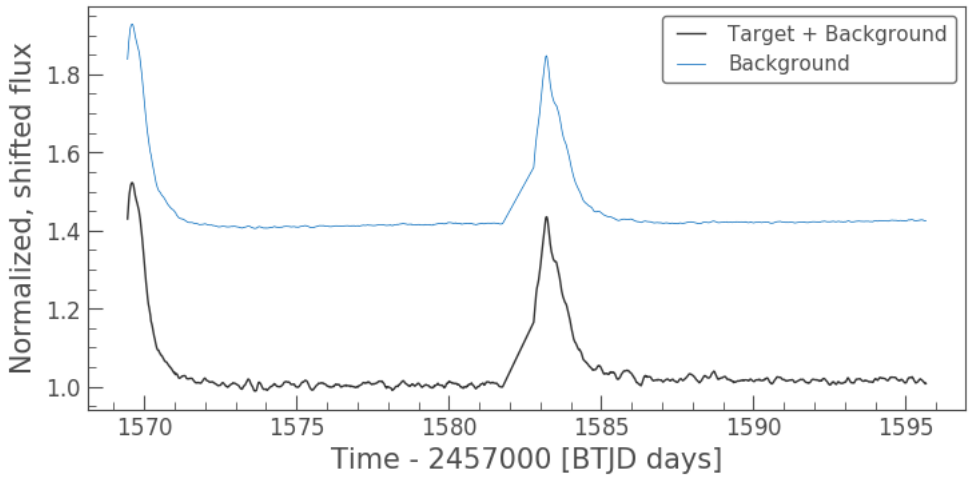

Figure 2.16: *The lightcurve of Hen2-47 as represented by the target and the background in normalized flux.*

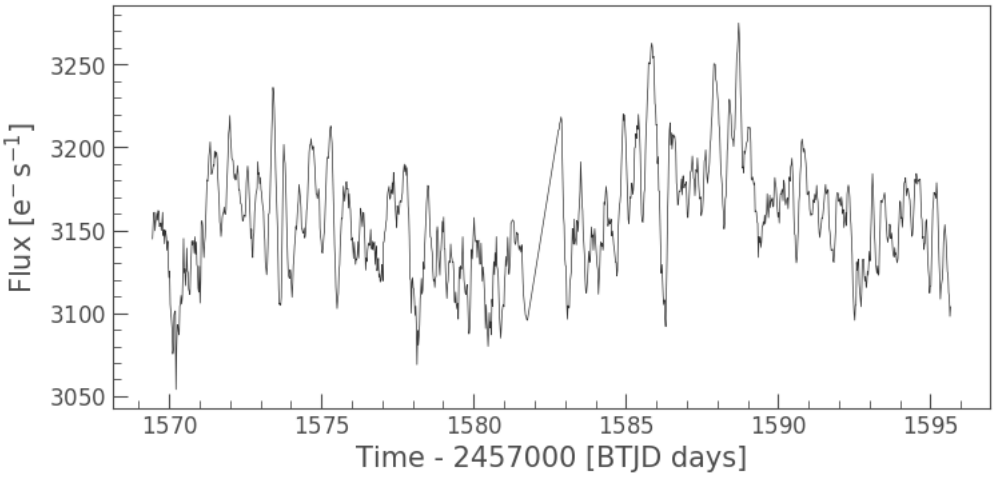

Figure 2.17: *The lightcurve of Hen2-47 in flux as received from the raw data.*

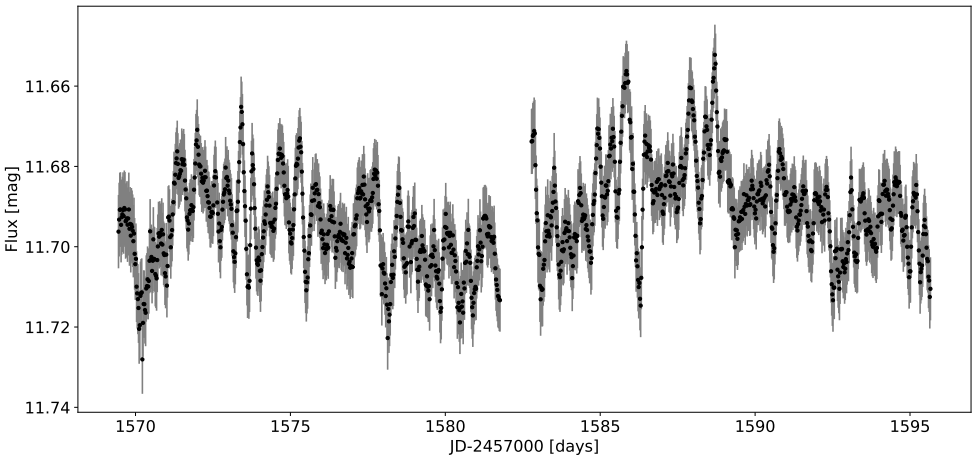

Figure 2.18: *Hen2-47 TESS lightcurve.*

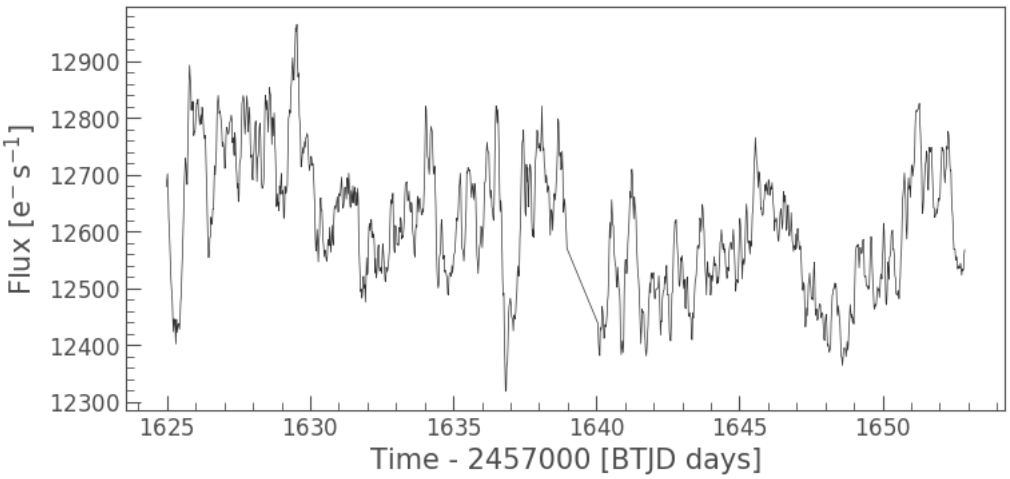

Figure 2.19: *The lightcurve of Hen3-1333 in flux as received from the raw data.*

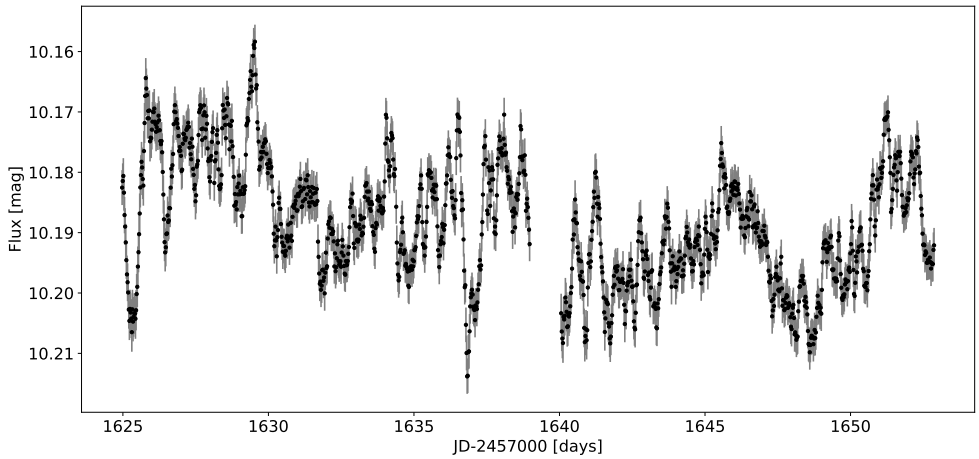

Figure 2.20: *Hen3-1333 TESS lightcurve.*

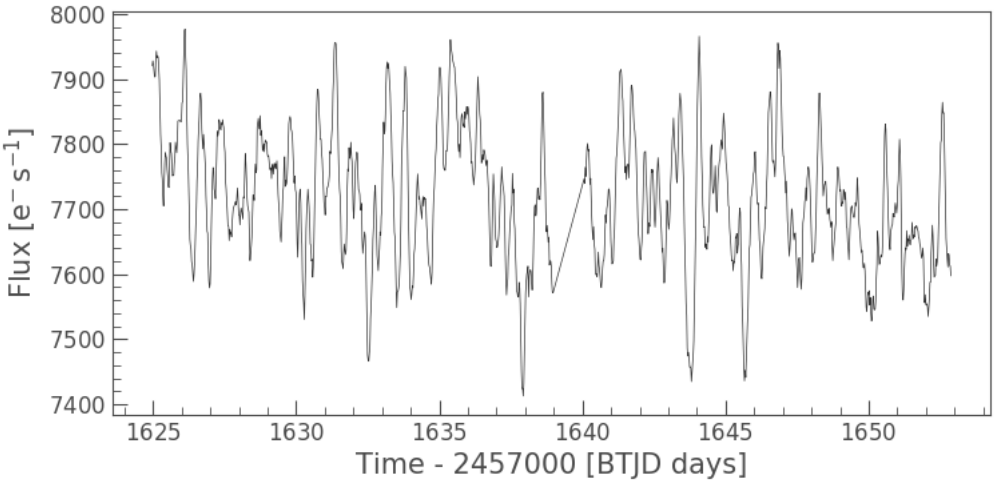

Figure 2.21: *The lightcurve of Hen2-113 in flux as received from the raw data.*

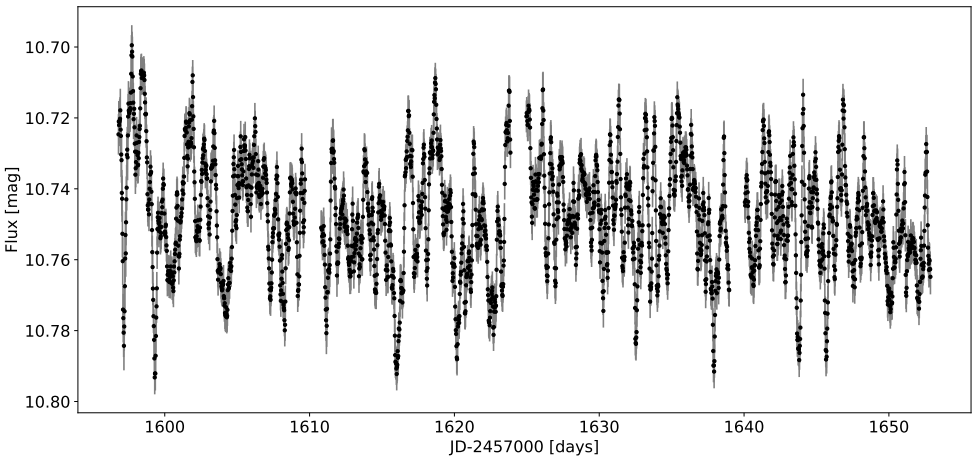

Figure 2.22: *Hen2-113 TESS lightcurve.*

2.4 Data quality

The SALT spectra were utilized in two ways, determining the RV through cross-correlation and Gaussian profile line fitting with the Doppler method. Investigating how these velocities correlate is important to check whether there may be any obvious sources of systemic errors. The correlation plots are displayed in Fig. 2.23, 2.24, 2.25.

The velocities for Hen3-1333 appear to be correlated because of the clumping seen in Fig. 2.23. There are a few outliers but the result supports the robust nature of the measurements. Hen2-113 (Fig. 2.24) shows a similar clumped scatter for the velocities but Hen2-47 (Fig. 2.25) is less correlated than the previous objects. The scatter seen from Hen2-47 could be a result from strong winds causing a larger scatter in the variability from the spectral lines, in particular CIII 5695 Å, since its variability is much greater than the cross-correlation results (Fig. 3.3).

Another check of the quality of the spectra is the S/N, which was measured on the individual spectral separate orders data product of the MIDAS pipeline. Fig. 2.26 (left panel) displays the S/N of the blue order spectra plotted against the cross-correlation velocities (taken from the 4200 - 5400 Å range). The red order spectra S/N are plotted against both the corrected cross-correlation velocities (5500 - 6200 Å) (Fig. 2.26 right panel) and the Gaussian line velocities (Fig. 2.27). The velocities in the plots have larger errors at lower S/N values, in which case the noise is larger than the signal. The rest of the spectra however have very good S/N values which suggest quality spectra.

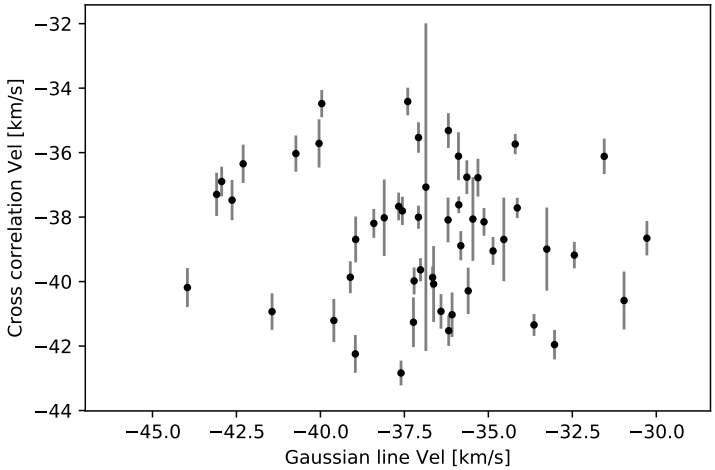

Figure 2.23: *The cross-correlation velocity from the 5500 – 6200* Å *range plotted against the Gaussian profile velocity of the CIII line at 5695* Å *for Hen3-1333.*

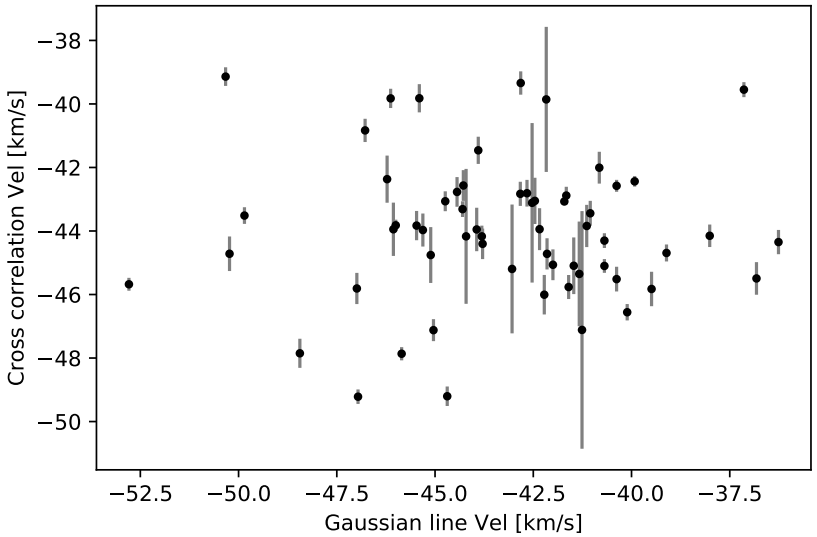

Figure 2.24: *The cross-correlation velocity from the 5500 – 6200* Å *range plotted against the Gaussian profile velocity of the CIII line at 5695* Å *for Hen2-113.*

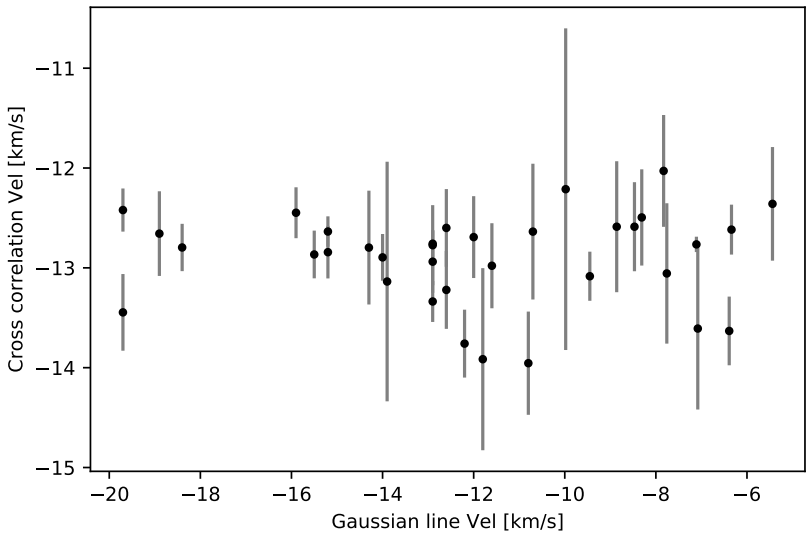

Figure 2.25: *The cross-correlation velocity from the 5500 – 6200* Å *range plotted against the Gaussian profile velocity of the CIII line at 5695* Å *for Hen2-47.*

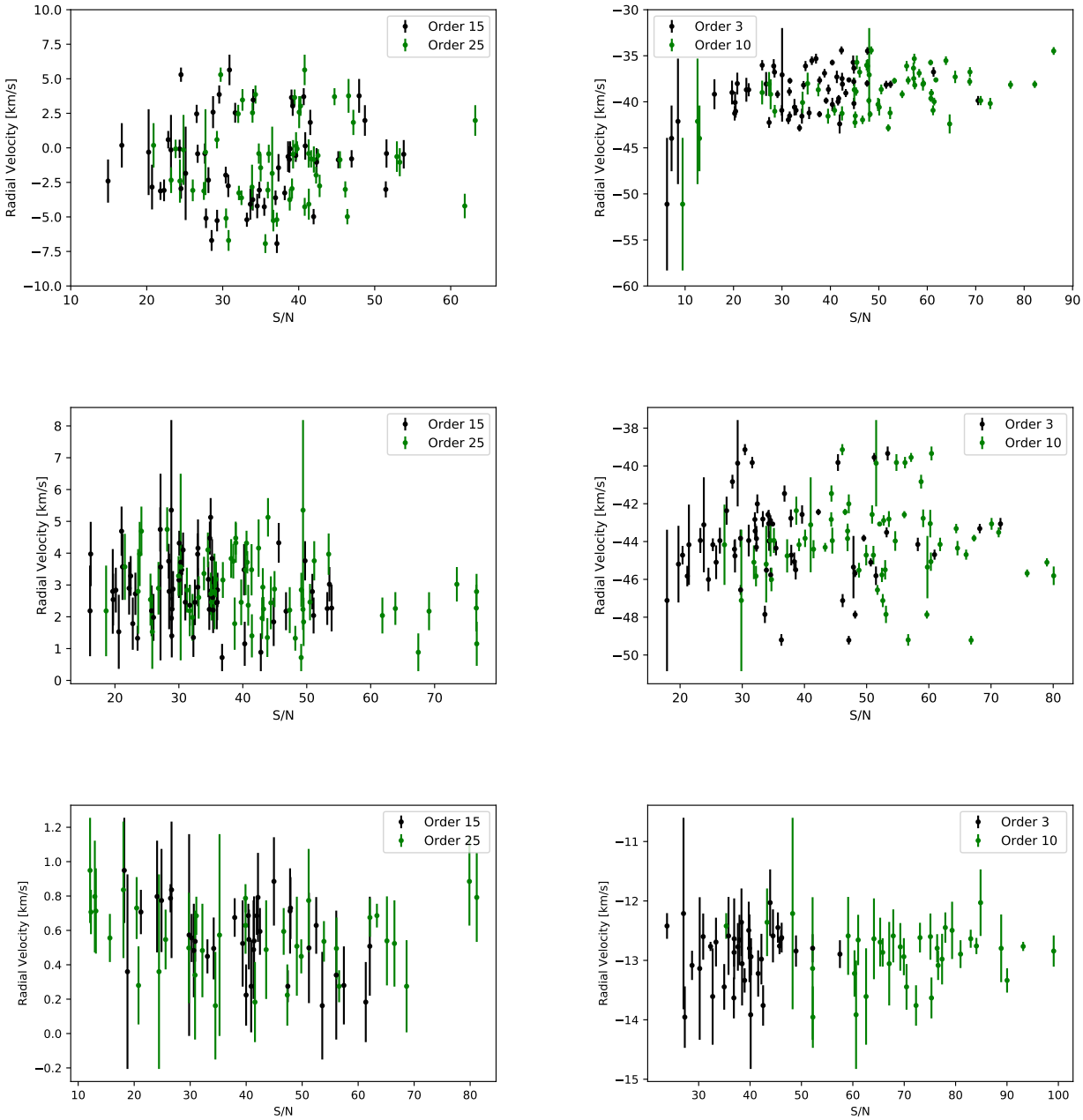

Figure 2.26: *Hen3-1333 (top panel), Hen2-113 (middle panel) and Hen2-47 (bottom panel) S/N measured from the order spectra produced by the* MIDAS *pipeline vs cross-correlation velocities. Left panel, has the velocities from the 4200 – 5400* Å *range and the velocities from the 5500 – 6200* Å *range are on the right panel.*

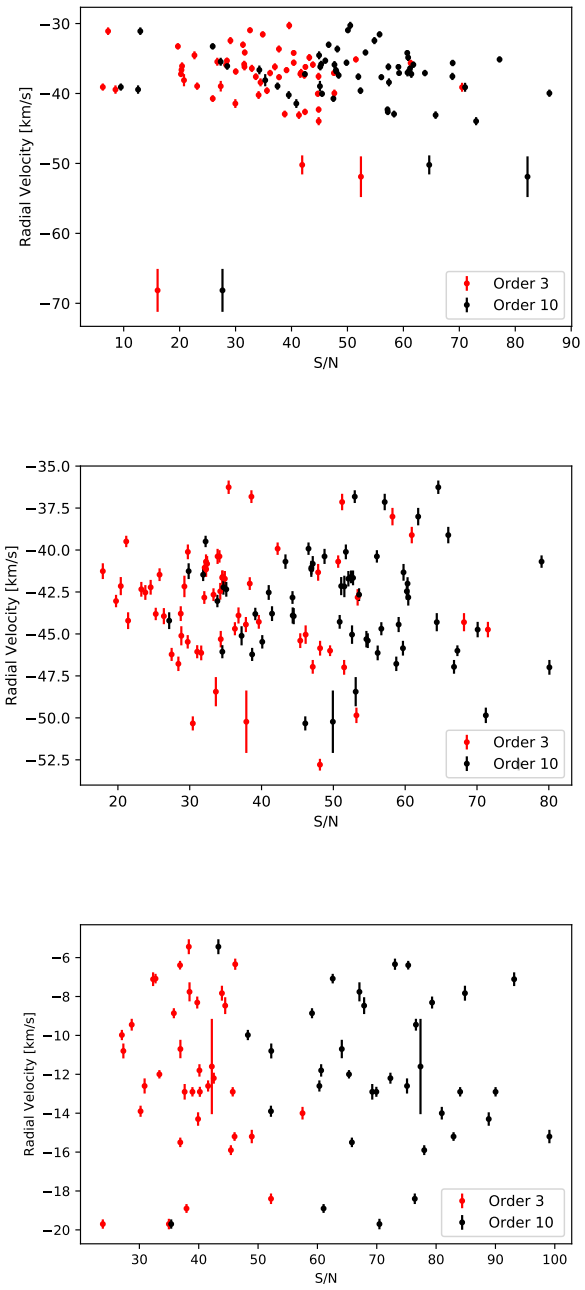

Figure 2.27: *Hen3-1333 (top), Hen2-113 (middle) and Hen2-47 (bottom) red order spectra S/N based on the individual orders produced by the* MIDAS *pipeline, plotted against the CIII 5695* Å*velocities.*

Chapter 3

Time-Series Analysis

Time-series analysis allows the investigation into a series of data and to look for periodicities. In this chapter the RVs and TESS lightcurves of Hen3-1333, Hen2-113 and Hen2-47 are analysed.

3.1 RV curves and TESS lightcurves

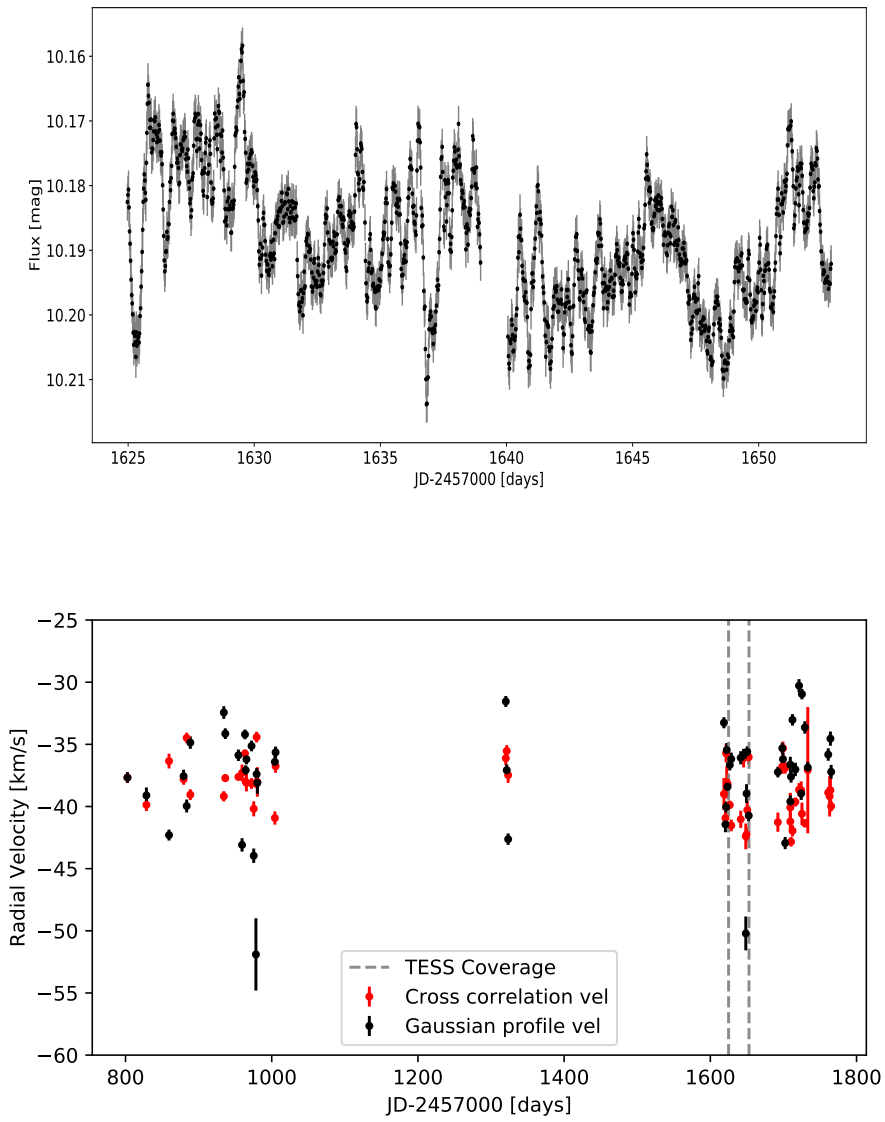

Figure 3.1: *Hen3-1333 lightcurve from TESS observed in sector 12 (Top panel), SALT HRS RV curves from the Gaussian profile fitting of CIII (5695 Å) in black and the cross-correlation velocities in red (Bottom panel).*

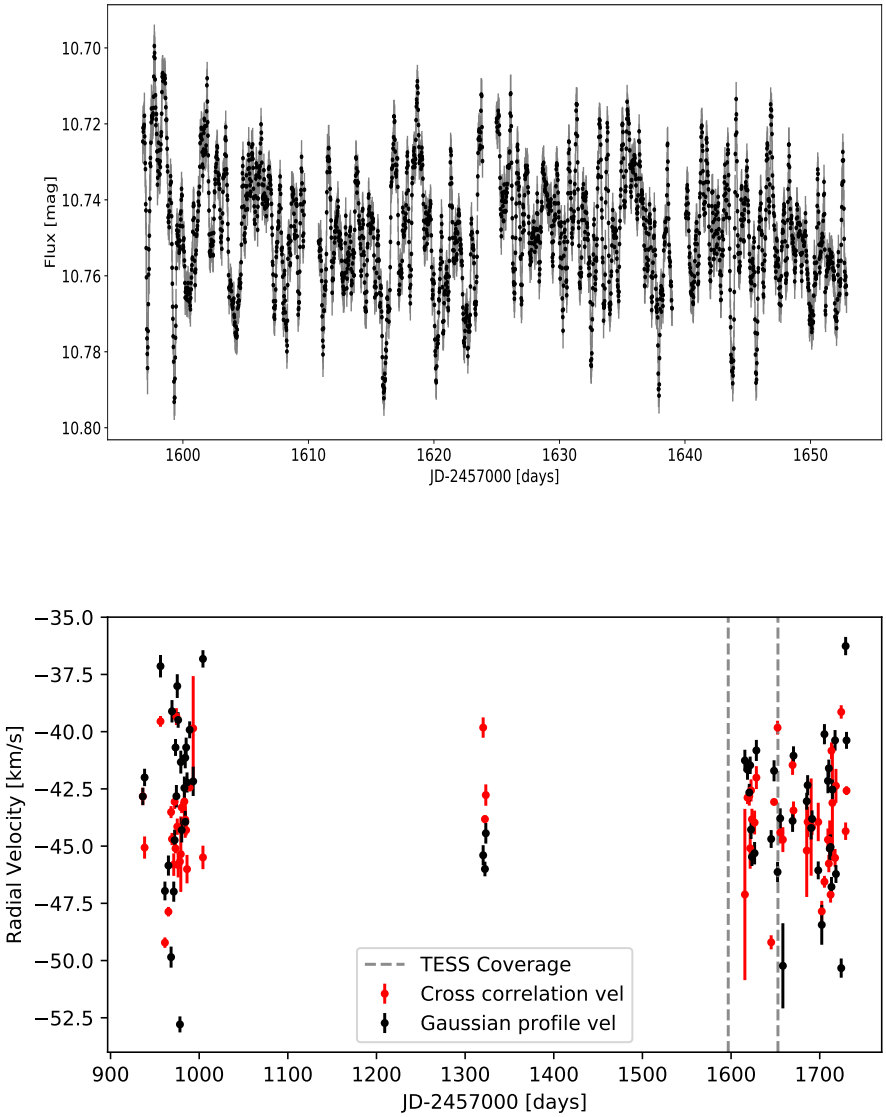

Figure 3.2: *Hen2-113 lightcurve from TESS observed in sector 11 and 12 (Top panel), SALT HRS RV curves from the Gaussian profile fitting of CIII (5695 Å) in black and the cross-correlation velocities in red (Bottom panel).*

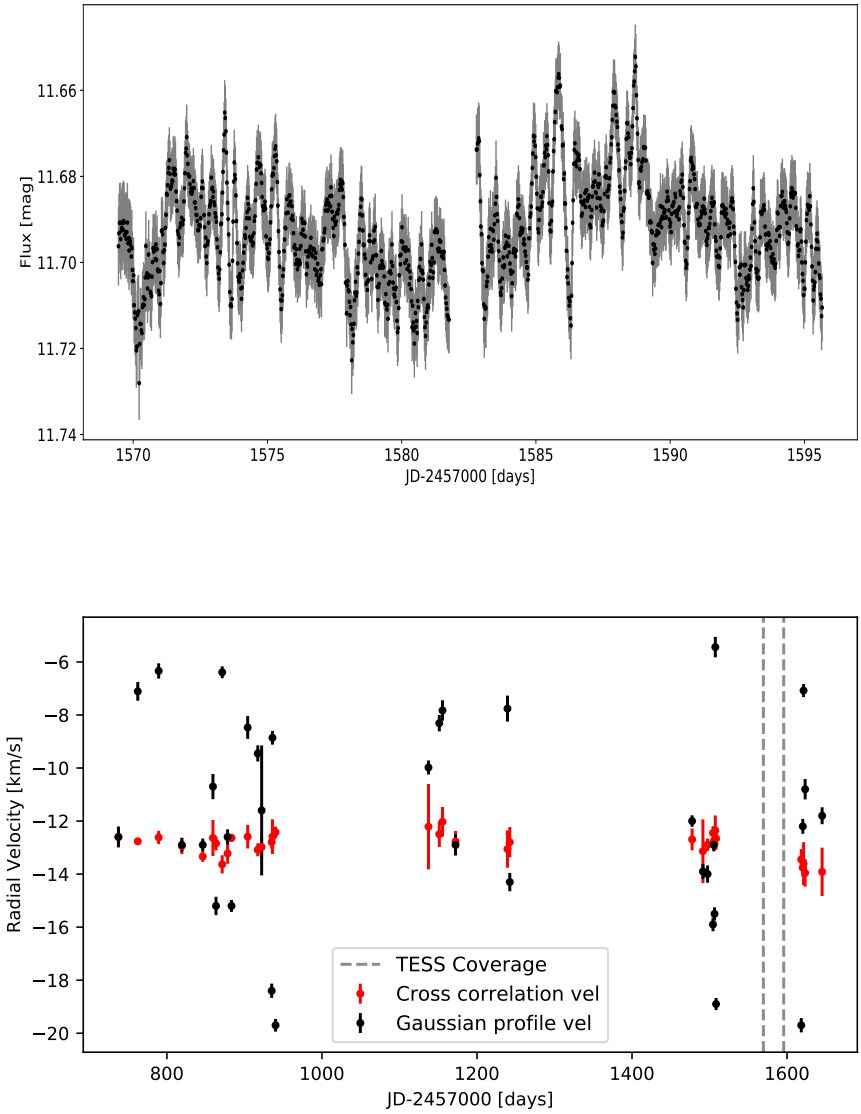

Figure 3.3: *Hen2-47 lightcurve from TESS observed in sector 10 (Top panel), SALT HRS RV curves from the Gaussian profile fitting of CIII (5695 Å) in black and the cross-correlation velocities in red (Bottom panel).*

Fig. 3.1, 3.2, 3.3 above display the time-series data for Hen3-1333, Hen2-113 and Hen2-47, respectively, where the TESS lightcurves are in the top panel and the RV time-series are in the bottom panel. Hen3-1333 and Hen2-113 show very similar RV curves, which is expected since they have similar class [WC] CSs. The TESS coverage is indicated on the RV curves to indicate the time frame in which the observations overlap. The RV curve from the cross-correlation velocities for Hen2-47 has a smaller amplitude range than the RV curve from the Gaussian profiles fitting, illustrating that there is more variability from the CIII line. The

flatter curve might be representing the nebula as opposed to the CS which has fast winds. To analyse the time-series we chose to use the Lomb-Scargle periodogram (VanderPlas 2018) and determine period candidates based on the variability.

3.2 Lomb-Scargle periodogram

The Lomb-Scargle periodogram was developed by Lomb (1976) and Scargle (1982). This tool is used to detect periodicities in unevenly-sampled time-series data. The method is based mainly on Fourier methods such as the Fourier transform. The origin of the Lomb-Scargle periodogram is the classical or Schuster periodogram (Schuster 1898) that takes the form,

$$P(f) = \frac{1}{N}\Big[\Big(\sum_n g_n cos(2\pi f t_n)\Big)^2 + \Big(\sum_n g_n sin(2\pi f t_n)\Big)^2\Big], \tag{3.1}$$

where $P(f)$ is the power spectrum, g_n is a uniformly sampled Gaussian function measured at time t_n.

This form of the periodogram has difficult statistical properties for non-uniform cases. When the classical periodogram is applied to data that has uniformly-sampled Gaussian noise, the products of the periodogram is distributed in terms of the χ-square result (VanderPlas 2018). This property is useful for cases where the periodogram is determined in the context of a classical hypothesis test to discern between periodic and non-periodic objects. Scargle (1982) solved the problem of non-uniform sampled data by considering a generalized form of the periodogram,

$$\begin{aligned} P_{LS}(f) = \frac{1}{2}\Big(&\Big(\sum_n g_n cos(2\pi f[t_n - \tau])\Big)^2 / \sum_n cos^2(2\pi f[t_n - \tau]) + \\ &\Big(\sum_n g_n sin(2\pi f[t_n - \tau])\Big)^2 / \sum_n sin^2(2\pi f[t_n - \tau])\Big), \end{aligned} \tag{3.2}$$

where τ is an arbitrary function and the divisors in the first and second term were chosen to ensure that the periodogram reduces to the classical form for even observations, secondly the periodogram's statistics are computable, and that the periodogram is insensitive to time-shifts in the data.

I used the Lomb-Scargle module in the ASTROPY package in Python to determine the periodograms. I specified the input data and frequency ranges to calculate the periodogram. The following section displays the periodogram results in Fig. 3.4 – 3.6 and the period candidates are stated in Tab. 3.1.

3.3 Periodogram results

The following periodograms were calculated for frequency ranges, $(0 - 1\ d^{-1})$, $(0 - 2\ d^{-1})$, $(0 - 3\ d^{-1})$, $(0 - 5\ d^{-1})$, $(0 - 10\ d^{-1})$ and $(1 - 10\ d^{-1})$, to account for periodicities of hours, days, months and years. The red spectra that accounts for cross-correlation and CIII RVs had an average S/N of 50.84, 51.69 and 70.35 for Hen3-1333, Hen2-113 and Hen2-47, respectively. The significance levels $(2 - 5\ \sigma)$ are the red lines in the figures and these were calculated by running 10 000 sets of periodograms for each data set (lightcurve, cross-correlation, CIII line), sorting the powers and indexing the values corresponding to positions of each σ. These were [9999], [9998], [9972] and [9544] for 2σ, 3σ, 4σ and 5σ, respectively. These significance levels accounted for the quality criterion of the signals from the periodograms. The left column of Fig. 3.4 shows the periodograms based on the TESS data for Hen3-1333, here there is a signal that stand out. The signal is suspected to be a result of systematic noise from the calculation of the Lomb-Scargle periodogram since the periodogram seems to jump and not start at zero power.

The top panel of Fig. 3.5 has a consistent signal in the $0 - 1\ d^{-1}$, this results in a periodicity of 4.18 days, 1.95 days and 1.46 days for TESS, cross-correlation and CIII line, respectively. The TESS signal is not significant, the other two are above 5σ but the CIII one appears to be a sampling alias of the signal at 0.73 days. The rest of the signal for Hen2-113 based on the RV curves have multiple signals above the significance levels but these appear to be aliases from the unevenly sampled data and are therefore disregarded.

Hen2-47 has a signal from the TESS data that reaches within 3σ, this is at 14.54 days, none of the cross-correlation signals are significant and the CIII line signals are largely above 5σ so they lie within the quality criterion but this makes it impossible to tell which signals are real. Hence, for this object the 14.54 days periodicity is the only one that will be investigated to confirm variability in this object.

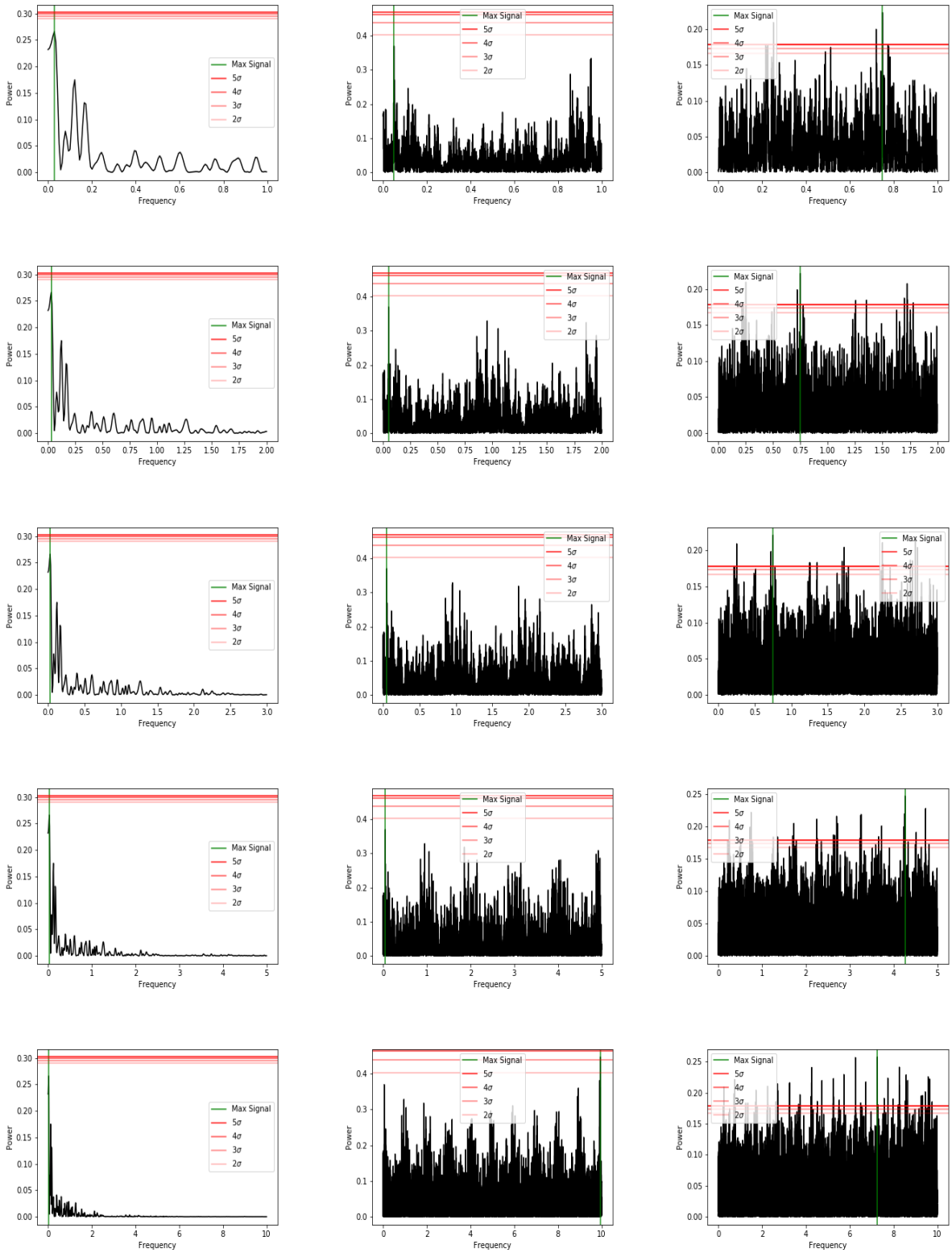

Figure 3.4: *Hen3-1333 periodograms of the TESS lightcurves and the RVs. TESS periodograms (left column), the cross-correlation RVs (middle column) and CIII (5695 Å) RVs in the right column where top to bottom range from (0 – 1 d^{-1}) – (0 – 10 d^{-1}).*

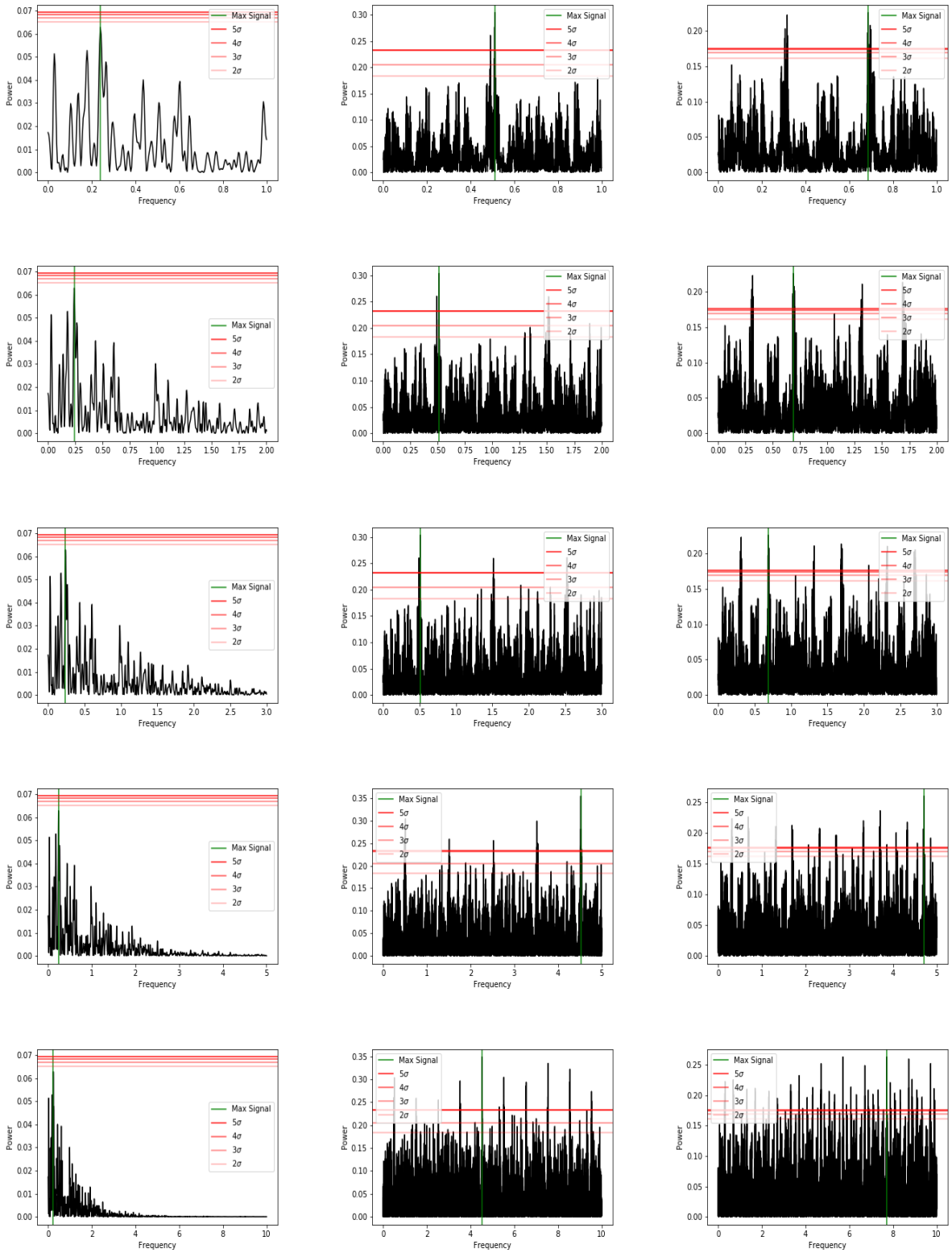

Figure 3.5: *Hen2-113 periodograms based on the TESS lightcurves and the RVs. TESS periodograms (left column), the cross-correlation RVs (middle column) and CIII (5695 Å) RVs in the right column where top to bottom range from (0 – 1 d^{-1}) – (0 – 10 d^{-1}).*

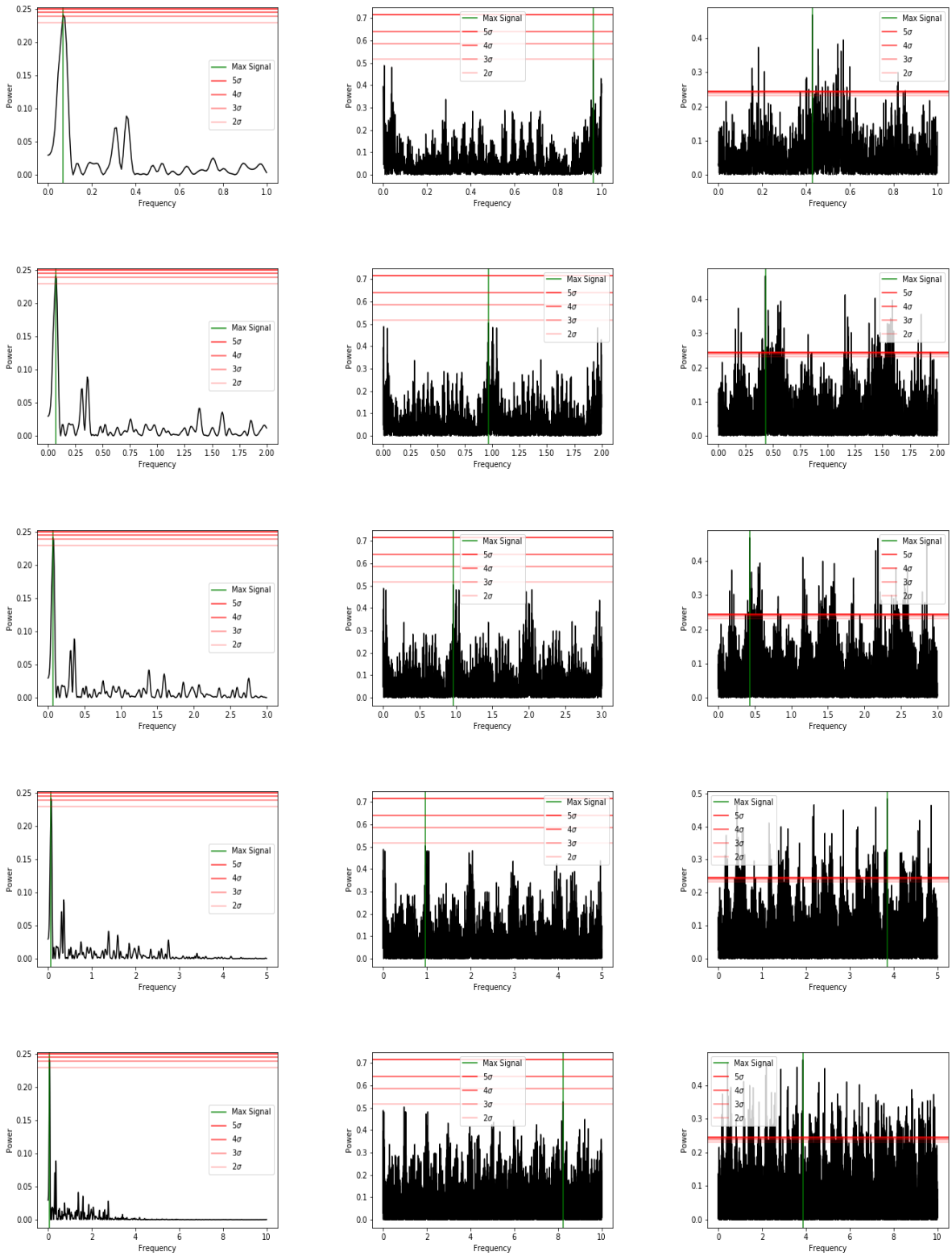

Figure 3.6: *Hen2-47 periodograms based on the TESS lightcurves and the RVs. TESS periodograms (left column), the cross-correlation RVs (middle column) and CIII (5695 Å) RVs in the right column where top to bottom range from (0 – 1 d^{-1}) – (0 – 10 d^{-1}).*

Table 3.1: *The period candidates from the periodograms seen in Fig. 3.4 – 3.6 in days in the order of increasing frequency ranges.*

	TESS		cross-correlation		CIII (5695 Å)	
Object	Period (days)	signal (days) uncertainty	Period (days)	signal (days) uncertainty	Period (days)	signal (days) uncertainty
Hen3-1333	34.75	11.43	19.93	0.28	1.3330	0.0014
			0.10	1.52	0.370236	0.000044
					0.12922	0.00011
Hen2-113	4.18	0.35	1.954	0.003	1.4558	0.0015
			0.221110	0.000037	0.249326	0.000036
					0.114672	0.000011
Hen2-47	14.54	10.0	1.03890	0.00054	2.3305	0.0054
			0.121500	0.000016	0.259300	0.000067
					2.916488	0.000067

The periodicities in Tab. 3.1 were selected because they stood out as the highest signal for each frequency range and the uncertainty was estimated as the fwhm from the signal. There were signals that were the same for certain frequency ranges (e.g. first and second row, for $1 - 3\ d^{-1}$) but not all the signals were significant. Hen2-47 is the only object that appears to have a significant signal (3σ) for the TESS data and all the objects had multiple significant signals for the RV time-series. The periodicities in the table suggest that there is some variability in the objects but due to the aliasing the significance of the results cannot be trusted to represent legitimate orbital periods of binary systems. The time-series needs to be phased up with these periodicities to further investigate the variability of the objects.

3.4 Phased RV curves and lightcurves

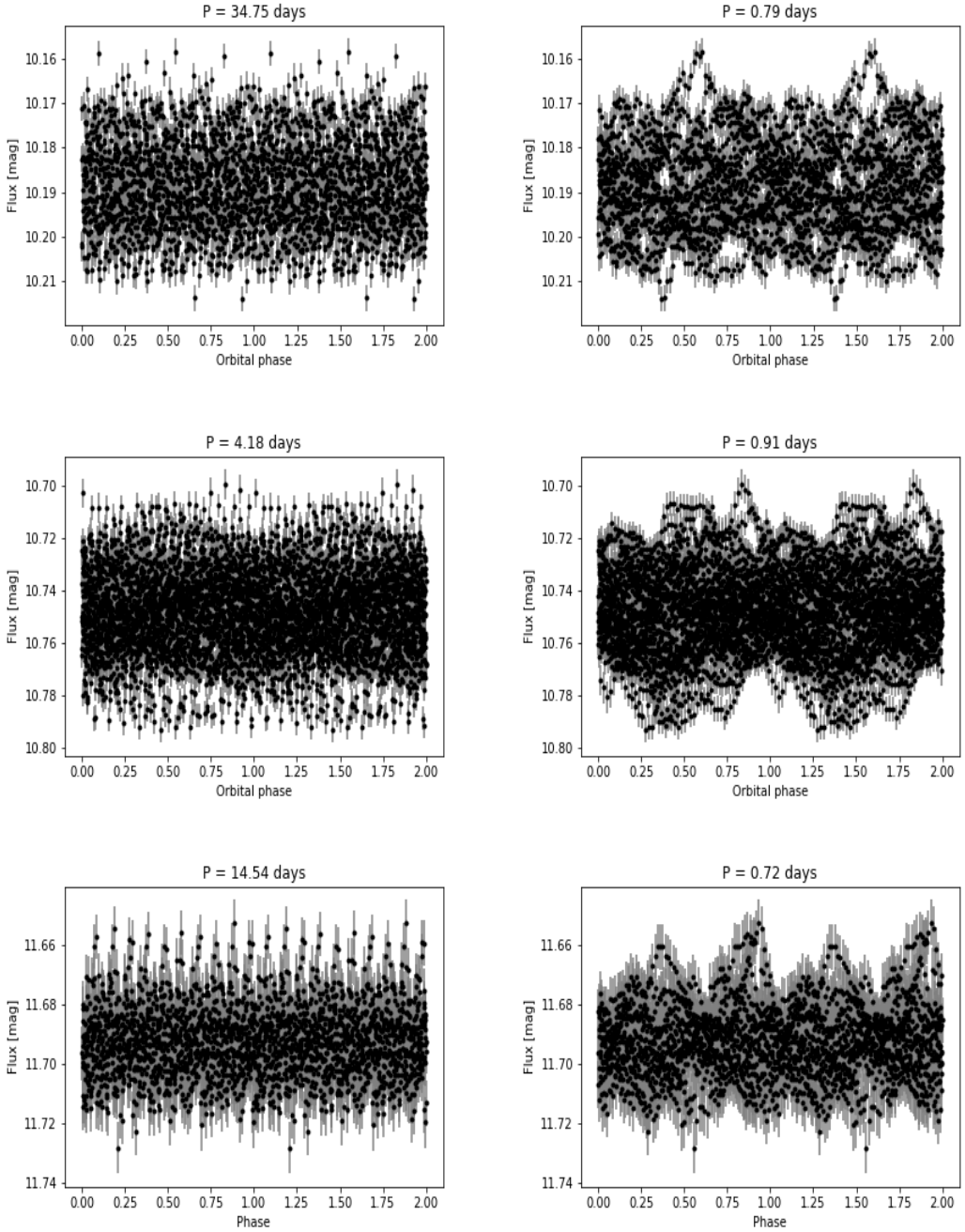

Figure 3.7: *The phased lightcurves of Hen3-1333 (top row), Hen2-113 (middle row) and Hen2-47 (bottom row) where the left panel represents the period from frequency range 0 - 10 (Hen3-1333 (34.75 days), Hen2-113 (4.18 days), Hen2-47 (14.54 days)) and the right panel represents the frequency range 1 - 10 (Hen3-1333 (0.79 days), Hen2-113 (0.91 days), Hen2-47 (0.72 days)).*

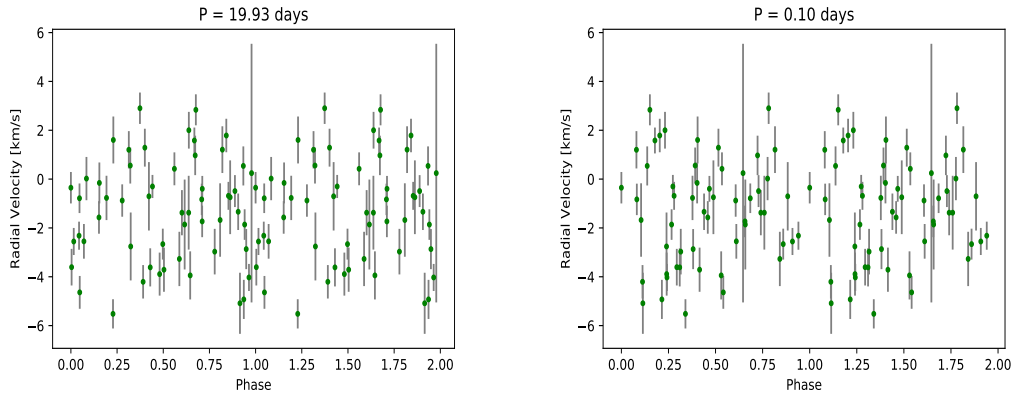

Figure 3.8: *The phased cross-correlation RV curves of Hen3-1333. The plot based on the frequency range 0 - 5 produces a period of 19.93 days (left panel), frequency range 0 - 10 give a period of 0.10 days (right panel).*

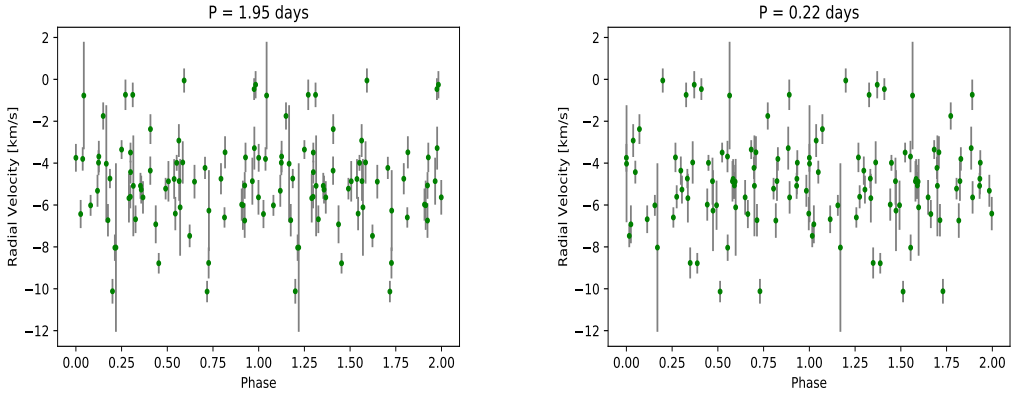

Figure 3.9: *The phased cross-correlation RV curves of Hen2-113. The plot based on the frequency range 0 - 3 give a period of 1.95 days (left panel) and frequency range 0 - 10 give a period of 0.22 days (right panel).*

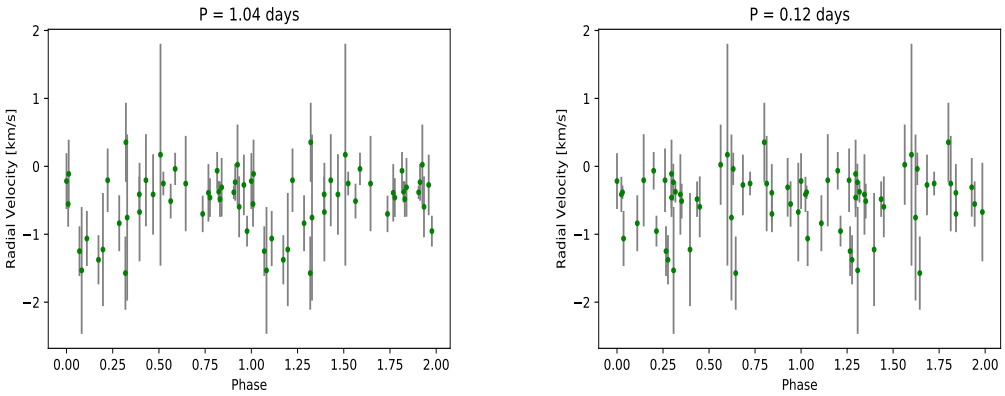

Figure 3.10: *The phased cross-correlation RV curves of Hen2-47. The plot based on the frequency range 0 - 5 give a period of 1.04 days (left panel) and frequency range 0 - 10 give a period of 0.12 days (right panel).*

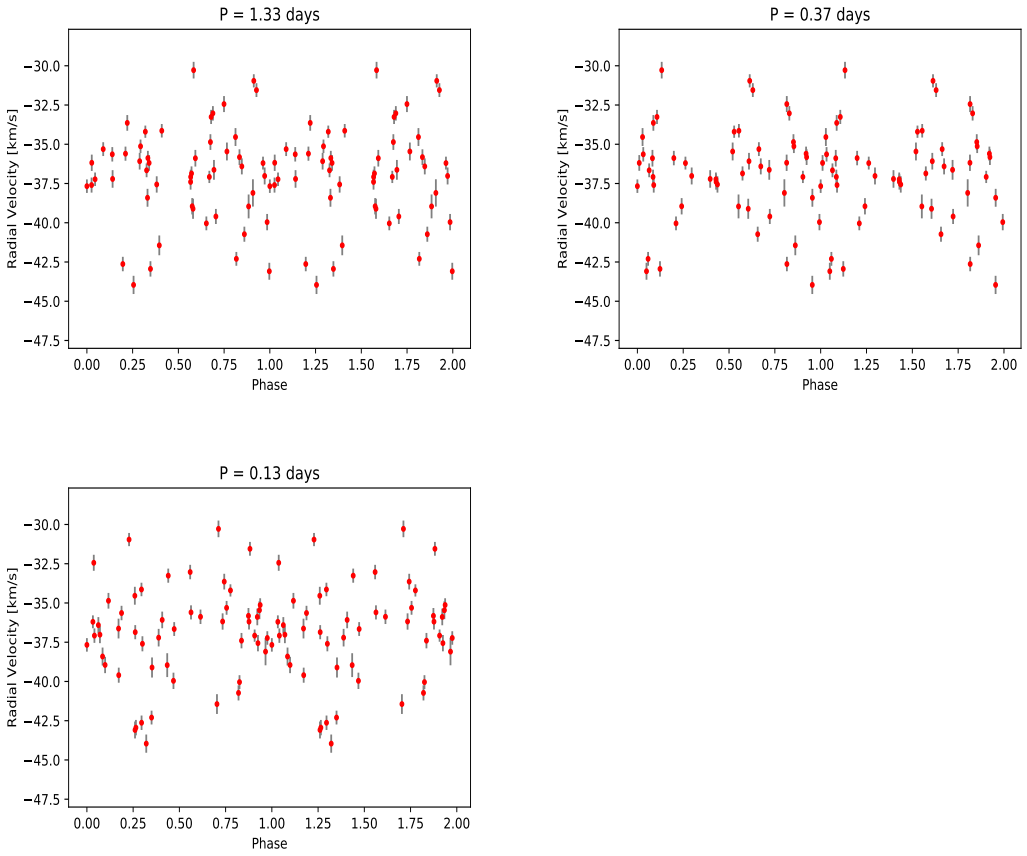

Figure 3.11: *The phased CIII RV curves of Hen3-1333. The plot based on the frequency range 0 - 2 give a period of 2.04 days (top left panel), frequency 0 - 5 give a period of 0.37 days (top right panel), and frequency range 0 - 10 give 0.13 days (bottom panel).*

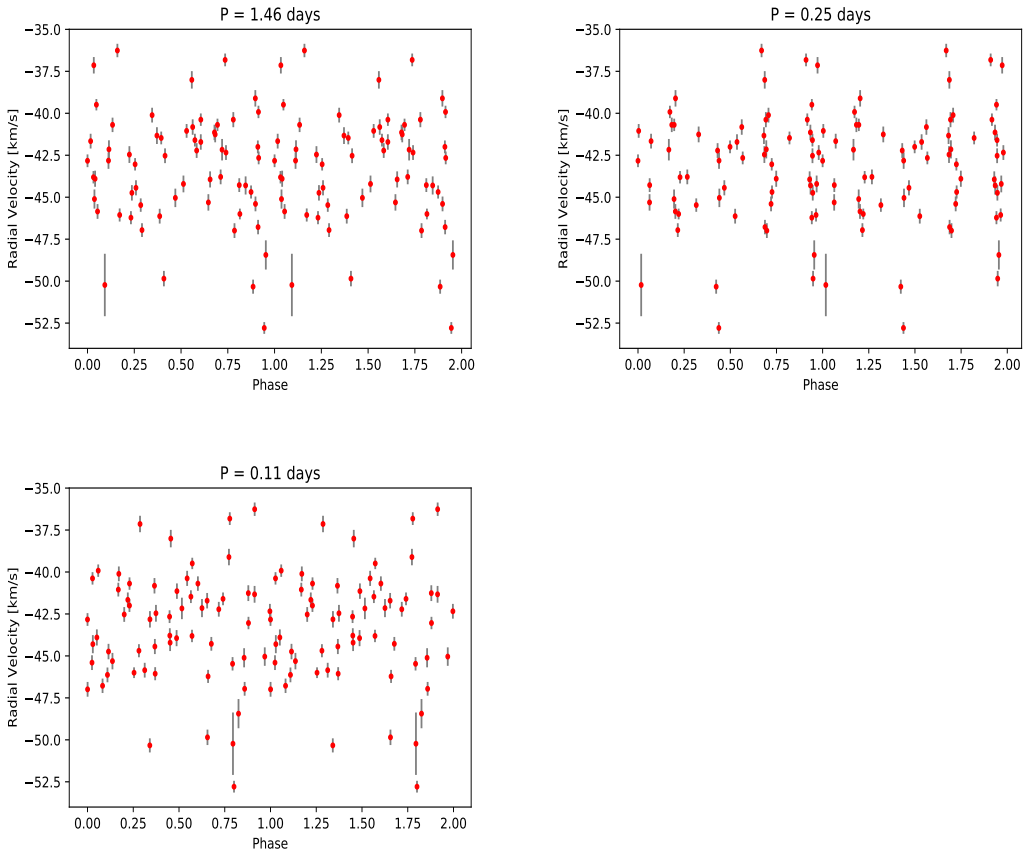

Figure 3.12: *The phased CIII RV curves of Hen2-113. The plot based on frequency range 0 - 3 gives a period of 1.46 days (top left panel), frequency 0 - 5 give a period of 0.25 days (top right panel), frequency ranges 0 - 10 give 0.11 days (bottom panel).*

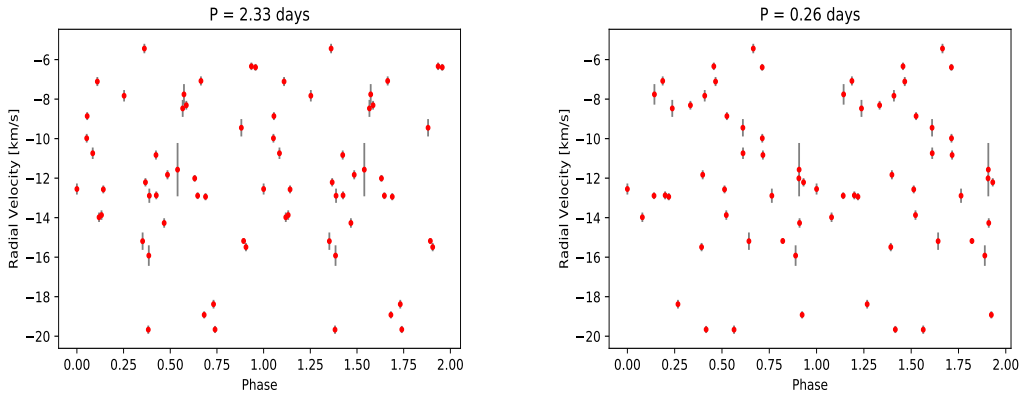

Figure 3.13: *The phased CIII RV curves of Hen2-47. The plot based on frequency range 0 - 3 give a period of 2.33 days (left panel), frequency 0 - 5 give a period of 0.26 days (right panel).*

The time-series results were phased on the periodicities expressed in Tab. 3.1 from the periodograms and are displayed in Fig. 3.7 – 3.13 shown separately for each object and source of method (TESS, cross-correlation, CIII line). The figures do not show coherent phased diagrams for the periodicities but Fig. 3.10, left panel shows an interesting curve for Hen2-47, a true orbital period would phase the time-series into a sinusoidal wave and this appears to resemble that. This signal however did not fall within the significance levels.

Hen2-47 has a quality signal at 14.54 days and the time-series data of the object were phased on this period (Fig. 3.14). These phased diagrams are incoherent and suggest this periodicity is likely a result of the wind variability from the CS and not due to a binary system.

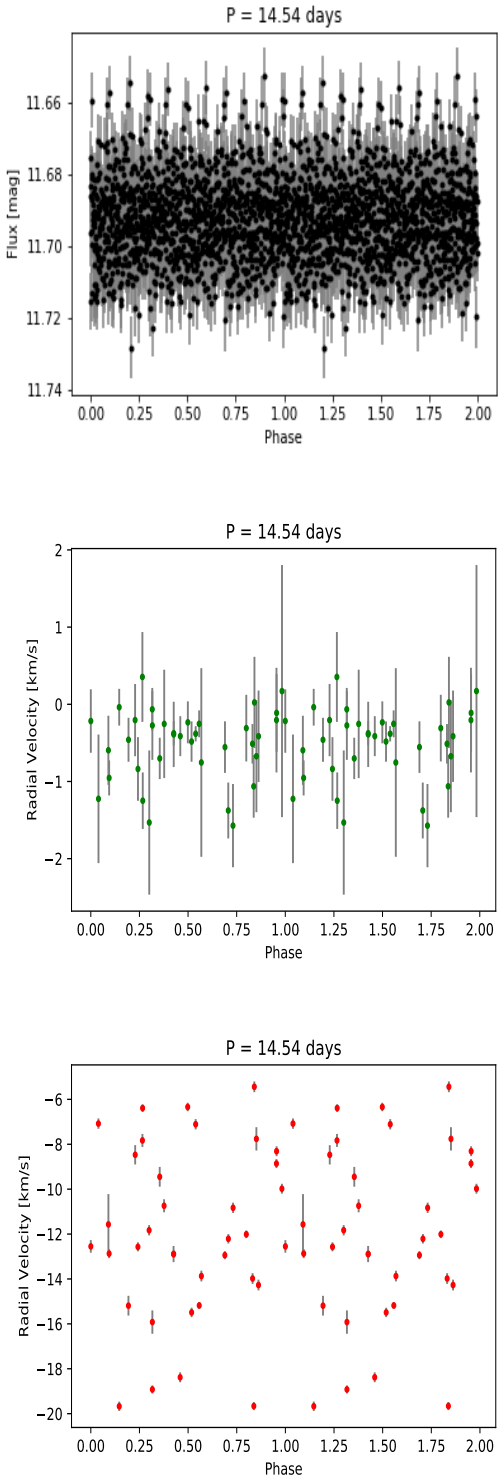

Figure 3.14: *The phased time-series of Hen2-47, phased on a period 14.54 days for the TESS (top), cross-correlation (middle) and CIII line time-series (bottom).*

Chapter 4

Discussion

In this chapter we assess scenarios for compatibility with the observed photometry and RV time-series.

4.1 Proposed scenarios

4.1.1 Scenario 1 - Close period binary (1 – 10 days)

Close binary interactions are regarded as viable mechanisms for modelling aspherical PNe (Jones and Boffin 2017). A close binary system in PNe is considered to be a system that has an orbital period of <3 days (De Marco et al. 2008) and these systems make up a fraction of $\approx 20\%$ of PNe CSs (Bond 2000, Miszalski et al. 2009). In this work the orbital period range 1 – 10 days is considered as short (i.e. a close binary). The periodograms include significance levels ($2 - 5\sigma$) to measure the quality of the data and the results from periodograms show that this is met. Tab. 3.1 illustrates that there is some short term variability found but these periodicities do not phase up coherently (Fig. 3.7 – 3.13). This outcome could be largely due to the uneven observational sampling of the data but it is more likely due to the wind variability which is seen from the pulsations in the lightcurves (Fig. 2.18, 2.20, 2.22). Based on the high cadence, the sensitivity, the time frame of the time-series and the incoherent phased diagrams, close binaries (<10 days) can be ruled out for the objects.

4.1.2 Scenario 2 - Intermediate period binary (10 – 10^3 days)

The periodicities from the periodograms based on the TESS lightcurves are not varying with the extended frequency ranges (left column of Fig. 3.4 – 3.6) but there is rather only one strong signal for each plot. The TESS signal from Hen2-47 is the only one that reaches the significance levels, within 3σ, alluding to a periodicity of ≈ 14.54 d and Fig. 3.14 shows the phased time-series of Hen2-47 based on this period. The 14.54 d periodicity does not produce coherent phased diagrams and it is also worth noting that this period is likely an

alias since it is about half of the length of the observing period (27.4 d). The signals from the periodograms representing the TESS lightcurves for Hen3-1333 and Hen2-113 do not even reach the 2σ level. This could mean the orbital periods are simply longer than what the current TESS observations can probe but this is unlikely since photometry is biased to detecting short periods. The periodograms representing the RV time-series of Hen3-1333 (Fig. 3.4 top middle panel) reveal a periodicity of 19.93 d but this does not fall within the significance criterion, thus intermediate orbital periods for this object are not likely based on the RV time-series. Hen2-113 does not show any intermediate periodicities from the periodograms and considering the time frame of the observations for the RV time-series is <800 days (Fig. 3.2 bottom panel), intermediate periodicites can be ruled out for this object. The same can be said for Hen3-1333 (time frame >900days, Fig. 3.1 bottom panel) but not Hen2-47 (Fig. 3.3 bottom panel) since although it was observed over a similar time frame, it only has 35 spectra. Thus we cannot rule out intermediate orbital periods for Hen2-47.

4.1.3 Scenario 3 - Long period binary (10^3 – 10^4 days)

Long orbital period binary systems in PNe are considered for systems that have orbital periods ranging from hundreds to thousands of days. Close and intermediate period binary systems may result from post-CE interaction systems, but the longer orbital period systems may be due to wind interactions. The number of long period systems is growing (Miszalski et al. 2018a) and the longest confirmed orbital period known is from a wide-binary CS BD+30°623 (NGC 1514) with a period of 3306 ± 60 days (Jones et al. 2017).

Velázquez et al. (2012) models PNe with multipolar features resembling Hen2-47 and suggests that such systems are likely to have long orbital periods, of the order of several years. The proposal of an orbital period of several years for multipolar PNe (which all three objects satisfy) suggest that these systems are likely long period systems. To confirm this, the objects require continued RV monitoring and more evenly sampled data for the spectroscopic time-series. In the time frame we have observed these objects, we find no indication for long term RV variability (bottom of Fig. 3.1 – 3.3). Fig. 3 in Jones et al. (2017) highlights that Méndez et al. (2016) observed a long time frame for NGC 1514 when the object did not show any long-term variability, but this object does have a confirmed binary CS as discussed above. It might be that our objects were also observed during an unlucky orbital phase, but this requires more RV monitoring to confirm.

Comparing the scenarios above to what is discussed in 1.4.3 from De Marco and Soker (2002), where they proposed two scenarios for a majority (80 – 85 %) and minority (15 – 20 %) of [WC] CS exhibiting dual-dust chemistry, some predictions are compatible. The scenarios both agree that the companions are not close, which is consistent with our results where short period systems are ruled out. The compatibility between our results and the literature implicates Hen3-1333 and Hen2-113 since these have [WC] CSs and dual-dust chemistry. Monitoring with other facilities such as NEOWISE to probe for variability due to dust can help with understanding exactly how compatible these objects are with the De Marco and Soker (2002) scenarios. The main scenario for a majority of [WC] CSs, suggests that the companion star is low mass (brown dwarf) whereas the other suggests a larger mass companion (De Marco and Soker 2002).

In Sec. 4.2 the modelling of the possible companion type and class is discussed for the objects in this work, taking into account assumed orbital periods from each scenario.

4.2 Mass function

The mass function for binary stellar objects is expressed as follows

$$\frac{m_2^3}{(m_1+m_2)^2} sin^3 i = \frac{P}{2\pi G} v_{1,r}^3, \tag{4.1}$$

where m_1 is the primary component mass, m_2 is the secondary component mass, i is the orbital inclination, G the gravitational constant and $v_{1,r}$ the semi-amplitude. The mass of the primary component was assumed, the inclinations for Hen3-1333 and Hen2-113 and the inclination for Hen2-47 was taken from Velázquez et al. (2012) (Tab. 4.1). Eqn. 4.1 was used to estimate the companion masses for the objects mentioned above by modelling Eqn. 4.1.

Table 4.1: *The initial conditions assumed for the mass function and calculated semi-amplitudes from the CIII RV time-series.*

	Primary mass	inclination	Semi-amplitude
Hen3-1333	$0.4M_\odot$, $0.6M_\odot$	$+10°$ to $+40°$	5.68 km/s
Hen2-113	$0.4M_\odot$, $0.6M_\odot$	$+10°$ to $+60°$	3.32 km/s
Hen2-47	$0.4M_\odot$, $0.6M_\odot$	$+10°$ to $+30°$	3.88 km/s

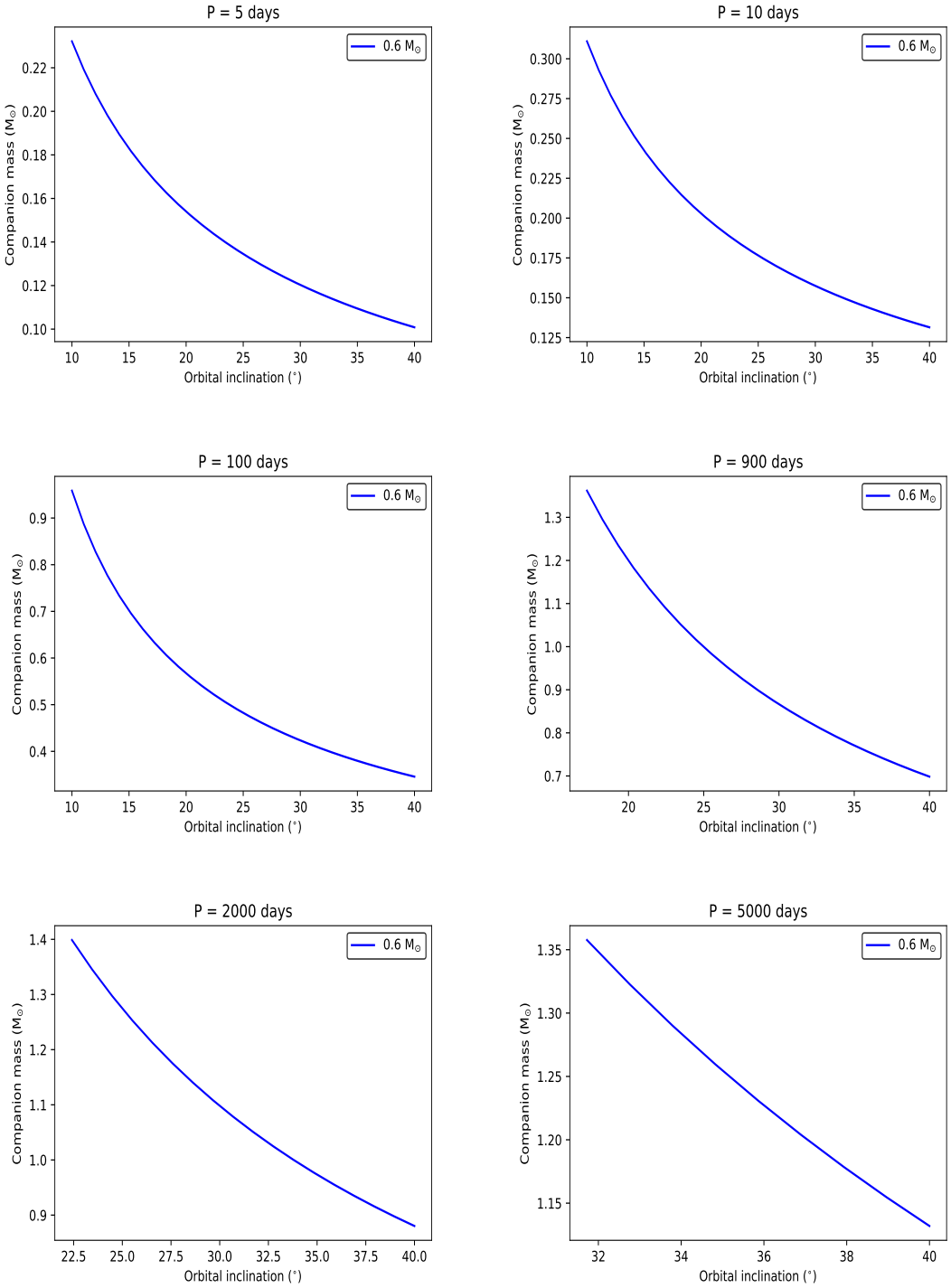

Figure 4.1: *Hen3-1333 companion mass vs inclination plot based on a primary mass of $0.6M_{\odot}$ for orbital periods in the short (top panel), intermediate (middle panel) and long (bottom panel) scenario ranges.*

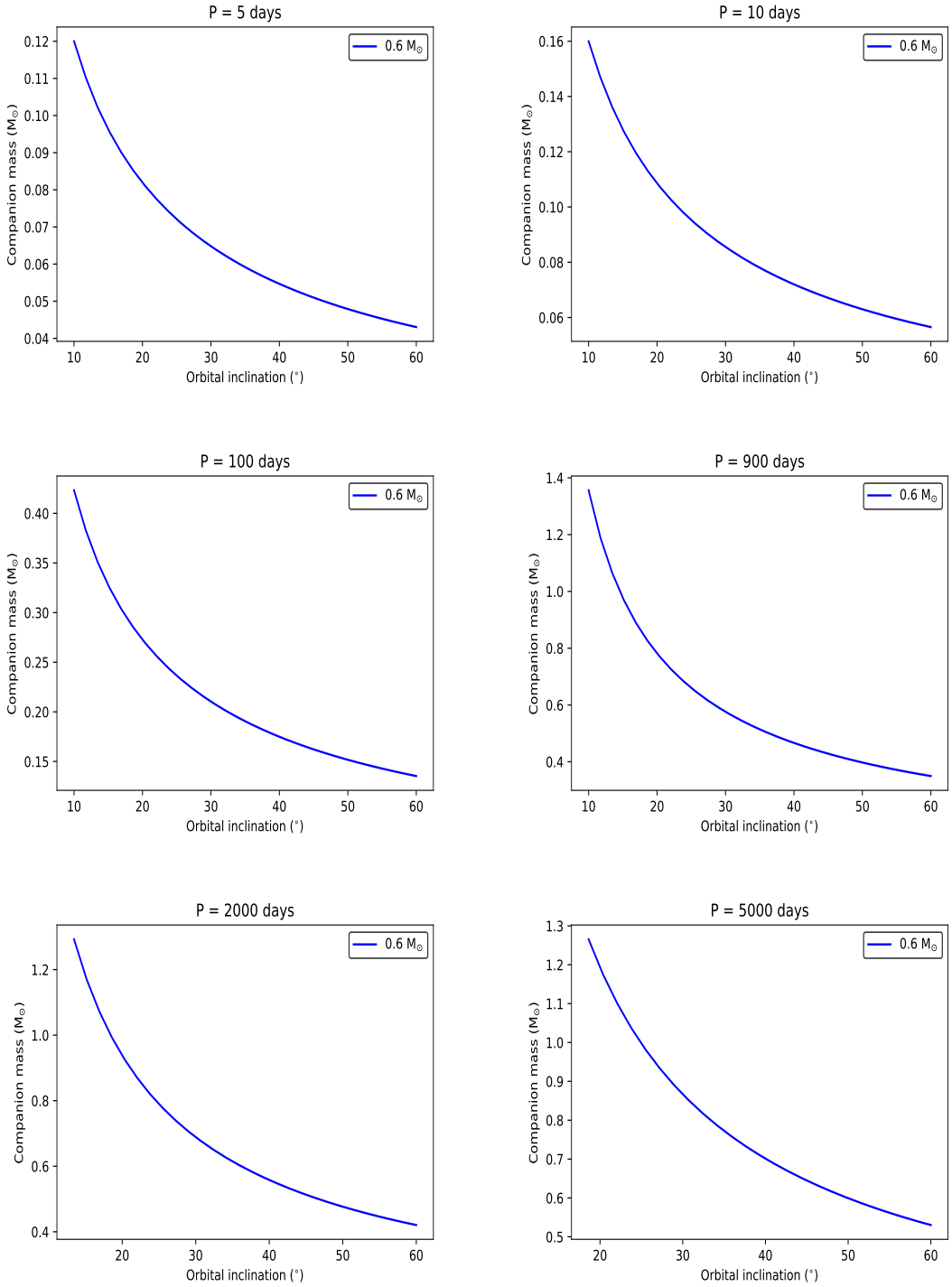

Figure 4.2: *Hen2-113 companion mass vs inclination plot based on a primary mass of $0.6M_{\odot}$ for orbital periods in the short (top panel), intermediate (middle panel) and long (bottom panel) scenario ranges.*

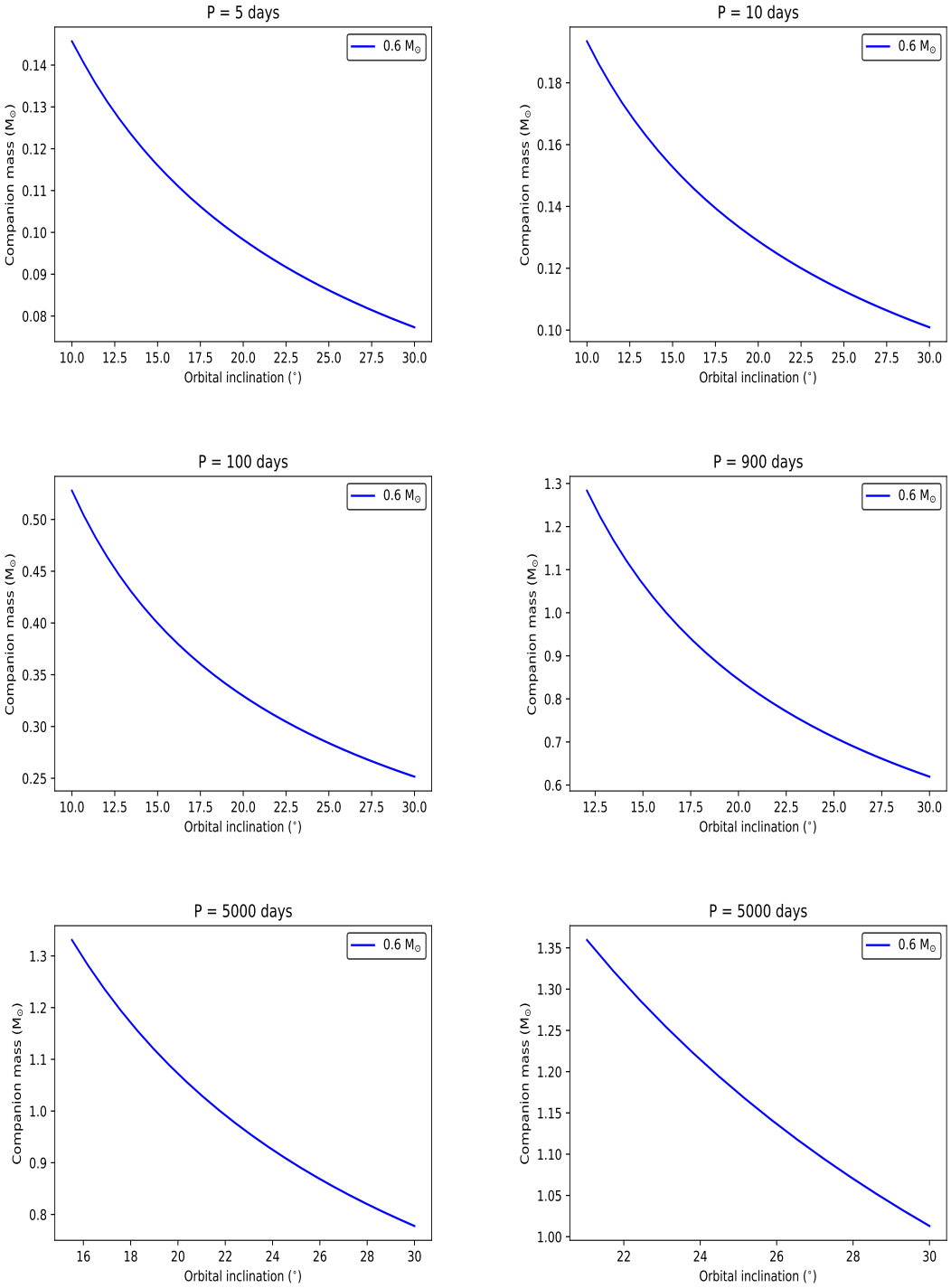

Figure 4.3: *Hen2-47 companion mass vs inclination plot based on a primary mass of $0.6M_{\odot}$ for orbital periods in the short(top panel), intermediate (middle panel) and long (bottom panel) scenario ranges.*

Rearranging Eqn. 4.1 in terms of the semi-amplitude, it takes the form

$$v_{1,r}^3 = \frac{2\pi G m_2^3}{(m_1 + m_2)^2} \frac{sin^3 i}{P}. \tag{4.2}$$

The companion masses were modelled for the objects and the assumed parameters for the orbital periods were based on the scenarios discussed in Sec. 4.1. The orbital period ranged between 1 and 5000 days (Tab. 4.2 – 4.4). The semi-amplitudes from the CIII RV time-series results are 5.68 km/s, 3.32 km/s and 3.88 km/s for Hen3-1333, Hen2-113 and Hen2-47, respectively (Tab. 4.1). Although we do not find any clear periodicities, we can estimate the companion properties based on an upper limit to the semi-amplitude. We assume this as 1-σ variation of the RV measurements. The results in Fig. 4.1, 4.2, 4.3 follow a trend where the longer orbital periods have larger companion masses (Tab. 4.2 – 4.4). The longer orbital periods from scenario 3 resulted in inconclusive companion masses at the low inclinations, this can be seen in the bottom panels of Fig. 4.1 – 4.3 where the inclinations start at higher points.

Table 4.2: *Primary masses with the modelled companion mass results for Hen3-1333.*

	Companion masses ($M_\odot$)
Orbital Period (days)	0.6$M_\odot$ Primary
5	0.10 – 0.23
10	0.13 – 0.31
100	0.35 – 0.96
900	0.70 – 1.36
2000	0.88 – 1.40
5000	1.13 – 1.36

Table 4.3: *Primary masses with the modelled companion mass results for Hen2-113.*

	Companion masses ($M_\odot$)
Orbital Period (days)	0.6$M_\odot$ Primary
5	0.043 – 0.12
10	0.057 – 0.16
100	0.14 – 0.42
900	0.35 – 1.36
2000	0.42 – 1.29
5000	0.53 – 1.27

Table 4.4: *Primary masses with the modelled companion mass results for Hen2-47.*

	Companion masses ($M_\odot$)
Orbital Period (days)	0.6$M_\odot$ Primary
5	0.077 – 0.15
10	0.10 – 0.19
100	0.25 – 0.53
900	0.62 – 1.28
2000	0.78 – 1.33
5000	1.01 – 1.36

Table 4.5: *The summary of characteristics and features of Hen3-1333, Hen2-113, Hen2-47.*

Object	Multi-polar	Dual-dust chemistry	Offset CS	Circum-stellar disk	Ring-like arcs	Period variability	Dust formation
Hen3-1333	Satisfy	Satisfy	None	Satisfy	None	N/ significant	Satisfy
Hen2-113	Satisfy	Satisfy	Satisfy	None	Satisfy	N/ significant	None
Hen2-47	Satisfy	None	Satisfy	None	Satisfy	Significant	None

4.3 Binary CSs for Hen3-1333, Hen2-113 and Hen2-47

Hen3-1333 ticks the multipolar, dual-dust chemistry and the circumstellar disk boxes (Tab. 4.5). There is evidence of pulsations and likely dust obscuration events in the lightcurve (Fig. 1.8, 3.1 top panel), which suggest there is dust formation occurring in the object. Hen2-113 is multipolar in morphology, there is dual-dust chemistry present and an offset CS is observed with two rings (Fig. 1.10). Hen2-47 also has an offset CS but it is accompanied with two ring-like arc structures around the centre of the object. Hen2-47 is also multipolar in morphology (Tab. 4.5). Sec. 1.4 we discussed how binary CSs are the favourable scenario to produce these features, but and we attempted to reassure the literature.

De Marco and Soker 2002, Velázquez et al. 2012 suggested long orbital periods are possible in objects that have [WC] type CSs and are multipolar. Hen3-1333 and Hen2-113 have [WC] CSs and all three objects are multipolar. Our results are consistent with longer periods (scenario 3), and the literature. In the effort to find a possible binary companion that agrees with these results, the mass function (Eqn. 4.1) was modelled. The companion mass possibilities are 0.10 – 1.36 $M_{\odot}$ for Hen3-1333, 0.043 – 1.27 $M_{\odot}$ for Hen2-113 and 0.077 – 1.36 $M_{\odot}$ for Hen2-47 (Fig. 4.1, 4.2, 4.3). These masses are consistent for both De Marco and Soker (2002) scenarios, where the first one predicts low mass (brown dwarf) companions and the second one implies larger mass companions which considers a disk that Hen3-1333 satisfies with its dust-disk. The stars with the companion masses found in this work are similar to main sequence stars and dwarfs. Other possible companions are white dwarfs and in the case of Hen3-1333 and Hen2-113, which have low-ionisation nebulae, these stars would have to be very cool and/or low mass.

Chapter 5

Conclusion

The aim of this project was to develop a quantitative time-series analysis to determine whether these objects have binary CSs and develop constraints to permissible orbital parameters. This was achieved through analysis of SALT and TESS via the methods of cross correlation and individual Gaussian line fitting to determine RVs and constructing TESS lightcurves of these objects. The objects were chosen because they are strong candidates for binarity, they exhibit unique characteristics and features that are not well understood but argued to be present in PNe that have binary CSs.

Hen3-1333 is a young multipolar PNe and it has a WR CS, this object has a discovered edge-on disk (De Marco et al. 2002a) and the dual-dust chemistry observed in its spectra is consistent with the confirmed dust-disk. The lightcurve (Fig. 1.8, 3.1 1.8, 3.1) shows dust obscuration events and dust formation is assumed in this object because of the presence of this dust-disk. The second object, Hen2-113 has a similar CS to Hen3-1333 and this can be seen in their RV curves (Fig. 3.1, 3.2 3.1, 3.2) and their spectra (Fig. 2.4, 2.5 2.4, 2.5) since it also has observed dual-dust chemistry. Hen2-113 is multipolar and has an offset CS that might be the result of CE mass loss (Chamandy et al. 2019) but our results suggest an unlikely close binary, therefore possibly not a post-CE object. Hen2-47, similarly has an offset CS and it has two ring-like arcs around the CS and it has mulitpolar morphology. The data and results in this work have allowed us to constrain the orbital period parameters to long orbital periods for the Hen3-1333 and Hen2-113. These are periods $>10^3$ days based on the scenario 3 and for Hen2-47, intermediate to long periods are possible ($>$20 days) based on the second and third scenario. This is consistent with the variability from the periodogram results and is supported with the time frame of our SALT data and TESS data.

In Chapter 4 we discussed how our results agree with the literature predictions for objects similar to ours and they are compatible, with regards to predicting binarity and the orbital period of such systems. Long orbital period systems are predicted for the majority of [WC] CSs and multipolar morphological objects (De Marco and Soker 2002, Velázquez et al. 2012). Only Hen3-1333 and Hen2-113 have confirmed [WC] type CSs and Hen2-47 is a [WR] CS with unspecified sub-class, and all three objects are multipolar, so the literature applies to this work. The companions modelled for the objects are main sequence and dwarf stars with masses of 0.10 – 1.36 $M_{\odot}$ for Hen3-1333, 0.043 – 1.27 $M_{\odot}$ for Hen2-113 and 0.077 – 1.36 $M_{\odot}$ for Hen2-47, for period ranges supporting the three scenarios discussed in Sec. 4.1. Since scenario 3 is the favoured scenario the companion masses could possibly lie towards the upper limits of these ranges but the systems are open to any companion size.

Finally we suggest that the objects in our work have main sequence or dwarf companions stars. And that these systems likely have long orbital periods and low orbital inclinations. To confirm this, continued monitoring is required. Since the results do not conclusively suggest that these objects have binary CSs, it is worth considering a merger scenario that has resulted in the formation of a single star. This work however, does not have any observational constraints to explore this scenario. And in the case that these objects have long orbital periods, low mass companions and low inclination (or lower) as assumed here, it would be difficult to detect any with the current measuring capabilities.

5.1 Relevance of this study

It is important to grow the binary population for PNe, especially the objects that are not well understood. The PNe phase is the closest subsequent phase to the CE phase and will therefore provide important information to understanding the CE evolution. This work provides recent updates on previous surveys and an opportunity to re-examine predictions and speculations from the literature. The objects in this work have WR CSs that are classified [WC] (Hen3-1333, Hen2-113) and other recent work by Dsilva et al. (2020) discuss a survey for more massive Galactic WR CSs. The objects in their work are more massive and of different classes but are similar in their fast wind properties that may result in pulsations, likely as the short period variability seen in our work. Dsilva et al. (2020) indicate that their sample has a lack of close period binaries, but rather a large fraction have long period systems, is consistent with this work. Hence more binary WR stars can be found using techniques that are similar to those in our work. Continued work on surveys of such objects will improve on the population of binaries in such objects and improve our understanding of such systems.

5.2 Future work

Binarity was not confirmed for the objects in our work but there is an open possibility for long orbital periods. To continue the investigation and search for these systems the following future work is suggested:

- continued long-term monitoring of the objects with SALT HRS and maintain the excellent quality of data.
- using data from other facilities such the NEOWISE-R data which explores mainly the infrared wavebands, this could be helpful with figuring out the variability that may be due to the pulsation affects and dust in these objects.
- expand the sample with objects that are similar, (WR CSPNe that exhibit the features discussed) such as M1-12 and M1-37, these are both multipolar PNe and M1-37 is often referred to as a Hen2-47 twin (Sahai 2000).
- consider other methods of analysis for time-series data. These can include trailed diagrams of the spectra, by producing dynamical power spectra. This could lead to clearer variability trends with the tracing of the CIII line and lead to periodicities that are consistent with long orbital periods.

Appendix A

Tables

Table A.1: *Observation and Julian dates for Hen3-1333, including the program proposal IDs (* bad spectra removed for results).*

Date of observation	Julian Date	Exposure time (s)	Proposal ID
2017-02-18	2457802.62173	300	2016-2-SCI-034
2017-03-16	2457828.56404	300	2016-2-SCI-034
2017-04-16	2457859.50004	300	2016-2-SCI-034
2017-05-05	2457879.4290	300	2017-1-MLT-010
2017-05-10	2457883.63281	300	2017-1-MLT-010
2017-05-15	2457888.6517	300	2017-1-MLT-010
2017-06-29	2457934.47001	300	2017-1-MLT-010
2017-07-01	2457936.46537	300	2017-1-MLT-010
2017-07-19	2457954.41331	300	2017-1-MLT-010
2017-07-24	2457959.41255	300	2017-1-MLT-010
2017-07-28	2457963.40543	300	2017-1-MLT-010
2017-07-29	2457964.41812	300	2017-1-MLT-010
2017-07-30	2457965.38843	300	2017-1-MLT-010
2017-08-06	2457972.38816	275	2017-1-MLT-010
2017-08-09	2457975.36038	275	2017-1-MLT-010
2017-08-12	2457978.37557	275	2017-1-MLT-010
2017-08-13	2457979.34525	275	2017-1-MLT-010
2017-08-14	2457980.35112	600	2017-1-MLT-010
2017-09-07	2458004.3122	300	2017-1-MLT-010
2017-09-08	2458005.2814	300	2017-1-MLT-010
2018-07-20	2458320.20883	300	2017-1-MLT-010
2018-07-21	2458321.43943	300	2017-1-MLT-010
2018-07-23	2458323.41182	300	2017-1-MLT-010
2019-05-15	2458618.60479	240	2018-2-MLT-007

Table A.1: *Observation and Julian dates for Hen3-1333, including the program proposal IDs (continued).*

2019-05-16	2458619.6477*	240	2018-2-MLT-007
2019-05-17	2458620.64285	240	2018-2-MLT-007
2019-05-18	2458621.58609	240	2018-2-MLT-007
2019-05-18	2458622.42057	240	2018-2-MLT-007
2019-05-20	2458623.59537	240	2018-2-MLT-007
2019-05-23	2458626.59251	240	2018-2-MLT-007
2019-05-25	2458628.61822	240	2018-2-MLT-007
2019-06-01	2458636.35342*	240	2018-2-MLT-007
2019-06-07	2458641.56818	240	2018-2-MLT-007
2019-06-11	2458645.54761	240	2018-2-MLT-007
2019-06-14	2458648.51252	240	2018-2-MLT-007
2019-06-15	2458649.517	240	2018-2-MLT-007
2019-06-16	2458650.51253	240	2018-2-MLT-007
2019-06-18	2458652.50042	240	2018-2-MLT-007
2019-07-27	2458692.39925	240	2018-2-MLT-007
2019-08-02	2458698.43429	240	2018-2-MLT-007
2019-08-03	2458699.37275	240	2018-2-MLT-007
2019-08-06	2458702.37913	240	2018-2-MLT-007
2019-08-13	2458709.3913	240	2018-2-MLT-007
2019-08-13	2458709.39916	240	2018-2-MLT-007
2019-08-14	2458710.38993	240	2018-2-MLT-007
2019-08-16	2458712.38776	240	2018-2-MLT-007
2019-08-20	2458716.35114	240	2018-2-MLT-007
2019-08-25	2458721.31119	240	2018-2-MLT-007
2019-08-28	2458724.30621	240	2018-2-MLT-007
2019-08-29	2458725.30895	240	2018-2-MLT-007
2019-08-30	2458726.29806*	157	2018-2-MLT-007
2019-09-02	2458729.29142	240	2018-2-MLT-007
2019-09-04	2458731.28775*	480	2018-2-MLT-007
2019-09-06	2458733.30586	240	2018-2-MLT-007
2019-10-04	2458761.26023	240	2018-2-MLT-007
2019-10-06	2458763.2402	240	2018-2-MLT-007
2019-10-07	2458764.24473	240	2018-2-MLT-007
2019-10-08	2458765.24113	240	2018-2-MLT-007

Table A.2: *Observation and Julian dates for Hen2-113, including the program proposal IDs.*

Date of observation	Julian Date	Exposure time (s)	Proposal ID
2017-07-01	2457936.42193	600	2017-1-MLT-010
2017-07-03	2457938.4212	600	2017-1-MLT-010
2017-07-21	2457956.36563	600	2017-1-MLT-010
2017-07-26	2457961.35099	600	2017-1-MLT-010
2017-07-30	2457965.30932	560	2017-1-MLT-010
2017-08-02	2457968.30056	560	2017-1-MLT-010
2017-08-03	2457969.32332	560	2017-1-MLT-010
2017-08-05	2457971.30754	560	2017-1-MLT-010
2017-08-06	2457972.30458	560	2017-1-MLT-010
2017-08-07	2457973.30584	500	2017-1-MLT-010
2017-08-08	2457974.27942	500	2017-1-MLT-010
2017-08-09	2457975.27231	500	2017-1-MLT-010
2017-08-10	2457976.29566	500	2017-1-MLT-010
2017-08-12	2457978.28596	500	2017-1-MLT-010
2017-08-13	2457979.26571	500	2017-1-MLT-010
2017-08-14	2457980.27825	600	2017-1-MLT-010
2017-08-17	2457983.28613	290	2017-1-MLT-010
2017-08-18	2457984.26944	290	2017-1-MLT-010
2017-08-18	2457984.28548	400	2017-1-MLT-010
2017-08-19	2457985.28501	290	2017-1-MLT-010
2017-08-20	2457986.28075	290	2017-1-MLT-010
2017-08-23	2457989.25541	290	2017-1-MLT-010
2017-08-27	2457993.24327	290	2017-1-MLT-010
2017-09-07	2458004.2452	400	2017-1-MLT-010
2018-07-20	2458320.33878	450	2017-1-MLT-010
2018-07-22	2458322.34219	450	2017-1-MLT-010
2018-07-23	2458323.33445	450	2017-1-MLT-010
2019-05-12	2458615.56539	300	2018-2-MLT-007
2019-05-15	2458618.54261	300	2018-2-MLT-007
2019-05-17	2458620.53347	300	2018-2-MLT-007
2019-05-18	2458621.54954	300	2018-2-MLT-007
2019-05-19	2458622.52303	300	2018-2-MLT-007
2019-05-20	2458623.53502	300	2018-2-MLT-007
2019-05-23	2458626.53113	300	2018-2-MLT-007
2019-05-25	2458628.53416	300	2018-2-MLT-007
2019-06-10	2458645.23461	300	2018-2-MLT-007
2019-06-13	2458648.48459	300	2018-2-MLT-007
2019-06-17	2458652.45519	300	2018-2-MLT-007

Table A.2: *Observation and Julian dates for Hen2-113, including the program proposal IDs (continued).*

2019-06-20	2458655.42673	300	2018-2-MLT-007
2019-06-23	2458658.43585	300	2018-2-MLT-007
2019-07-04	2458669.39093	300	2018-2-MLT-007
2019-07-05	2458670.41392	300	2018-2-MLT-007
2019-07-20	2458685.33689	300	2018-2-MLT-007
2019-07-21	2458686.35764	300	2018-2-MLT-007
2019-07-25	2458690.32289	300	2018-2-MLT-007
2019-07-26	2458691.36629	300	2018-2-MLT-007
2019-08-02	2458698.33166	300	2018-2-MLT-007
2019-08-06	2458702.30297	300	2018-2-MLT-007
2019-08-09	2458705.32004	300	2018-2-MLT-007
2019-08-13	2458709.28298	300	2018-2-MLT-007
2019-08-14	2458710.28561	300	2018-2-MLT-007
2019-08-15	2458711.29046	300	2018-2-MLT-007
2019-08-16	2458712.27447	300	2018-2-MLT-007
2019-08-17	2458713.26524	300	2018-2-MLT-007
2019-08-18	2458714.29736	300	2018-2-MLT-007
2019-08-21	2458717.2958	300	2018-2-MLT-007
2019-08-22	2458718.29369	300	2018-2-MLT-007
2019-08-28	2458724.23758	300	2018-2-MLT-007
2019-09-02	2458729.23456	300	2018-2-MLT-007
2019-09-03	2458730.22791	300	2018-2-MLT-007

Table A.3: *Observation and Julian dates for Hen2-47, including the program proposal IDs.*

Date of observation	Julian Date	Exposure time (s)	Proposal ID
2016-12-15	2457737.52117	1850	2016-2-SCI-034
2017-01-08	2457762.45509	1850	2016-2-SCI-034
2017-02-04	2457789.41243	1850	2016-2-SCI-034
2017-03-06	2457819.34303	1850	2016-2-SCI-034
2017-04-02	2457846.26218	1850	2016-2-SCI-034
2017-04-15	2457859.41783	1850	2016-2-SCI-034
2017-04-19	2457863.3942	1850	2017-1-MLT-010
2017-04-27	2457871.37723	1850	2017-1-MLT-010
2017-05-04	2457878.32189	1850	2017-1-MLT-010
2017-05-09	2457883.36416	1850	2017-1-MLT-010
2017-05-30	2457904.24935	1850	2017-1-MLT-010
2017-06-12	2457917.25669	1850	2017-1-MLT-010
2017-06-17	2457922.25916	1850	2017-1-MLT-010
2017-06-30	2457935.21444	2150	2017-1-MLT-010

Table A.3: *Observation and Julian dates for Hen2-47, including the program proposal IDs (continued).*

2017-07-01	2457936.21131	1850	2017-1-MLT-010
2017-07-05	2457940.21347	1850	2017-1-MLT-010
2018-01-18	2458137.45123	1850	2017-1-MLT-010
2018-02-01	2458151.41081	1850	2017-1-MLT-010
2018-02-06	2458155.55867	1850	2017-1-MLT-010
2018-02-22	2458172.35104	1850	2017-1-MLT-010
2018-04-30	2458239.3679	1850	2017-1-MLT-010
2018-05-03	2458242.32602	1850	2017-1-MLT-010
2018-12-25	2458477.53489	1850	2018-2-MLT-007
2019-01-07	2458491.48047	1850	2018-2-MLT-007
2019-01-13	2458497.48206	1850	2018-2-MLT-007
2019-01-20	2458504.46175	1850	2018-2-MLT-007
2019-01-21	2458505.4322	1850	2018-2-MLT-007
2019-01-22	2458506.40136	1850	2018-2-MLT-007
2019-01-23	2458507.45524	1850	2018-2-MLT-007
2019-01-24	2458508.45078	1850	2018-2-MLT-007
2019-05-14	2458618.32155	1200	2018-2-MLT-007
2019-05-16	2458620.30706	1200	2018-2-MLT-007
2019-05-17	2458621.2928	1200	2018-2-MLT-007
2019-05-19	2458623.33486	1200	2018-2-MLT-007
2019-06-10	2458645.24473	1200	2018-2-MLT-007

Table A.4: *Hen3-1333 cross correlation velocities for the blue and the red SALT spectra.*

	Cross correlation Blue Spectra		Cross correlation Red Spectra	
Julian Date JD	RV (km/s)	σ (km/s)	RV (km/s)	σ (km/s)
2457802.62173	−0.63	1.11	−0.35	0.64
2457828.56404	−0.47	1.03	−2.55	0.71
2457859.50004	3.86	0.66	0.97	0.81
2457879.429	−0.80	0.63	−0.49	0.65
2457883.63281	3.76	1.22	2.84	0.64
2457888.6517	−4.08	1.13	−1.73	0.65
2457934.47001	−1.85	3.38	−1.86	0.63
2457936.46537	0.59	0.63	−0.40	0.53
2457954.41331	0.14	1.00	−0.30	0.47
2457959.41255	−0.85	0.95	0.02	0.89
2457963.40543	2.59	1.16	1.58	0.53
2457964.41812	−0.56	0.46	−0.69	0.57
2457965.38843	−2.75	0.81	−0.77	0.91

Table A.4: *Hen3-1333 cross correlation velocities for the blue and the red SALT spectra (continued).*

2457972.38816	−0.86	0.62	−0.83	0.64
2457975.36038	−4.98	0.56	−2.87	0.82
2457978.37557	−1.04	1.02	−0.79	0.61
2457979.34525	3.03	0.71	2.90	0.64
2457980.35112	−2.84	1.62	−0.71	1.40
2458004.3122	−4.27	0.65	−3.61	0.75
2458005.2814	1.98	1.11	0.56	0.74
2458320.20883	−2.95	0.73	1.20	0.76
2458321.43943	−4.21	0.89	1.79	0.69
2458323.41182	−0.07	0.54	−0.16	0.84
2458618.60479	−2.40	1.56	−1.68	1.50
2458620.64285	−3.12	0.65	−3.62	0.78
2458621.58609	3.65	0.58	1.60	0.96
2458622.42057	−0.41	0.73	−0.74	1.51
2458623.59537	−1.98	0.61	−0.88	0.66
2458626.59251	−3.75	0.78	−2.56	0.55
2458628.61822	−5.27	0.78	−4.25	1.03
2458641.56818	−2.34	0.93	−3.71	0.90
2458645.54761	3.47	0.78	1.21	0.96
2458648.51252	−6.93	0.68	−5.09	1.25
2458649.517	−6.70	0.75	−4.93	0.8
2458650.51253	−1.44	0.99	−2.97	0.93
2458652.50042	2.54	0.72	1.29	0.78
2458692.39925	−0.31	3.11	−3.94	0.99
2458698.43429	5.30	0.52	0.54	0.80
2458699.37275	5.64	1.10	20	0.75
2458702.37913	3.70	0.62	0.42	0.67
2458709.3913	−3.08	0.79	−2.76	1.39
2458709.39916	−3.06	0.60	−3.89	0.88
2458710.38993	−5.20	0.51	−5.52	0.60
2458712.38776	−5.10	0.71	−4.64	0.67
2458716.35114	−3.01	0.58	−2.32	0.58
2458721.31119	−0.41	1.02	−1.34	0.75
2458724.30621	−0.15	2.53	−1.38	0.93
2458725.30895	−3.27	0.52	−3.27	1.11
2458726.29806	−0.02	8.92	−13.8	7.41
2458729.29142	−3.62	0.53	−4.03	0.55
2458733.30586	−0.08	0.67	0.25	5.30

Table A.4: *Hen3-1333 cross correlation velocities for the blue and the red SALT spectra (continued).*

2458761.26023	−0.43	0.65	−1.57	0.67
2458763.2402	0.18	1.61	−1.86	1.84
2458764.24473	2.46	0.66	−1.38	1.51
2458765.24113	1.84	0.91	−2.66	0.63

Table A.5: *Hen2-113 cross correlation velocities for the blue and the red SALT spectra.*

	Cross correlation Blue Spectra		Cross correlation Red Spectra	
Julian Date JD	RV (km/s)	σ (km/s)	RV (km/s)	σ (km/s)
2457936.42193	2.36	0.64	−3.75	0.66
2457938.4212	2.23	0.65	−5.98	0.77
2457956.36563	3.76	0.62	−0.47	0.52
2457961.35099	0.88	0.59	−10.13	0.51
2457965.30932	0.72	0.43	−8.78	0.49
2457968.30056	2.26	0.52	−4.43	0.55
2457969.32332	2.18	0.58	−5.61	0.55
2457971.30754	1.15	0.69	−6.73	0.77
2457972.30458	2.27	0.73	−3.98	0.60
2457973.30584	2.79	0.56	−6.02	0.50
2457974.27942	3.97	0.65	−0.25	0.65
2457975.27231	2.04	0.57	−5.07	0.64
2457976.29566	2.80	1.33	−6.74	0.83
2457978.28596	1.33	0.39	−6.59	0.49
2457979.26571	1.84	0.76	−6.27	1.93
2457980.27825	3.02	0.54	−4.23	0.53
2457983.28613	1.96	0.65	−3.97	1.01
2457984.26944	2.19	0.80	−4.87	0.97
2457984.28548	1.78	0.82	−4.76	0.95
2457985.28501	1.98	0.74	−5.22	0.52
2457986.28075	1.53	1.17	−6.92	0.91
2457989.25541	3.75	0.55	−3.35	0.45
2457993.24327	2.80	1.19	−0.77	2.57
2458004.2452	1.40	0.68	−6.41	0.80
2458320.33878	3.48	0.81	−0.74	0.73
2458322.34219	2.46	0.57	−4.74	0.46
2458323.33445	2.87	0.57	−3.69	0.75
2458615.56539	3.97	1.01	−8.03	4.02
2458618.54261	3.83	0.61	−3.80	0.56
2458620.53347	4.33	0.63	−3.73	0.70

Table A.5: *Hen2-113 cross correlation velocities for the blue and the red SALT spectra (continued).*

2458621.54954	2.54	0.82	−6.01	1.18
2458622.52303	2.93	0.60	−3.48	0.77
2458623.53502	2.61	0.67	−4.75	0.74
2458626.53113	4.16	0.90	−4.89	0.80
2458628.53416	3.48	0.80	−2.92	0.78
2458645.23461	1.35	0.61	−10.12	0.59
2458648.48459	3.16	0.56	−3.99	0.38
2458652.45519	5.13	0.61	−0.74	0.59
2458655.42673	2.84	0.71	−5.32	0.76
2458658.43585	2.46	0.72	−5.63	0.83
2458669.39093	5.35	2.83	−2.38	0.71
2458670.41392	3.56	2.93	−4.36	0.68
2458685.33689	3.57	1.04	−6.11	2.31
2458686.35764	2.90	0.83	−4.86	0.94
2458690.32289	2.19	1.43	−5.09	2.41
2458691.36629	2.72	0.66	−5.09	0.62
2458698.33166	4.10	0.55	−4.86	1.12
2458702.30297	2.44	0.83	−8.77	0.74
2458705.32004	2.24	0.38	−7.47	0.54
2458709.28298	3.71	0.35	−5.64	0.77
2458710.28561	2.46	0.57	−6.68	0.66
2458711.29046	3.28	0.62	−5.67	1.16
2458712.27447	2.21	0.72	−8.04	0.63
2458713.26524	4.32	0.39	−1.75	0.65
2458714.29736	4.69	0.77	−4.03	2.79
2458717.2958	3.18	0.56	−6.43	0.67
2458718.29369	4.75	0.70	−3.28	1.03
2458724.23758	4.47	0.52	−0.06	0.58
2458729.23456	2.85	0.54	−5.27	0.67
2458730.22791	3.36	0.53	−3.49	0.47

Table A.6: *Hen2-47 cross correlation velocities for the blue and the red SALT spectra.*

	Cross correlation Blue Spectra		Cross correlation Red Spectra	
Julian Date JD	RV (km/s)	σ (km/s)	RV (km/s)	σ (km/s)
2457737.52117	0.49	0.29	−0.22	0.41
2457762.45509	0.18	0.23	−0.38	0.10
2457789.41243	0.28	0.23	−0.23	0.27
2457819.34303	0.69	0.11	−0.56	0.33

Table A.6: *Hen2-47 cross correlation velocities for the blue and the red SALT spectra (continued).*

2457846.26218	0.89	0.26	−0.95	0.23
2457859.41783	0.77	0.30	−0.25	0.70
2457863.3942	0.79	0.26	−0.46	0.29
2457871.37723	0.69	0.07	−1.25	0.37
2457878.32189	0.678	0.11	−0.84	0.41
2457883.36416	0.52	0.25	−0.25	0.17
2457904.24935	0.54	0.12	−0.21	0.47
2457917.25669	0.28	0.27	−0.70	0.27
2457922.25916	0.28	0.09	−0.60	0.45
2457935.21444	0.54	0.26	−0.41	0.26
2457936.21131	0.50	0.18	−0.21	0.68
2457940.21347	0.36	0.57	−0.04	0.24
2458137.45123	0.57	0.59	0.17	1.63
2458151.41081	0.59	0.14	−0.11	0.50
2458155.55867	0.51	0.29	0.35	0.58
2458172.35104	0.63	0.17	−0.39	0.42
2458239.3679	0.22	0.18	−0.67	0.73
2458242.32602	0.16	0.31	−0.41	0.59
2458477.53489	0.79	0.08	−0.31	0.43
2458491.48047	0.80	0.33	−0.75	1.22
2458497.48206	0.84	0.40	−0.51	0.26
2458504.46175	0.71	0.25	−0.07	0.28
2458505.4322	0.73	0.18	−0.38	0.16
2458506.40136	0.701	0.13	−0.48	0.26
2458507.45524	0.95	0.31	0.02	0.59
2458508.45078	0.56	0.14	−0.27	0.45
2458618.32155	0.50	0.32	−1.06	0.41
2458620.30706	0.34	0.38	−1.38	0.36
2458621.2928	0.55	0.17	−1.23	0.83
2458623.33486	0.48	0.27	−1.57	0.54
2458645.24473	0.45	0.10	−1.53	0.93

Table A.7: *Hen3-1333 CIII line (5695 Å) Gaussian profile velocities.*

Julian Date JD	RV (km/s)	σ (km/s)
2457802.6217	-37.67	0.43
2457828.5640	-39.11	0.64
2457859.5000	-42.30	0.44
2457879.4290	-37.56	0.52
2457883.6328	-39.96	0.52

Table A.7: *Hen3-1333 CIII line (5695 Å) Gaussian profile velocities (continued).*

2457888.6517	-34.86	0.50
2457934.4700	-32.44	0.51
2457936.4654	-34.14	0.43
2457954.4133	-35.88	0.46
2457959.4126	-43.09	0.54
2457963.4054	-34.20	0.39
2457964.4181	-37.08	0.39
2457965.3884	-36.20	0.41
2457972.3882	-35.13	0.43
2457975.3604	-43.96	0.58
2457978.3756	-51.90	2.91
2457979.3453	-37.40	0.49
2457980.3511	-38.10	0.87
2458004.3122	-36.41	0.51
2458005.2814	-35.64	0.46
2458320.2088	-31.55	0.44
2458321.4394	-37.08	0.46
2458323.4118	-42.63	0.46
2458618.6048	-33.26	0.45
2458620.6429	-41.44	0.63
2458621.5861	-40.04	0.44
2458622.4206	-35.46	0.57
2458623.5954	-38.41	0.57
2458626.5925	-36.66	0.44
2458628.6182	-36.18	0.52
2458641.5682	-36.08	0.53
2458645.5476	-35.89	0.53
2458648.5125	-50.21	1.36
2458649.5170	-38.96	0.76
2458650.5125	-35.60	0.45
2458652.5004	-40.73	0.48
2458692.3993	-37.23	0.43
2458698.4343	-35.31	0.44
2458699.3728	-36.19	0.50
2458702.3791	-42.94	0.49
2458709.3913	-36.63	0.63
2458709.3992	-39.60	0.48
2458710.3899	-37.60	0.48
2458712.3878	-33.03	0.46
2458716.3511	-37.02	0.54

Table A.7: *Hen3-1333 CIII line (5695 Å) Gaussian profile velocities (continued).*

2458721.3112	-30.28	0.53
2458724.3062	-38.95	0.52
2458725.3090	-30.96	0.42
2458726.2981	-39.08	0.51
2458729.2914	-33.64	0.50
2458733.3059	-36.86	0.45
2458761.2602	-35.82	0.50
2458763.2402	-68.15	3.07
2458764.2447	-34.54	0.57
2458765.2411	-37.21	0.56

Table A.8: *Hen2-113 CIII line (5695 Å) Gaussian profile velocities.*

Julian Date JD	RV (km/s)	σ (km/s)
2457936.4219	-42.83	0.38
2457938.4212	-42.00	0.38
2457956.3656	-37.14	0.49
2457961.3510	-46.96	0.41
2457965.3093	-45.85	0.44
2457968.3006	-49.85	0.46
2457969.3233	-39.11	0.49
2457971.3075	-46.99	0.44
2457972.3046	-44.74	0.46
2457973.3058	-40.69	0.37
2457974.2794	-42.82	0.49
2457975.2723	-38.01	0.52
2457976.2957	-39.49	0.34
2457978.2860	-52.79	0.35
2457979.2657	-41.33	0.50
2457980.2783	-44.30	0.54
2457983.2861	-42.46	0.50
2457984.2694	-43.94	0.48
2457984.2855	-41.14	0.46
2457985.2850	-40.69	0.43
2457986.2808	-42.22	0.44
2457989.2554	-39.92	0.37
2457993.2433	-42.17	0.64
2458004.2452	-36.82	0.38
2458320.3388	-45.40	0.44
2458322.3422	-46.00	0.32

Table A.8: *Hen2-113 CIII line (5695 Å) Gaussian profile velocities (continued).*

2458323.3345	-44.44	0.45
2458615.5654	-41.26	0.47
2458618.5426	-41.66	0.44
2458620.5335	-42.66	0.38
2458621.5495	-41.47	0.38
2458622.5230	-44.28	0.41
2458623.5350	-45.47	0.40
2458626.5311	-45.31	0.49
2458628.5342	-40.82	0.46
2458645.2346	-44.69	0.39
2458648.4846	-41.71	0.46
2458652.4552	-46.13	0.44
2458655.4267	-43.79	0.44
2458658.4359	-50.23	1.86
2458669.3909	-43.90	0.48
2458670.4139	-41.05	0.41
2458685.3369	-43.04	0.37
2458686.3576	-42.34	0.44
2458690.3229	-44.21	0.50
2458691.3663	-43.81	0.37
2458698.3317	-46.06	0.39
2458702.3030	-48.44	0.87
2458705.3200	-40.11	0.44
2458709.2830	-42.15	0.54
2458710.2856	-41.60	0.38
2458711.2905	-45.11	0.57
2458712.2745	-45.04	0.55
2458713.2652	-46.78	0.43
2458714.2974	-42.53	0.44
2458717.2958	-40.38	0.45
2458718.2937	-46.22	0.39
2458724.2376	-50.33	0.42
2458729.2346	-36.26	0.40
2458730.2279	-40.38	0.37

Table A.9: *Hen2-47 CIII line (5695 Å) Gaussian profile velocities.*

Julian Date JD	RV (km/s)	σ (km/s)
2457737.5212	-12.55	0.28
2457762.4551	-7.11	0.23
2457789.4124	-6.34	0.19
2457819.3430	-12.94	0.18
2457846.2622	-12.87	0.20
2457859.4178	-10.74	0.29
2457863.3942	-15.19	0.44
2457871.3772	-6.39	0.17
2457878.3219	-12.57	0.20
2457883.3642	-15.18	0.15
2457904.2494	-8.47	0.43
2457917.2567	-9.45	0.44
2457922.2592	-11.57	1.35
2457935.2144	-18.38	0.22
2457936.2113	-8.86	0.20
2457940.2135	-19.67	0.21
2458137.4512	-9.98	0.22
2458151.4108	-8.31	0.22
2458155.5587	-7.83	0.29
2458172.3510	-12.89	0.36
2458239.3679	-7.76	0.52
2458242.3260	-14.27	0.24
2458477.5349	-12.01	0.17
2458491.4805	-13.87	0.24
2458497.4821	-13.98	0.24
2458504.4618	-15.92	0.52
2458505.4322	-12.89	0.17
2458506.4014	-15.49	0.21
2458507.4552	-5.44	0.24
2458508.4508	-18.92	0.18
2458618.3216	-19.66	0.18
2458620.3071	-12.21	0.21
2458621.2928	-7.08	0.23
2458623.3349	-10.83	0.23
2458645.2447	-11.83	0.23

Appendix B

List of abbreviations

Table B.1: *Table of abbreviations and acronyms used in the text.*

Abbrev/Acronym	Full meaning
AGB	Asymptotic Giant Branch
CE	Common Envelope
CM	Centre of Mass
CS	Central Star
CSPNe	Central Star of Planetary Nebulae
CTIO	Cerro Tololo Interamerican Observatory
FFI	Full Frame Image
FWHM	Full Width Half Maximum
GISW	Generalized Interacting Stellar Wind model
HERMES	High-Efficiency and high-Resolution Mercator Échelle Spectrograph
HR	High Resolution
HRS	High Resolution Spectrograph
HS	High Stability
IDS	Intermediate Dispersion Spectrograph
INT	Isaac Newton Telescope
IRAF	Image Reduction and Analysis Facility
ISM	Interstellar Medium
ISO	Infrared Space Observatory
ISW	Interacting Stellar Wind model
LR	Low Resolution
LMF	Luminosity Function
LMFIT	Levenberg Marquardt Fitting Technique
LTP	Late Thermal Pulse
MAST	Mikulski Archive for Space Telescopes
MR	Medium Resolution

Table B.1: *Table of abbreviations and acronyms used in the text (continued).*

NEOWISE	Near-Earth Object Wide-field Infrared Survey Explorer
PCEB	Post-Common Envelope Binaries
PN	Planetary Nebula
PNe	Planetary Nebulae
PNNi	Planetary Nebula Nuclei
PPNe	Pre-Planetary Nebulae
Pop I	Population I
Pop II	Population II
RCB	R Coronae Borealis
RSS	Robert Stobie Spectrograph
RV	Radial Velocity
SAAO	South African Astronomical Observatory
SALT	Southern African Large Telescope
SED	Spectral Energy Distribution
SMARTS	Small and Moderate Aperture Research Telescope System
S/N	Signal to Noise
TESS	The Exoplanet Survey Satellite
VLTI	Very Large Telescope Interferometer
VPH	Volume Phase Holographic
WC	Wolf-Rayet Carbon type
WD	White Dwarf
WDMS	White Dwarf Main Sequence
WIYN	Winsconsin-Idiana-Yale-NOAO Telescope
WN	Wolf-Rayet Nitrogen type
WO	Wolf-Rayet Oxygen type
WR	Wolf-Rayet

Bibliography

M. Afsar and H. E. Bond. Radial-Velocity Survey of Central Stars of Southern Planetary Nebulae . Mem. Soc. Astron. Italiana, 76:608, January 2005.

C. Alcock, R. A. Allsman, D. R. Alves, T. S. Axelrod, A. Becker, D. P. Bennett, Geoffrey C. Clayton, K. H. Cook, N. Dalal, A. J. Drake, K. C. Freeman, M. Geha, K. D. Gordon, K. Griest, D. Kilkenny, M. J. Lehner, S. L. Marshall, D. Minniti, K. A. Misselt, C. A. Nelson, B. A. Peterson, P. Popowski, M. R. Pratt, P. J. Quinn, C. W. Stubbs, W. Sutherland , A. Tomaney, T. Vandehei, and D. L. Welch. The MACHO Project LMC Variable Star Inventory. X. The R Coronae Borealis Stars. ApJ, 554(1):298–315, June 2001. doi: 10.1086/321369.

S. Aniyan, K. C. Freeman, M. Arnaboldi, O. Gerhard, L. Coccato, M. Fabricius, K. Kuijken, and M. Merrifield. Resolving the Disk-Halo Degeneracy using Planetary Nebulae. In X. Liu, L. Stanghellini, and A. Karakas, editors, *Planetary Nebulae: Multi-Wavelength Probes of Stellar and Galactic Evolution*, volume 323 of *IAU Symposium*, pages 284–287, October 2017. doi: 10.1017/S1743921317001144.

Bruce Balick and Adam Frank. Shapes and Shaping of Planetary Nebulae. ARA&A, 40: 439–486, January 2002. doi: 10.1146/annurev.astro.40.060401.093849.

Bruce Balick, Martín Huarte-Espinosa, Adam Frank, Thomas Gomez, Javier Alcolea, Romano L. M. Corradi, and Dejan Vinković. Outflows from Evolved Stars: The Rapidly Changing Fingers of CRL 618. ApJ, 772(1):20, July 2013. doi: 10.1088/0004-637X/772/1/20.

Bruce Balick, Adam Frank, and Baowei Liu. Models of the Mass-ejection Histories of Preplanetary Nebulae. III. The Shaping of Lobes by Post-AGB Winds. ApJ, 877(1):30, May 2019. doi: 10.3847/1538-4357/ab16f5.

P. Ballester. Reduction of Echelle Spectra with MIDAS. In *European Southern Observatory Conference and Workshop Proceedings*, volume 41 of *European Southern Observatory Conference and Workshop Proceedings*, page 177, June 1992.

G. Barentsen and Lightkurve Collaboration. Lightkurve: An accessible Python package for

TESS & Kepler time series analysis. In *American Astronomical Society Meeting Abstracts*, American Astronomical Society Meeting Abstracts, page 409.04, January 2020.

M. J. Barlow. ISO LWS Observations of Cool Evolved Stars and Post-AGB Objects. Ap&SS, 255:315–323, January 1998. doi: 10.1023/A:1001587707752.

S. I. Barnes, P. L. Cottrell, M. D. Albrow, N. Frost, G. Graham, G. Kershaw, R. Ritchie, D. Jones, R. Sharples, D. Bramall, J. Schmoll, P. Luke, P. Clark, L. Tyas, D. A. H. Buckley, and J. Brink. *The optical design of the Southern African Large Telescope high resolution spectrograph: SALT HRS*, volume 7014 of *Society of Photo-Optical Instrumentation Engineers (SPIE) Conference Series*, page 70140K. 2008. doi: 10.1117/12.788219.

P. Bartzakos, A. F. J. Moffat, and V. S. Niemela. Magellanic Cloud WC/WO Wolf-Rayet stars - II. Colliding winds in binaries. MNRAS, 324(1):33–50, June 2001. doi: 10.1046/j.1365-8711.2001.04127.x.

Eric G. Blackman. Magnetic fields in Planetary Nebulae: paradigms and related MHD frontiers. In Klaus G. Strassmeier, Alexander G. Kosovichev, and John E. Beckman, editors, *Cosmic Magnetic Fields: From Planets, to Stars and Galaxies*, volume 259 of *IAU Symposium*, pages 35–46, April 2009. doi: 10.1017/S174392130903004X.

Henri M. J. Boffin, Brent Miszalski, Thomas Rauch, David Jones, Romano L. M. Corradi, Ralf Napiwotzki, Avril C. Day-Jones, and Joachim Köppen. An Interacting Binary System Powers Precessing Outflows of an Evolved Star. *Science*, 338(6108):773, November 2012. doi: 10.1126/science.1225386.

Howard E. Bond. *Binarity of Central Stars of Planetary Nebulae*, volume 199 of *Astronomical Society of the Pacific Conference Series*, page 115. 2000.

Howard E. Bond. Spectroscopic binaries in planetary nebulae. *AIP Conference Proceedings*, 2005. ISSN 0094-243X. doi: 10.1063/1.2146263. URL `http://dx.doi.org/10.1063/1.2146263`.

D. G. Bramall, R. Sharples, L. Tyas, J. Schmoll, P. Clark, P. Luke, N. Looker, N. A. Dipper, S. Ryan, D. A. H. Buckley, J. Brink, and S. I. Barnes. The SALT HRS spectrograph: final design, instrument capabilities, and operational modes. In Proc. SPIE, volume 7735 of *Society of Photo-Optical Instrumentation Engineers (SPIE) Conference Series*, page 77354F, July 2010. doi: 10.1117/12.856382.

C. E. Brasseur, Carlita Phillip, Scott W. Fleming, S. E. Mullally, and Richard L. White. Astrocut: Tools for creating cutouts of TESS images, May 2019.

David A. H. Buckley, Gerhard P. Swart, and Jacobus G. Meiring. Completion and commissioning of the Southern African Large Telescope. In Proc. SPIE, volume 6267 of *Society of Photo-Optical Instrumentation Engineers (SPIE) Conference Series*, page 62670Z, June 2006. doi: 10.1117/12.673750.

V. Bujarrabal, A. Castro-Carrizo, H. Van Winckel, J. Alcolea, C. Sánchez Contreras, M. Santand er-García, and M. Hillen. High-resolution observations of IRAS 08544-4431. Detection of a disk orbiting a post-AGB star and of a slow disk wind. A&A, 614:A58, June 2018. doi: 10.1051/0004-6361/201732422.

N. Calvet and M. Peimbert. Bipolar nebulae and type I planetary nebulae. In L. H. Aller, editor, *Planetary Nebulae*, volume 103 of *IAU Symposium*, page 546, January 1983.

Luke Chamandy, Yisheng Tu, Eric G. Blackman, Jonathan Carroll-Nellenback, Adam Frank, Baowei Liu, and Jason Nordhaus. Energy budget and core-envelope motion in common envelope evolution. MNRAS, 486(1):1070–1085, June 2019. doi: 10.1093/mnras/stz887.

O. Chesneau, A. Collioud, O. De Marco, S. Wolf, E. Lagadec, A. A. Zijlstra, A. Rothkopf, A. Acker, G. C. Clayton, and B. Lopez. A close look into the carbon disk at the core of the planetary nebula CPD-56°8032. A&A, 455(3):1009–1018, September 2006. doi: 10.1051/0004-6361:20054585.

R. Ciardullo. The Planetary Nebula Luminosity Function: Pieces of the Puzzle. , 27(2): 149–155, May 2010. doi: 10.1071/AS09022.

M. Cohen, M. J. Barlow, R. J. Sylvester, X. W. Liu, P. Cox, T. Lim, B. Schmitt, and A. K. Speck. Silicate and ice emission bands in the ISO spectrum of the PAH-emitting carbon-rich planetary nebula CPD–$56^{circ8032}$. In T. Le Bertre, A. Lebre, and C. Waelkens, editors, *Asymptotic Giant Branch Stars*, volume 191 of *IAU Symposium*, page 291, January 1999.

Martin Cohen, M. J. Barlow, X. W. Liu, and A. F. Jones. The dual dust chemistries of planetary nebulae with [WCL] central stars. MNRAS, 332(4):879–890, June 2002. doi: 10.1046/j.1365-8711.2002.05350.x.

Lisa A. Crause, Ray M. Sharples, David G. Bramall, Jürgen Schmoll, Paul Clark, Eddy J. Younger, Luke M. G. Tyas, Sean G. Ryan, Janus D. Brink, Ockert J. Strydom, David A. H. Buckley, Martin Wilkinson, Steven M. Crawford, and Éric Depagne. Performance of the Southern African Large Telescope (SALT) High Resolution Spectrograph (HRS). In Proc. SPIE, volume 9147 of *Society of Photo-Optical Instrumentation Engineers (SPIE) Conference Series*, page 91476T, July 2014. doi: 10.1117/12.2055635.

Steven M. Crawford, Martin Still, Pim Schellart, Luis Balona, David A. H. Buckley, Garith Dugmore, Amanda A. S. Gulbis, Alexei Kniazev, Marissa Kotze, Nicola Loaring, Kenneth H. Nordsieck, Timothy E. Pickering, Stephen Potter, Encarni Romero Colmenero, Petri Vaisanen, Theodore Williams, and Ewald Zietsman. *PySALT: the SALT science pipeline*, volume 7737 of *Society of Photo-Optical Instrumentation Engineers (SPIE) Conference Series*, page 773725. 2010. doi: 10.1117/12.857000.

P. A. Crowther, Orsola De Marco, and M. J. Barlow. Quantitative classification of WC and WO stars. MNRAS, 296(2):367–378, May 1998. doi: 10.1046/j.1365-8711.1998.01360.x.

A. Danehkar and Q. A. Parker. Spatially resolved kinematic observations of the planetary nebulae Hen 3-1333 and Hen 2-113. MNRAS, 449:L56–L59, April 2015. doi: 10.1093/mnrasl/slv022.

J. A. de Freitas Pacheco, R. D. D. Costa, F. X. de Araujo, and D. Petrini. Mass-loss rates and C/He ratios in the winds of the WC central stars of planetary nebulae. MNRAS, 260: 401–407, January 1993. doi: 10.1093/mnras/260.2.401.

Orsola De Marco. The Origin and Shaping of Planetary Nebulae: Putting the Binary Hypothesis to the Test. PASP, 121(878):316, April 2009. doi: 10.1086/597765.

Orsola De Marco and P. A. Crowther. The WC10 central stars CPD-56 deg8032 and He2-113 - II. Model analysis and comparison with nebular properties. MNRAS, 296(2):419–429, May 1998. doi: 10.1046/j.1365-8711.1998.01379.x.

Orsola De Marco and Noam Soker. A New Look at the Evolution of Wolf-Rayet Central Stars of Planetary Nebulae. PASP, 114(796):602–611, June 2002. doi: 10.1086/341691.

Orsola De Marco, M. J. Barlow, and M. Cohen. Discovery of an Edge-on Dust Disk around the [WC10] Central Star CPD -56°8032. ApJ, 574(1):L83–L86, July 2002a. doi: 10.1086/342277.

Orsola De Marco, Geoffrey C. Clayton, F. Herwig, D. L. Pollacco, J. S. Clark, and David Kilkenny. What Are the Hot R Coronae Borealis Stars? AJ, 123(6):3387–3408, June 2002b. doi: 10.1086/340569.

Orsola De Marco, Howard E. Bond, Dianne Harmer, and Andrew J. Fleming. Indications of a Large Fraction of Spectroscopic Binaries among Nuclei of Planetary Nebulae. ApJ, 602(2):L93–L96, February 2004. doi: 10.1086/382156.

Orsola De Marco, Todd C. Hillwig, and A. J. Smith. Binary Central Stars of Planetary Nebulae Discovered Through Photometric Variability. I. What we Know and what we would like to Find Out. AJ, 136(1):323–336, July 2008. doi: 10.1088/0004-6256/136/1/323.

Karan Dsilva, Tomer Shenar, Hugues Sana, and Pablo Marchant. A spectroscopic multiplicity survey of galactic wolf-rayet stars. i. the northern wc sequence, 2020.

Adina D. Feinstein, Benjamin T. Montet, Daniel Foreman-Mackey, Megan E. Bedell, Nicholas Saunders, Jacob L. Bean, Jessie L. Christiansen, Christina Hedges, Rodrigo Luger, Daniel Scolnic, and Jose Vinicius de Miranda Cardoso. eleanor: Extracted and systematics-corrected light curves for TESS-observed stars, April 2019.

Adam Frank. The Unity and Diversity of Planetary or Nebulae Radiation- Gasdynamics of PNe. II. AJ, 107:261, January 1994. doi: 10.1086/116850.

Adam Frank, Bruce Balick, and James Riley. Stellar Wind Paleontology: Shells and Halos of Planetary Nebulae. AJ, 100:1903, December 1990. doi: 10.1086/115646.

G. Garcia-Segura, N. Langer, M. Rozycka, M. M. Mac Low, and J. Franco. Shaping bipolar and elliptical Planetary Nebulae: Rotation and magnetic field. In H. J. Habing and H. J. G. L. M. Lamers, editors, *Planetary Nebulae*, volume 180 of *IAU Symposium*, page 226, January 1997.

G. García-Segura, E. Villaver, N. Langer, S. C. Yoon, and A. Manchado. Single Rotating Stars and the Formation of Bipolar Planetary Nebula. ApJ, 783(2):74, March 2014. doi: 10.1088/0004-637X/783/2/74.

Guillermo García-Segura, Ronald E. Taam, and Paul M. Ricker. Common Envelope Shaping of Planetary Nebulae. II. Magnetic Solutions and Self-Collimated Outflows. *arXiv e-prints*, art. arXiv:2003.06073, March 2020.

Aidan Gibbs, Alex Bixel, Benjamin V. Rackham, Dániel Apai, Martin Schlecker, Néstor Espinoza, Luigi Mancini, Wen-Ping Chen, Thomas Henning, Paul Gabor, Richard Boyle, Jose Perez Chavez, Allie Mousseau, Jeremy Dietrich, Quentin Jay Socia, Wing Ip, Chow-Choong Ngeow, An-Li Tsai, Asmita Bhand are, Victor Marian, Hans Baehr, Samantha Brown, Maximilian Häberle, Miriam Keppler, Karan Molaverdikhani, and Paula Sarkis. EDEN: Sensitivity Analysis and Transiting Planet Detection Limits for Nearby Late Red Dwarfs. AJ, 159(4):169, April 2020. doi: 10.3847/1538-3881/ab7926.

Denise R. Gonçalves. What do planetary nebulae and H II regions reveal about the chemical evolution of nearby dwarf galaxies? In Kristen B. W. McQuinn and Sabrina Stierwalt, editors, *Dwarf Galaxies: From the Deep Universe to the Present*, volume 344 of *IAU Symposium*, pages 161–177, October 2019. doi: 10.1017/S1743921318007408.

M. A. Guerrero, A. Manchado, and M. Serra-Ricart. K4-55: A Bipolar Planetary Nebula Observed near Pole-on. ApJ, 456:651, January 1996. doi: 10.1086/176686.

M. Hajduk, P. A. M. van Hoof, and A. A. Zijlstra. *Evolution of the Central Stars of Young Planetary Nebulae*, volume 493 of *Astronomical Society of the Pacific Conference Series*, page 533. 2015.

Sinhué A. R. Haro-Corzo, Pablo F. Velázquez, Alejandro C. Raga, Angels Riera, and Primoz Kajdic. Shaping Point- and Mirror-symmetric Protoplanetary Nebulae by the Orbital Motion of the Central Binary System. ApJ, 703(1):L18–L22, September 2009. doi: 10.1088/0004-637X/703/1/L18.

Falk Herwig. Evolution of Asymptotic Giant Branch Stars. ARA&A, 43(1):435–479, September 2005. doi: 10.1146/annurev.astro.43.072103.150600.

D. J. Hillier. An iterative method for the solution of the statistical and radiativeequilibrium equations in expanding atmospheres. A&A, 231:116–124, May 1990.

Chih-Hao Hsia, Wayne Chau, Yong Zhang, and Sun Kwok. Hubble Space Telescope Observations and Geometric Models of Compact Multipolar Planetary Nebulae. ApJ, 787(1): 25, May 2014. doi: 10.1088/0004-637X/787/1/25.

Chih-Hao Hsia, Yong Zhang, Sun Kwok, and Wayne Chau. A young multipolar planetary nebula in the making—IRAS 21282+5050. Ap&SS, 364(2):32, February 2019. doi: 10.1007/s10509-019-3523-2.

Po-Sheng Huang, Chin-Fei Lee, and Raghvendra Sahai. Evolution from Spherical AGB Wind to Multipolar Outflow in Pre-planetary Nebula IRAS 17150−3224. ApJ, 889(2):85, February 2020. doi: 10.3847/1538-4357/ab5f09.

V. Icke. Blowing bubbles. A&A, 202:177–188, August 1988.

N. Ivanova, S. Justham, X. Chen, O. De Marco, C. L. Fryer, E. Gaburov, H. Ge, E. Glebbeek, Z. Han, X. D. Li, G. Lu, T. Marsh, P. Podsiadlowski, A. Potter, N. Soker, R. Taam, T. M. Tauris, E. P. J. van den Heuvel, and R. F. Webbink. Common envelope evolution: where we stand and how we can move forward. A&A Rev., 21:59, February 2013. doi: 10.1007/s00159-013-0059-2.

G. H. Jacoby. The luminosity function for planetary nebulae and the number of planetary nebulae in local group galaxies. ApJS, 42:1–18, January 1980. doi: 10.1086/190642.

Jon M. Jenkins, Joseph D. Twicken, Sean McCauliff, Jennifer Campbell, Dwight Sanderfer, David Lung, Masoud Mansouri-Samani, Forrest Girouard, Peter Tenenbaum, Todd Klaus, Jeffrey C. Smith, Douglas A. Caldwell, A. D. Chacon, Christopher Henze, Cory Heiges, David W. Latham, Edward Morgan, Daryl Swade, Stephen Rinehart, and Roland Vanderspek. *The TESS science processing operations center*, volume 9913 of *Society of Photo-Optical Instrumentation Engineers (SPIE) Conference Series*, page 99133E. 2016. doi: 10.1117/12.2233418.

D. Jones, D. L. Mitchell, M. Lloyd, D. Pollacco, T. J. O'Brien, J. Meaburn, and N. M. H. Vaytet. The morphology and kinematics of the Fine Ring Nebula, planetary nebula Sp 1, and the shaping influence of its binary central star. MNRAS, 420(3):2271–2279, March 2012. doi: 10.1111/j.1365-2966.2011.20192.x.

D. Jones, H. Van Winckel, A. Aller, K. Exter, and O. De Marco. The long-period binary central stars of the planetary nebulae NGC 1514 and LoTr 5. A&A, 600:L9, April 2017. doi: 10.1051/0004-6361/201730700.

David Jones and Henri M. J. Boffin. On the possible triple central star system of PN SuWt 2: no ménage à trois at the heart of the Wedding Ring. MNRAS, 466(2):2034–2038, April 2017. doi: 10.1093/mnras/stw3191.

Taichi Kato, Daisaku Nogami, and Hajime Baba. The 1996-1997 Fading of V651 Monocerotis, the Binary Central Star of the Planetary Nebula NGC 2346. PASJ, 53(5):901–903, October 2001. doi: 10.1093/pasj/53.5.901.

R. L. Kingsburgh and M. J. Barlow. Elemental abundances for a sample of southern galactic planetary nebulae. MNRAS, 271:257–299, November 1994. doi: 10.1093/mnras/271.2.257.

A. Y. Kniazev, V. V. Gvaramadze, and L. N. Berdnikov. MN48: a new Galactic bona fide luminous blue variable revealed by Spitzer and SALT. MNRAS, 459(3):3068–3077, July 2016. doi: 10.1093/mnras/stw889.

Michael J. Kurtz and Douglas J. Mink. RVSAO 2.0: Digital Redshifts and Radial Velocities. PASP, 110(750):934–977, August 1998. doi: 10.1086/316207.

S. Kwok and B. J. Hrivnak. The search for proto-planetary nebulae. JRASC, 87(4):192–193, August 1993.

S. Kwok, C. R. Purton, and P. M. Fitzgerald. On the origin of planetary nebulae. ApJ, 219: L125–L127, February 1978. doi: 10.1086/182621.

Sun Kwok. *The Origin and Evolution of Planetary Nebulae*. 2000.

Sun Kwok. Planetary Nebulae: New Challenges in the 21st Century. *Journal of Korean Astronomical Society*, 38(2):271–278, June 2005. doi: 10.5303/JKAS.2005.38.2.271.

E. Lagadec, O. Chesneau, M. Matsuura, O. De Marco, J. A. de Freitas Pacheco, A. A. Zijlstra, A. Acker, G. C. Clayton, and B. Lopez. New insights on the complex planetary nebula Hen 2-113. A&A, 448(1):203–212, March 2006. doi: 10.1051/0004-6361:20053803.

Chin-Fei Lee and Raghvendra Sahai. Shaping Proto-Planetary and Young Planetary Nebulae with Collimated Fast Winds. ApJ, 586(1):319–337, March 2003. doi: 10.1086/346265.

N. R. Lomb. Least-Squares Frequency Analysis of Unequally Spaced Data. Ap&SS, 39(2): 447–462, February 1976. doi: 10.1007/BF00648343.

A. Manchado, A. Riera, A. Mampaso, P. García Lario, and S. R. Pottasch. IRAS 22568+6141: a new bipolar nebula. , 18:182, September 1989.

Rajeev Manick, Brent Miszalski, and Vanessa McBride. A radial velocity survey for post-common-envelope Wolf-Rayet central stars of planetary nebulae: first results and discovery of the close binary nucleus of NGC 5189. MNRAS, 448(2):1789–1806, April 2015. doi: 10.1093/mnras/stv074.

Roberto H. Méndez. The Planetary Nebulae Luminosity Function (PNLF): current perspectives. In X. Liu, L. Stanghellini, and A. Karakas, editors, *Planetary Nebulae: Multi-Wavelength Probes of Stellar and Galactic Evolution*, volume 323 of *IAU Symposium*, pages 298–302, October 2017. doi: 10.1017/S1743921317000461.

Roberto H. Méndez, Rolf-Peter Kudritzki, and Miguel A. Urbaneja. The Two Central Stars of NGC 1514: Can They Actually Be Related? ApJ, 829(2):73, October 2016. doi: 10.3847/0004-637X/829/2/73.

B. Miszalski, A. Acker, A. F. J. Moffat, Q. A. Parker, and A. Udalski. Binary planetary nebulae nuclei towards the Galactic bulge. I. Sample discovery, period distribution, and binary fraction. A&A, 496(3):813–825, March 2009. doi: 10.1051/0004-6361/200811380.

B. Miszalski, J. Mikołajewska, J. Köppen, T. Rauch, A. Acker, M. Cohen, D. J. Frew, A. F. J. Moffat, Q. A. Parker, A. F. Jones, and A. Udalski. The influence of binarity on dust obscuration events in the planetary nebula M 2-29 and its analogues. A&A, 528: A39, April 2011. doi: 10.1051/0004-6361/201015469.

B. Miszalski, P. A. Crowther, O. De Marco, J. Köppen, A. F. J. Moffat, A. Acker, and T. C. Hillwig. IC 4663: the first unambiguous [WN] Wolf-Rayet central star of a planetary nebula. MNRAS, 423(1):934–947, June 2012. doi: 10.1111/j.1365-2966.2012.20929.x.

B. Miszalski, R. Manick, J. Mikołajewska, K. Iłkiewicz, D. Kamath, and H. Van Winckel. SALT HRS discovery of a long-period double-degenerate binary in the planetary nebula NGC 1360. MNRAS, 473(2):2275–2287, January 2018a. doi: 10.1093/mnras/stx2501.

B. Miszalski, R. Manick, H. Van Winckel, and J. Mikołajewska. The post-common-envelope binary nucleus of the planetary nebula IC 4776: neither an anomalously long orbital period nor a Wolf-Rayet binary. MNRAS, 487(1):1040–1046, July 2019a. doi: 10.1093/mnras/stz1315.

Brent Miszalski, Rajeev Manick, Joanna Mikołajewska, Hans Van Winckel, and Krystian Iłkiewicz. SALT HRS Discovery of the Binary Nucleus of the Etched Hourglass Nebula MyCn 18. , 35:e027, June 2018b. doi: 10.1017/pasa.2018.23.

Brent Miszalski, Rajeev Manick, Thomas Rauch, Krystian Iłkiewicz, Hans Van Winckel, and Joanna Mikołajewska. Two's company, three's a crowd: SALT reveals the likely triple nature of the nucleus of the extreme abundance discrepancy factor planetary nebula Sp 3. , 36:e042, January 2019b. doi: 10.1017/pasa.2019.36.

A. F. J. Moffat. Asymmetries and inhomogeneities in Wolf-Rayet winds. In J. M. Vreux, A. Detal, D. Fraipont-Caro, E. Gosset, and G. Rauw, editors, *Liege International Astrophysical Colloquia*, volume 33 of *Liege International Astrophysical Colloquia*, page 199, January 1996.

M. Morris. Models for the structure and origin of bipolar nebulae. ApJ, 249:572–585, October 1981. doi: 10.1086/159317.

Mark Morris. Mechanisms for mass loss from cool stars. PASP, 99:1115–1122, November 1987. doi: 10.1086/132089.

A. Nebot Gómez-Morán, B. T. Gänsicke, M. R. Schreiber, A. Rebassa-Mansergas, A. D. Schwope, J. Southworth, A. Aungwerojwit, M. Bothe, P. J. Davis, U. Kolb, M. Müller, C. Papadaki, S. Pyrzas, A. Rabitz, P. Rodríguez-Gil, L. Schmidtobreick, R. Schwarz, C. Tappert, O. Toloza, J. Vogel, and M. Zorotovic. Post common envelope binaries

from SDSS. XII. The orbital period distribution. A&A, 536:A43, December 2011. doi: 10.1051/0004-6361/201117514.

Matthew Newville, Till Stensitzki, Daniel B. Allen, Michal Rawlik, Antonino Ingargiola, and Andrew Nelson. Lmfit: Non-Linear Least-Square Minimization and Curve-Fitting for Python, June 2016.

J. V. Perea-Calderón, D. A. García-Hernández, P. García-Lario, R. Szczerba, and M. Bobrowsky. The mixed chemistry phenomenon in Galactic Bulge PNe. A&A, 495(2):L5–L8, February 2009. doi: 10.1051/0004-6361:200811457.

G. Pojmanski. The All Sky Automated Survey. Catalog of Variable Stars. I. 0 h - 6 hQuarter of the Southern Hemisphere. , 52:397–427, December 2002.

D. L. Pollacco, D. Kilkenny, F. Marang, F. van Wyk, and G. Roberts. The discovery of photometric variations in the prototype WC 11 star CPD -56 8032. MNRAS, 256:669–672, June 1992. doi: 10.1093/mnras/256.4.669.

A. C. Raga, A. Esquivel, P. F. Velázquez, J. Cantó, S. Haro-Corzo, A. Riera, and A. Rodríguez-González. Mirror and Point Symmetries in a Ballistic Jet from a Binary System. ApJ, 707(1):L6–L11, December 2009. doi: 10.1088/0004-637X/707/1/L6.

G. Raskin, H. van Winckel, H. Hensberge, A. Jorissen, H. Lehmann, C. Waelkens, G. Avila, J. P. de Cuyper, P. Degroote, R. Dubosson, L. Dumortier, Y. Frémat, U. Laux, B. Michaud, J. Morren, J. Perez Padilla, W. Pessemier, S. Prins, K. Smolders, S. van Eck, and J. Winkler. HERMES: a high-resolution fibre-fed spectrograph for the Mercator telescope. A&A, 526:A69, February 2011. doi: 10.1051/0004-6361/201015435.

George R. Ricker, Joshua N. Winn, Roland Vanderspek, David W. Latham, Gáspár Á. Bakos, Jacob L. Bean, Zachory K. Berta-Thompson, Timothy M. Brown, Lars Buchhave, Nathaniel R. Butler, R. Paul Butler, William J. Chaplin, David Charbonneau, Jørgen Christensen-Dalsgaard, Mark Clampin, Drake Deming, John Doty, Nathan De Lee, Courtney Dressing, Edward W. Dunham, Michael Endl, Francois Fressin, Jian Ge, Thomas Henning, Matthew J. Holman, Andrew W. Howard, Shigeru Ida, Jon M. Jenkins, Garrett Jernigan, John Asher Johnson, Lisa Kaltenegger, Nobuyuki Kawai, Hans Kjeldsen, Gregory Laughlin, Alan M. Levine, Douglas Lin, Jack J. Lissauer, Phillip MacQueen, Geoffrey Marcy, Peter R. McCullough, Timothy D. Morton, Norio Narita, Martin Paegert, Enric Palle, Francesco Pepe, Joshua Pepper, Andreas Quirrenbach, Stephen A. Rinehart, Dimitar Sasselov, Bun'ei Sato, Sara Seager, Alessandro Sozzetti, Keivan G. Stassun, Peter Sullivan, Andrew Szentgyorgyi, Guillermo Torres, Stephane Udry, and Joel Villasenor. Transiting Exoplanet Survey Satellite (TESS). *Journal of Astronomical Telescopes, Instruments, and Systems*, 1:014003, January 2015. doi: 10.1117/1.JATIS.1.1.014003.

Nicolas A. Roddier, Daniel R. Blanco, Larry W. Goble, and Claude A. Roddier. *WIYN telescope active optics system*, volume 2479 of *Society of Photo-Optical Instrumentation Engineers (SPIE) Conference Series*, pages 364–376. 1995. doi: 10.1117/12.211446.

R. Sahai and J. Trauger. Bipolar Bubbles, Jets and Rings in Very Low Excitation Planetary Nebulae - First Results from an HST/WFPC2 Imaging Survey. In *American Astronomical Society Meeting Abstracts*, volume 189 of *American Astronomical Society Meeting Abstracts*, page 97.06, December 1996.

R. Sahai, M. Rubin, C. Sánchez Contreras, and M. Claussen. Probing the "Missing Mass" in Bipolar and Multipolar Pre-Planetary Nebulae. In *Asymmetrical Planetary Nebulae IV*, page 58, June 2007.

R. Sahai, III Villar, G. G., and M. Morris. Young planetary nebulae: Hubble Space Telescope imaging and new morphological classifications system. In *Asymmetric Planetary Nebulae 5 Conference*, page P21, January 2011.

Raghvendra Sahai. The Starfish Twins: Two Young Planetary Nebulae with Extreme Multipolar Morphology. ApJ, 537(1):L43–L47, July 2000. doi: 10.1086/312748.

Raghvendra Sahai and John T. Trauger. Multipolar Bubbles and Jets in Low-Excitation Planetary Nebulae: Toward a New Understanding of the Formation and Shaping of Planetary Nebulae. AJ, 116(3):1357–1366, September 1998. doi: 10.1086/300504.

Raghvendra Sahai, Aditya Dayal, Alan M. Watson, John T. Trauger, Karl R. Stapelfeldt, Christopher J. Burrows, III Gallagher, John S., Paul A. Scowen, J. Jeff Hester, Robin W. Evans, Gilda E. Ballester, John T. Clarke, David Crisp, Richard E. Griffiths, John G. Hoessel, Jon A. Holtzman, John Krist, and Jeremy R. Mould. The Etched Hourglass Nebula MyCn 18. I. Hubble Space Telescope Observations. AJ, 118(1):468–476, July 1999. doi: 10.1086/300939.

J. D. Scargle. Studies in astronomical time series analysis. II. Statistical aspects of spectral analysis of unevenly spaced data. ApJ, 263:835–853, December 1982. doi: 10.1086/160554.

Arthur Schuster. Bigelow's "Solar and terrestrial magnetism". *Terrestrial Magnetism (Journal of Geophysical Research)*, 3(4):179, January 1898. doi: 10.1029/TM003i004p00179.

N. Soker. Axisymmetrical structures of planetary nebulae and SN 1987A. Phys. Rep., 311: 307–316, April 1999. doi: 10.1016/S0370-1573(98)00108-2.

Noam Soker. Why Magnetic Fields Cannot Be the Main Agent Shaping Planetary Nebulae. PASP, 118(840):260–269, February 2006. doi: 10.1086/498829.

Noam Soker and Mario Livio. Interacting Winds and the Shaping of Planetary Nebulae. ApJ, 339:268, April 1989. doi: 10.1086/167294.

Noam Soker and Mario Livio. Disks and jets in planetary nebulae. ApJ, 421:219, January 1994. doi: 10.1086/173639.

Noam Soker and Saul Rappaport. The Formation of Very Narrow Waist Bipolar Planetary Nebulae. ApJ, 538(1):241–259, July 2000. doi: 10.1086/309112.

Noam Soker, Saul Rappaport, and Amos Harpaz. Eccentric Binary Model for Off-Center Planetary Nebula Nuclei. ApJ, 496(2):842–848, March 1998. doi: 10.1086/305413.

P. M. Sorensen and D. L. Pollacco. *Binary Central Stars in Planetary Nebulae*, volume 303 of *Astronomical Society of the Pacific Conference Series*, page 494. 2003.

O. Stahl, A. Kaufer, and S. Tubbesing. *The FEROS spectrograph*, volume 188 of *Astronomical Society of the Pacific Conference Series*, page 331. 1999.

Letizia Stanghellini and Misha Haywood. The Galactic Structure and Chemical Evolution Traced by the Population of Planetary Nebulae. ApJ, 714(2):1096–1107, May 2010. doi: 10.1088/0004-637X/714/2/1096.

M. Steffen, S. Hubrig, H. Todt, M. Schöller, W. R. Hamann, C. Sandin, and D. Schönberner. Weak magnetic fields in central stars of planetary nebulae? A&A, 570:A88, October 2014. doi: 10.1051/0004-6361/201423842.

P. Tisserand, J. B. Marquette, P. R. Wood, É. Lesquoy, J. P. Beaulieu, A. Milsztajn, C. Hamadache, C. Afonso, J. N. Albert, J. Andersen, R. Ansari, É. Aubourg, P. Bareyre, X. Charlot, C. Coutures, R. Ferlet, P. Fouqué, J. F. Glicenstein, B. Goldman, A. Gould, M. Gros, J. Haissinski, J. de Kat, L. Le Guillou, C. Loup, C. Magneville, É. Maurice, A. Maury, M. Moniez, N. Palanque-Delabrouille, O. Perdereau, Y. Rahal, J. Rich, M. Spiro, A. Vidal-Madjar, and S. Zylberajch. R Coronae Borealis stars in the Galactic bulge discovered by EROS-2. A&A, 481(3):673–690, April 2008. doi: 10.1051/0004-6361:20078814.

James Tocknell, Orsola De Marco, and Mark Wardle. Constraints on common envelope magnetic fields from observations of jets in planetary nebulae. MNRAS, 439(2):2014–2024, April 2014. doi: 10.1093/mnras/stu079.

H. Todt and W. R. Hamann. Wolf-Rayet central stars of planetary nebulae. In Wolf-Rainer Hamann, Andreas Sander, and Helge Todt, editors, *Wolf-Rayet Stars*, pages 253–258, January 2015.

J. Tonry and M. Davis. A survey of galaxy redshifts. I. Data reduction techniques. AJ, 84: 1511–1525, October 1979. doi: 10.1086/112569.

S. Toonen and G. Nelemans. The effect of common-envelope evolution on the visible population of post-common-envelope binaries. A&A, 557:A87, September 2013. doi: 10.1051/0004-6361/201321753.

Peter G. Tuthill, John D. Monnier, Nicholas Lawrance, William C. Danchi, Stan P. Owocki, and Kenneth G. Gayley. The Prototype Colliding-Wind Pinwheel WR 104. ApJ, 675(1): 698–710, March 2008. doi: 10.1086/527286.

Hans Van Winckel, Alain Jorissen, Katrina Exter, Gert Raskin, Saskia Prins, Jesus Perez Padilla, Florian Merges, and Wim Pessemier. Binary central stars of planetary nebulae

with long orbits: the radial velocity orbit of BD+33°2642 (PN G052.7+50.7) and the orbital motion of HD 112313 (PN LoTr5). A&A, 563:L10, March 2014. doi: 10.1051/0004-6361/201423650.

Jacob T. VanderPlas. Understanding the Lomb-Scargle Periodogram. ApJS, 236(1):16, May 2018. doi: 10.3847/1538-4365/aab766.

Pablo F. Velázquez, Wolfgang Steffen, Alejand ro C. Raga, Sinhué Haro-Corzo, Alejandro Esquivel, Jorge Cantó, and Angels Riera. Shaping the Red Rectangle Proto-planetary Nebula by a Precessing Jet. ApJ, 734(1):57, June 2011. doi: 10.1088/0004-637X/734/1/57.

Pablo F. Velázquez, Alejandro C. Raga, Angels Riera, Wolfgang Steffen, Alejandro Esquivel, Jorge Cantó, and Sinhué Haro-Corzo. Multipolar young planetary nebulae modelled as a precessing and orbiting jet with time-dependent ejection velocity. MNRAS, 419(4):3529–3536, February 2012. doi: 10.1111/j.1365-2966.2011.19991.x.

Pablo F. Velázquez, Angels Riera, Alejandro C. Raga, and Juan C. Toledo-Roy. An Asymmetric Jet-launching Model for the Protoplanetary Nebula CRL 618. ApJ, 794(2):128, October 2014. doi: 10.1088/0004-637X/794/2/128.

L. B. F. M. Waters and F. G. Molster. Crystalline silicates in AGB and post-AGB stars. In T. Le Bertre, A. Lebre, and C. Waelkens, editors, *Asymptotic Giant Branch Stars*, volume 191 of *IAU Symposium*, page 209, January 1999.

L. B. F. M. Waters, D. A. Beintema, A. A. Zijlstra, A. de Koter, F. J. Molster, J. Bouwman, T. de Jong, S. R. Pottasch, and Th. de Graauw. Crystalline silicates in planetary nebulae with [WC] central stars. A&A, 331:L61–L64, March 1998.

P. M. Williams. Variable dust emission by WC type Wolf-Rayet stars observed in the NEOWISE-R survey. MNRAS, 488(1):1282–1300, September 2019. doi: 10.1093/mnras/stz1784.

A. A. Zijlstra, M. J. Gaylard, P. te Lintel Hekkert, J. Menzies, L. A. Nyman, and H. E. Schwarz. IRAS 07027-7934 : the link between OH/IR stars and carbon-rich planetary nebulae. A&A, 243:L9, March 1991.

Yangyuxin Zou, Adam Frank, Zhuo Chen, Thomas Reichardt, Orsola De Marco, Eric G. Blackman, Jason Nordhaus, Bruce Balick, Jonathan Carroll-Nellenback, Luke Chamandy, and Baowei Liu. Bipolar Planetary Nebulae from Outflow Collimation by Common Envelope Evolution. *arXiv e-prints*, art. arXiv:1912.01647, December 2019.